Fakultät für Maschinenwesen
Lehrstuhl für Angewandte Mechanik

Spatial Dynamics of Pushbelt CVTs: Model Enhancements to a Non-smooth Flexible Multibody System

Dipl.-Tech. Math. Univ. Thomas H. Cebulla

Vollständiger Abdruck der von der Fakultät für Maschinenwesen der
Technischen Universität München zur Erlangung des akademischen Grades eines

Doktor-Ingenieurs (Dr.-Ing.)

genehmigten Dissertation.

Vorsitzender: Univ.-Prof. dr. ir. Daniel J. Rixen

Prüfer der Dissertation:

1. Univ.-Prof. Dr.-Ing. habil. Heinz Ulbrich, i. R.
2. Univ.-Prof. Dr.-Ing. Carlo L. Bottasso

Die Dissertation wurde am 16.09.2013 bei der Technischen Universität München
eingereicht und durch die Fakultät für Maschinenwesen am 21.01.2014 angenommen.

Abstract

This study deals with the spatial dynamics of pushbelt continuously variable transmissions. The basis is a transient non-smooth flexible multibody system, in which measure differential equations in combination with set-valued force laws are numerically integrated by means of using time-stepping schemes. This model is modularly refined by means of different enhancements to represent the physical characteristics of the transmission in more detail. The enhancements include both increasing the possibilities to specify boundary conditions for the model and the geometrical adaptation of single bodies. Moreover, a reduced hybrid model has been added, which represents the planar phenomena in a faster computing time and a concept of pre-integration is presented. Furthermore, the contact model between single bodies has been refined and a spatial quasi-static coupled contact law enhances the model. A geometric nonlinear Cosserat rod model is presented and methods of nonlinear model order reduction are tested in combination with constraints to this rod model. The effects of the different model enhancements on single phenomena are analysed. Comparisons with measurements validate the hybrid model resulting in very good results.

Danksagung

Diese Studie fasst die Ergebnisse meiner Arbeit als wissenschaftlicher Mitarbeiter von Januar 2010 bis April 2013 am Lehrstuhl für Angewandte Mechanik an der Technischen Universität München zusammen. Sie wurde von Bosch Transmission Technology B.V. ermöglicht und finanziert.

Herzlicher Dank gebührt meinem Doktorvater Prof. Dr.-Ing. habil. Heinz Ulbrich i. R. für die Betreuung und stete Unterstützung dieser Arbeit. Das mir entgegengebrachte Vertrauen und die Freiheit mich in diesem Projekt entfalten zu können trugen zum Erfolg bei. Herrn Prof. Dr.-Ing. Carlo L. Bottasso danke ich für die Übernahme des Zweitgutachtens und das große Interesse an meiner Arbeit. Auch möchte ich mich bei Prof. dr. ir. Daniel J. Rixen für die Übernahme des Prüfungsvorsitzes bedanken.

Bei Bosch Transmission Technology B.V. bedanke ich mich ganz besonders bei Arie van der Velde, Semih Yildiz und Han Pijpers. Die Zusammenarbeit lief stets reibungslos und bereitete mir große Freude. Des Weiteren möchte ich mich bei allen Kollegen insbesondere den Rechneradministratoren am Lehrstuhl für Angewandte Mechanik für die große Hilfsbereitschaft bedanken. Besonders hervorheben möchte ich Thorsten Schindler als meinen Vorgänger in diesem Projekt. Er legte nicht nur den Grundstein für diese Arbeit, sondern unterstützte mich hierin in allen Belangen. Darüber hinaus bedanke ich mich bei Kilian Grundl, der das Projekt weiterführt und eine große Bereicherung für dieses darstellt.

Zudem bedanke ich mich bei den Korrekturlesern Thorsten Schindler, Kilian Grundl, Arie van der Velde und Isabel Siegel für ihre äußerst akribische Durchsicht und die konstruktiven Anmerkungen. Zuletzt möchte ich mich bei meinen Eltern und Freunden für die tatkräftige Unterstützung alle Jahre bis zur Fertigstellung dieser Arbeit bedanken.

Contents

1 Introduction

The spatial dynamics of a continuously variable transmission (CVT) are dealt with in the context a of non-smooth flexible multibody system in this study. It represents the continuation of a good and long-standing cooperation between the Institute of Applied Mechanics of the Technische Universität München and Van Doorne's Transmissie, later Bosch Transmission Technology B.V., in Tilburg, the Netherlands. The objective of this cooperation, as well as of this study, is to contribute to the overall optimisation of the CVT transmission and thus to improve its efficiency. This improvement process has an impact on the global goal of reducing the fuel consumption and CO_2 emissions. Through the ongoing optimisation at Bosch concerning different technology fields (e.g. mechanics, hydraulics and control), a concept study on a new CVT prototype has been presented in [26] with "a weight & size reduction of 10-15% and a fuel economy improvement of 7% comparing to the current generation" [26, p. 427].

The joint research project with the aim to analyse the dynamics of the pushbelt continuously variable transmission variator started with [8], where the entire pushbelt was simplified to a one-dimensional continuum. After that, a planar dynamic multibody simulation model of the pushbelt CVT variator was accomplished and validated in [17] and is used at Bosch for the development of their system. Here, the pushbelt is divided into a nonlinear geometric beam model for the ring set and rigid bodies for the elements. Further projects originated with the aim to cover also out-of-plane effects by developing a dynamic multibody variator model in three dimensions. The foundation has been laid in [45]. Many important technical features of the system have been integrated into the model and a first validation has been done. However, a model refinement with many additional functional details as well as an intensified validation of the final system had yet to be done. The first is approached in this study and the second in its follow-up project.

As the title of this study already suggests, its objective is to add different model enhancements to the spatial model to cover the physical characteristics of the pushbelt CVT variator in more detail. The simulation model had to be enhanced with a unilateral element - ring set contact to enable a lifting of the ring sets from the element saddle. In combination with this unilateral element - ring set contact, a lateral movement of the ring sets on the element saddles should be enabled, controlled by a ring tracking law. Then, variable boundary conditions should increase the options to specify load conditions on the pushbelt CVT model. In addition, tapered elements should represent different element shapes resulting from manufacturing affecting the dynamics of the system. Last, a coupled contact law for the element - sheave contact had to be added to enable coupling of the elements through the elasticity of the pulley sheaves in a contact quasi-statically. All the additional technical features had to be added to the model in a modular way to enable or disable different features and combine them in a reasonable way. In addition, the computing time had to be reduced employing different strategies. The planar model [17] had been developed in an older software which was no longer maintained. Meanwhile, the institute proceeded to a new multibody simulation software *MBSim* [31], wherein the spatial model has been developed. So, the desire was to have a fast state-of-the-art (extended) planar model in the current software to cover a lot of phenomena in a much shorter computing time. In summary, the model [45] should be enhanced with these features. An intensified validation of the spatial model is instructed in the project plan of the follow-up project. Therefore, in this study not a final but further validation is carried out and comparisons of the different model enhancements with the existing ones are shown.

So far, extensive research work concerning the simulation of CVTs have been carried out. A literature survey concerning the dynamics of pushbelt CVTs and multibody systems is given in [17]. An extensive review paper on the state of the art of dynamics and control of both belt and chain CVTs is found in [49]. A short survey of CVT simulation models is presented in [45] with arguments for the need for a spatial simulation model. Thus, the reader is referred to these sources and it is not necessary to give a literature review at this point. Examples for newer developments are: In [42], a very simple model of the belt has been presented focusing on fast calculation. It neglects inertia terms and bending stiffness and models the pushbelt as a one-dimensional continuum. In [43], a method has been presented to prognosticate the transmission efficiency of a pushbelt CVT variator. An accurate model of friction forces and sliding velocities is given to determine the friction loss. In [50], investigations of the scuffing resistance of belt and chain CVTs with experiments and a simulation model based on [44, 51] have been presented. Overall, the spatial transient simulation model [45] represents one of the most detailed simulation model of a pushbelt CVT. It considers out-of-plane effects, but has a high computing time because of the large number of degrees of freedom (about 3500) and contacts (about 5500). Further literature references concerning the addressed topics of this study are given in the respective chapters.

This study is structured as follows. The chapters 2 and 3 are introductory chapters to expose the background and basis for this study. Chapter 2 sums up existing theory from literature on non-smooth flexible multibody systems, where the pushbelt CVT model is embedded. Chapter 3 explains some backgrounds on CVTs, in general, and the model [45] which is the point of departure of this study. After this introduction to the topic, the different model enhancements which have been accomplished during this study are presented in Chapter 4 to Chapter 6. Chapter 4 combines three enhancements under the umbrella term initialisation. These are the variable boundary conditions, the tapered elements and the concept of planar pre-integration. Chapter 5 contains two enhancements under the term interactions, which are the unilateral element - ring set contact and the coupled contact law for the element - sheave contact. In Chapter

6, three enhancements are presented which focus on model reduction. These are the hybrid pushbelt CVT model, the derivation of a planar Cosserat rod model and an approach of nonlinear model order reduction for this rod model. After that, results and verification of the model enhancements are shown in Chapter 7. Chapter 8 closes this study with conclusions and recommendations for future work.

2 Non-smooth Flexible Multibody Systems

The dynamic behaviour of mechanical systems can be modelled, simulated and analysed within multibody systems. These methods provide the necessary tools to model the system with differential equations and to numerically integrate the equations of motion by means of different integrators. The mechanical system is split into (rigid and flexible) bodies and the corresponding mass-less links between them, like e.g. contacts, joints (i.e. hinges or bearings) and spring / damping connections. Each rigid body can move in space with large translation and rotation restricted by the interactions. For a more detailed representation of the bodies, methods to model flexible bodies are integrated into the multibody system. This enables small or large deformations of selected bodies. The contact between bodies can be modelled in different ways. In this study, the non-smooth approach was chosen, as introduced in [34]. It has proven itself in practice cf. [38, 54]. Very detailed references on the non- smooth approach can be found in [1, 6, 29].

In this chapter, a short summary is given of the state of the art from the existing literature to supply the necessary background. First, the measure differential equations (MDEs) are introduced from measure theory with regard to the application in mechanical systems with set-valued force laws. Therefore, they are presented in the composition with generalised velocities, coordinates, forces etc. The MDEs are the theoretical foundation for the equations of motion of non-smooth multibody systems. Then, the contact description with set-valued force laws is shown. The unilateral constraints for example are part of these set-valued force laws and are amongst other things responsible for discontinuities in the systems' velocities. The derivation of the equations of motion is presented and some background on flexible multibody systems is given. Last, some integration schemes for non-smooth systems are demonstrated.

2.1 Functions of bounded variation

The theory of functions of bounded variation originates from mathematical analysis. It builds the basis for the MDEs, which model the non-smooth system equations. The transfer from measure theory to non-smooth mechanics was established by [34]. First of all, for a detailed explanation of the subject, some definitions from calculus of variations have to be given following [33, 18, 29].

The *right-limit* $\boldsymbol{u}^+(t_i)$ of a mapping $\boldsymbol{u}: I \rightarrow \mathrm{I\!R}^n$ with a nonempty closed real interval I

at a fixed time $t_i \in \mathbb{R}$ is defined as

$$\boldsymbol{u}^+(t_i) = \lim_{s \to t_i, s > t_i} \boldsymbol{u}(s), \tag{2.1}$$

if it exists. The right-limit is approached through the course of $\boldsymbol{u}(t)$ from the right side of t_i in the interval, hence it is not defined on the right end of I. Symmetrically, the *left-limit* $\boldsymbol{u}^-(t_i)$ is defined as the limit approached from the left side. If the function $\boldsymbol{u}$ is continuous at t_i, the left- and right-limit are equal at this point.

For the theory of functions of bounded variation, a definition of continuity is required which is more restrictive than ordinary continuity. A function $\boldsymbol{q} : I \to \mathbb{R}^n$ is *absolutely continuous* on I if for every $\varepsilon > 0$ a $\delta > 0$ exists, depending on the respective ε, so that

$$\sum_{i=1}^{m} \|\boldsymbol{q}(b_i) - \boldsymbol{q}(a_i)\| < \varepsilon$$

holds for every finite number of pairwise disjoint sub-intervals $(a_i, b_i) \subset I, \;\; i = 1, \ldots, m$ which fulfil

$$\sum_{i=1}^{m} (b_i - a_i) < \delta.$$

Ordinary continuity is included for the special case of $m = 1$, i.e. the set of all absolute continuous functions is a subset of the set of all continuous functions. The most cited example of a function that is continuous everywhere but not absolutely continuous is the Cantor function.

The *fundamental theorem of calculus* states that an absolute continuous functions $\boldsymbol{q}$ on the interval $[a, b]$ has a derivative $\dot{\boldsymbol{q}}$ almost everywhere on $[a, b]$, which is Lebesgue integrable $\dot{\boldsymbol{q}} \in L^1([a, b])$. The integral of $\dot{\boldsymbol{q}}$ is given by

$$\boldsymbol{q}(b) - \boldsymbol{q}(a) = \int_a^b \dot{\boldsymbol{q}}(t) \, \mathrm{d}t. \tag{2.2}$$

Therefore, the concepts of differentiation and integration are brought into a relation with the concept of absolute continuity.

The *variation* of a multidimensional function $\boldsymbol{u} : I \to \mathbb{R}^n$ on a one-dimensional subinterval $J \subset I \subset \mathbb{R}$ is a map

$$\operatorname{var}(\boldsymbol{u}, J) = \sup_{(t_i)} \sum_{i=1}^{m} \|\boldsymbol{u}(t_i) - \boldsymbol{u}(t_{i-1})\|, \tag{2.3}$$

with $m \in \mathbb{N}$ arbitrary and $(t_i)_{0 \le i \le m}$ denoting all strictly increasing sequences $t_0 < t_1 < \cdots < t_m$ of partitions of J. The supremum is set to infinity if no majorising real number can be given. The variation is a measure for the local oscillation behaviour of a function. If J contains more than one element, it holds

$$\mathrm{var}(\boldsymbol{u}, J) = 0 \quad \Leftrightarrow \quad \boldsymbol{u} \text{ is constant on } J. \tag{2.4}$$

Otherwise, if $J = \{t_i\}$ is a singleton, the variation is always zero independent of the function

$$\mathrm{var}(\boldsymbol{u}, \{t_i\}) = \sup \varnothing = 0. \tag{2.5}$$

The notion of the variation can easily be understood by means of a one-dimensional example. The variation function $g(t) := \mathrm{var}(f, [a,t])$ of any real-valued function $f(t)$ is monotonically increasing. Figure 2.1 shows a function $f(t)$ and the corresponding variation. The function is composed of different sections (constant, linear, polynomial) and different links (kinks, jumps). The variation $\mathrm{var}(f, [a,t])$ summarises figuratively the altitude difference while running through the graph of $f(t)$ including all jumps. Therefore, constant resp. increasing sections of $f(t)$ are represented by constant resp. increasing sections in $\mathrm{var}(f, [a,t])$. Decreasing parts are converted to increasing ones by taking the positive altitude difference. Kinks and discontinuities stay at the same abscissa position as in f, but result always in an increasing ordinate.

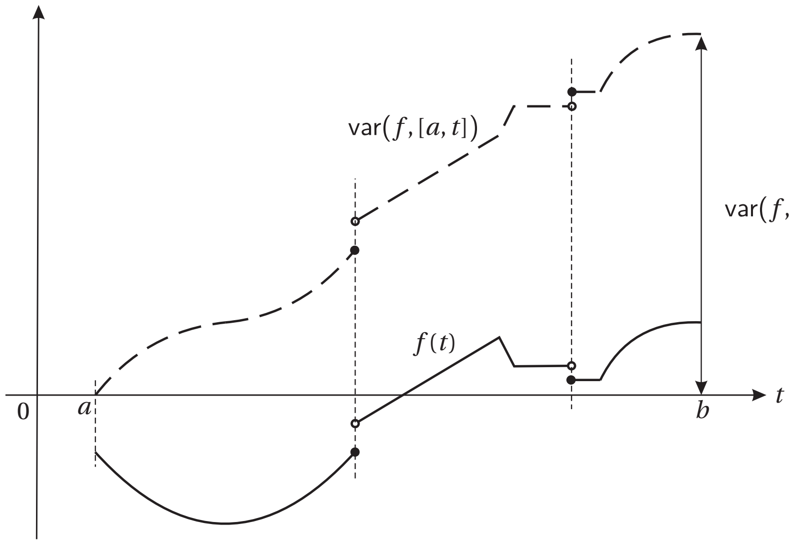

Figure 2.1: Variation function $\mathrm{var}(f, [a,t])$ of function $f(t)$, cf. [29]

The function $\boldsymbol{u} : I \to \mathbb{R}^n$ is of *bounded variation on I* if its variation is finite

$$\boldsymbol{u} \in BV(I) \quad \Leftrightarrow \quad \mathrm{var}(\boldsymbol{u}, I) < +\infty\,. \tag{2.6}$$

Descriptively this means that it has only finitely many oscillations in the finite interval I.

A continuous function is not obligatory of bounded variation. However, every absolutely continuous function on I is of bounded variation on this interval. A typical example for a one-dimensional continuous function that is not of bounded variation is

$$f(t) = \begin{cases} 0, & \text{if } t = 0 \\ t \sin\left(\frac{1}{t}\right), & \text{if } t \neq 0\,. \end{cases} \tag{2.7}$$

Here no upper bound can be given in any interval around 0, which restricts the variation.

Some properties are summarised subsequently similar to [18, p. 59] that are valid for every function of bounded variation $\boldsymbol{u} \in BV(I)$:

1. It has only jump-type discontinuities.
2. The number of discontinuities in I are at most countable.
3. The left-limit $\boldsymbol{u}^-(t)$ and the right-limit $\boldsymbol{u}^+(t)$ exist for every $t \in I$ exempt from the respective boundary points.
4. A decomposition, called Lebesgue decomposition, exists into

   $$\boldsymbol{u} = \boldsymbol{u}_A + \boldsymbol{u}_S + \boldsymbol{u}_{SI}, \tag{2.8}$$

   where

   a) $\boldsymbol{u}_A \in BV(I)$ is an absolutely continuous function,
   b) $\boldsymbol{u}_S \in BV(I)$ is a step function,
   c) $\boldsymbol{u}_{SI} \in BV(I)$ is a singular function, as for instance the Cantor function.
5. It is differentiable almost everywhere.

2.2 Measure differential equations

The states of mechanical systems, more precisely the velocities, are no longer smooth functions when certain set-valued force laws (like e.g. unilateral constraints and dry friction) are added to the system. Thus, the states have to be considered as functions of bounded variation. Standard techniques to describe and solve the equations of motion fail. The measure differential equations applied to non-smooth mechanics close this gap. They originate out of the discipline of measure theory. This section presents the subject from a mathematical point of view following [18, 29].

The assumptions on the time dependent functions (velocities, coordinates and accelerations) to describe non-smooth mechanics with MDEs are summarised:

- The generalised velocities $\boldsymbol{u} : I \rightarrow \mathbb{R}^m$ are functions of bounded variation on a time interval I.

- The generalised coordinates $\boldsymbol{q}: I \to \mathbb{R}^n$ are absolutely continuous and related to the velocities by

$$\boldsymbol{q}(t) = \boldsymbol{q}(t_0) + \int_{t_0}^{t} \boldsymbol{T}(\boldsymbol{q}(\tau))\boldsymbol{u}(\tau)\,\mathrm{d}\tau, \quad t \geq t_0. \tag{2.9}$$

  The matrix $\boldsymbol{T}: \mathbb{R}^n \to \mathbb{R}^{n\times m}$ describes the relationship between the derivative of the spatial generalised coordinates and the generalised velocities.

- As the generalised accelerations $\dot{\boldsymbol{u}} \in L^1(I)$ exist only almost everywhere, they are substituted by a differential measure $\mathrm{d}\boldsymbol{u}$ comprising the overall accelerations.

The assumption that the generalised coordinates $\boldsymbol{q}$ are absolutely continuous is no restriction, as jumps in position and rotation are not of practical interest. Because of the bounded variation, the left- and right-limit of $\boldsymbol{u}$ exist everywhere on I apart from the boundary points. As finitely many discontinuities in $\boldsymbol{u}$ are allowed, the generalised velocities can not be obtained from $\dot{\boldsymbol{u}}$ by integration. This would only yield the absolute continuous fraction of $\boldsymbol{u}$ and would neglect the rest. Therefore, the *differential measure* of $\boldsymbol{u}$ is introduced, denoted by $\mathrm{d}\boldsymbol{u}$. It is associated with the classical $\mathbb{R}^n$-valued Stieltjes measure on the interval I, for which

$$\int_{[t_k,t_l]} \mathrm{d}\boldsymbol{u} = \boldsymbol{u}^+(t_l) - \boldsymbol{u}^-(t_k) \tag{2.10}$$

holds for every compact subinterval $[t_k, t_l]$ of I. Details on the differential measure and the prove of the property (2.10) can be found in [33]. The integral over a singleton $\{t_k\}$ in I depicts either a possible jump at t_k or vanishes if both limits are equal:

$$\int_{\{t_k\}} \mathrm{d}\boldsymbol{u} = \boldsymbol{u}^+(t_k) - \boldsymbol{u}^-(t_k). \tag{2.11}$$

With this differential measure, all three parts of $\boldsymbol{u}$ (absolutely continuous, step and singular function) can be gained from integration of $\mathrm{d}\boldsymbol{u}$. So it is suited to represent the generalised accelerations of non-smooth mechanical systems.

According to (2.8), the function of generalised velocities $\boldsymbol{u} \in BV(I)$ can be decomposed into three parts. Likewise, the corresponding differential measure $\mathrm{d}\boldsymbol{u}$ can be fragmented into

$$\mathrm{d}\boldsymbol{u} = \mathrm{d}\boldsymbol{u}_A + \mathrm{d}\boldsymbol{u}_S + \mathrm{d}\boldsymbol{u}_{SI}\,, \tag{2.12}$$

using the Lebesgue decomposition for the measure [29]. The first part $\mathrm{d}\boldsymbol{u}_A$ is the measure of the absolutely continuous function $\boldsymbol{u}_A$. It takes into account the smooth motion of the velocity. The derivative $\dot{\boldsymbol{u}}_A$, which exists almost everywhere and is integrable, serves as a density function with the Lebesgue measure $\mathrm{d}t$

$$\mathrm{d}\boldsymbol{u}_A = \dot{\boldsymbol{u}}_A \,\mathrm{d}t. \tag{2.13}$$

According to the fundamental theorem of calculus, the integration of $\mathrm{d}\boldsymbol{u}_A$ over any subinterval of I results in

$$\int_{[t_k,t_l]} \mathrm{d}\boldsymbol{u}_A = \int_{[t_k,t_l]} \dot{\boldsymbol{u}}_A \,\mathrm{d}t = \boldsymbol{u}_A(t_l) - \boldsymbol{u}_A(t_k). \tag{2.14}$$

The second measure $\mathrm{d}\boldsymbol{u}_S$ in (2.12) includes the non-smooth part. The step function $\boldsymbol{u}_S$ has countably many jumps at the discontinuity points $\{t_i\}_i$ and is constant elsewhere on the interval I. Hence, its derivative $\dot{\boldsymbol{u}}_S$ is zero for almost every $t \in I$ and the corresponding differential measure has to deal with these non-smooth points. It is purely atomic, as it adds up the Dirac measures at the discontinuities t_i of $\boldsymbol{u}_S$ weighted with the respective jump heights

$$\mathrm{d}\boldsymbol{u}_S = \sum_i \left(\boldsymbol{u}_S^+(t_i) - \boldsymbol{u}_S^-(t_i)\right) \mathrm{d}\delta_{t_i}. \tag{2.15}$$

The definition of the *Dirac measure* with an arbitrary function $\boldsymbol{f} : I \to \mathrm{I\!R}^n$ is given by

$$\int_{[t_k,t_l]} \boldsymbol{f} \,\mathrm{d}\delta_{t_i} = \begin{cases} \boldsymbol{f}(t_i), & \text{if } t_i \in [t_k, t_l], \\ \boldsymbol{0}, & \text{if } t_i \notin [t_k, t_l]. \end{cases} \tag{2.16}$$

With the abbreviatory notation $\mathrm{d}\eta := \sum_i \mathrm{d}\delta_{t_i}$, Equation (2.15) is written as

$$\mathrm{d}\boldsymbol{u}_S = (\boldsymbol{u}_S^+ - \boldsymbol{u}_S^-)\,\mathrm{d}\eta. \tag{2.17}$$

The third term in (2.12), $\mathrm{d}\boldsymbol{u}_{SI}$, is a singular measure. It is assumed zero in this study according to [18], which means the velocities are assumed to have no singular terms. Hence, the singular part is not treated further.

The generalised forces are substituted by a real measure $\mathrm{d}\boldsymbol{\Lambda}$, called the reaction measure. Analogously to the differential measure of the velocity, $\mathrm{d}\boldsymbol{\Lambda}$ can be decomposed into a Lebesgue measurable and an atomic part[1]

$$\mathrm{d}\boldsymbol{\Lambda} = \boldsymbol{\lambda}\,\mathrm{d}t + \boldsymbol{\Lambda}\,\mathrm{d}\eta\,. \tag{2.18}$$

It consists of the smooth contact forces $\boldsymbol{\lambda}$ due to persisting or opening contacts and the impact percussions (or impulses) $\boldsymbol{\Lambda}$ in the case of a closing contact. The measure of the impact percussions is purely atomic and can be split up by the Dirac delta into the

---

[1] Again the singular part is assumed zero.

single impulses at the discontinuities t_i

$$\boldsymbol{\Lambda}\,\mathrm{d}\eta = \sum_i \boldsymbol{\Lambda}(t_i)\,\mathrm{d}\delta_{t_i}\,. \tag{2.19}$$

Altogether, the *measure differential equations* are obtained which contain the smooth equations of motion and the non-smooth impact equations

$$\boldsymbol{M}(\boldsymbol{q})\,\mathrm{d}\boldsymbol{u} = \boldsymbol{h}(\boldsymbol{q},\boldsymbol{u},t)\,\mathrm{d}t + \boldsymbol{W}(\boldsymbol{q})\,\mathrm{d}\boldsymbol{\Lambda}\,. \tag{2.20}$$

The MDEs hold for every t in I. The mass matrix $\boldsymbol{M}$ is symmetric positive definite, the vector $\boldsymbol{h}$ contains the Lebesgue integrable smooth forces including those resulting from single-valued force laws. The matrix $\boldsymbol{W}$ specifies the directions of the set-valued contact reactions. In general these matrix and vector functions are nonlinear in the states.

To show that both systems of equations (smooth and non-smooth) are included, Equation (2.20) is integrated. By integrating over any time interval $J \subset I$ without a discontinuity, the (smooth) equations of motion are gained. For those intervals the impact percussions vanish and therefore the velocity is smooth and only the Lebesgue measurable parts remain. These parts can be combined in one integral equation which holds for every smooth subinterval

$$\int_J \big(\boldsymbol{M}(\boldsymbol{q})\,\dot{\boldsymbol{u}} - \boldsymbol{h}(\boldsymbol{q},\boldsymbol{u},t) - \boldsymbol{W}(\boldsymbol{q})\,\boldsymbol{\lambda}\big)\,\mathrm{d}t = 0 \qquad \forall J \setminus \{t_i\}_i\,. \tag{2.21}$$

The notation $\dot{\boldsymbol{u}} := \dot{\boldsymbol{u}}_A$ is introduced for the smooth part of the generalised accelerations. Out of this integral version the differential equations are gained

$$\boldsymbol{M}(\boldsymbol{q})\,\dot{\boldsymbol{u}} = \boldsymbol{h}(\boldsymbol{q},\boldsymbol{u},t) + \boldsymbol{W}(\boldsymbol{q})\,\boldsymbol{\lambda}\,. \tag{2.22}$$

The (non-smooth) impact equations emerge by integration over a singleton $\{t_i\}$ with discontinuity

$$\int_{\{t_i\}} \big(\boldsymbol{M}(\boldsymbol{q})\big(\boldsymbol{u}^+ - \boldsymbol{u}^-\big) - \boldsymbol{W}(\boldsymbol{q})\,\boldsymbol{\Lambda}\big)\,\mathrm{d}\eta = 0 \qquad \forall\, t_i \in I \tag{2.23}$$

$$\Leftrightarrow \quad \boldsymbol{M}(\boldsymbol{q}(t_i))\big(\boldsymbol{u}^+(t_i) - \boldsymbol{u}^-(t_i)\big) = \boldsymbol{W}(\boldsymbol{q}(t_i))\,\boldsymbol{\Lambda}(t_i)\,. \tag{2.24}$$

This results as the integral (with respect to the Lebesgue measure $\mathrm{d}t$) over every singleton $\{t_i\}$ vanishes for every smooth function. Hence, only the atomic part remains. Equation (2.24) means that in every discontinuity point t_i the non-zero impact percussions effect a velocity jump and therefore the right- and left-limit of the velocity have to be considered.

2.3 Local contact kinematics

A contact description is required for the interactions of the bodies. The given description of the local contact kinematics follows the explanation of [29, 46]. A contour is assigned to each body, i.e. a surface, which is a two-dimensional manifold uniquely defined by a contour parameter $\boldsymbol{s} \in \mathbb{R}^2$. The surfaces are assumed to be convex. One contour can be in contact with one or more contours of other bodies. Contacts between bodies are modelled as discrete point contacts. In order to specify a contact between two contours, the positions vectors of the two contact points $\boldsymbol{r}_{OC_k}$, $k = 1,2$ on each body have to be found out of all potential contact points. This general contact situation is illustrated in Figure 2.2.

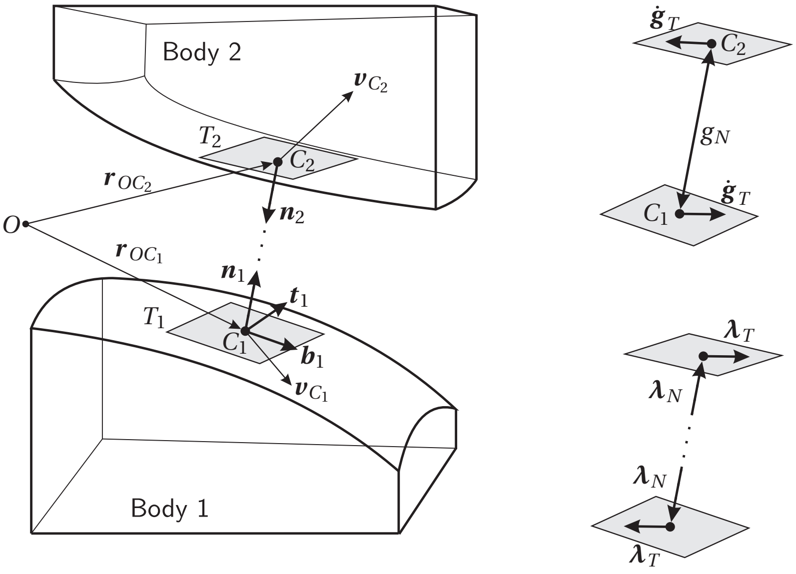

Figure 2.2: Contact geometry between two rigid bodies [29, p. 83]

The two contact points C_1 and C_2 have the minimal distance between all points on both surfaces, i.e. they are the proximal points. Their position vector

$$\boldsymbol{r}_{OC_k} = \boldsymbol{r}_k(\boldsymbol{q}_k, \boldsymbol{s}_{OC_k}), \qquad k = 1,2 \tag{2.25}$$

depends on the contour parameter of the contact point $\boldsymbol{s}_{OC_k}$ and the generalised position $\boldsymbol{q}_k$ of the body. The two contact points are the unknowns that have to be found in the contact search. During the motion $\boldsymbol{q}_k(t)$ of the bodies, the positions of these points on the contour $\boldsymbol{s}_{OC_k}$ and their relative distance may change, so the contact search have to take place in each time step. Each point possesses a contour normal $\boldsymbol{n}_k = \boldsymbol{n}_k(\boldsymbol{q}_k, \boldsymbol{s}_{OC_k})$ that is directed outward and two tangents $\boldsymbol{t}_k(\boldsymbol{q}_k, \boldsymbol{s}_{OC_k})$, $\boldsymbol{b}_k(\boldsymbol{q}_k, \boldsymbol{s}_{OC_k})$, as it can be seen in Figure 2.2. All three vectors are normalised and form an orthonormal basis $(\boldsymbol{t}_k, \boldsymbol{n}_k, \boldsymbol{b}_k)$.

The condition for the contact search is as follows. Two points C_1 and C_2 form a *contact pair* if their respective normals are linearly dependent (i.e. they form the same one-dimensional vector space) and have an opposite sign

$$\boldsymbol{n}_1 = -\boldsymbol{n}_2 \,. \tag{2.26}$$

Consequently, their tangent planes T_1 and T_2 are parallel. The distance vector of the potential contact points C_k have to be orthogonal to both tangent planes

$$\begin{pmatrix} \boldsymbol{t}_1^T \\ \boldsymbol{b}_1^T \\ \boldsymbol{t}_2^T \\ \boldsymbol{b}_2^T \end{pmatrix} \cdot \left(\boldsymbol{r}_{OC_2} - \boldsymbol{r}_{OC_1}\right) = \boldsymbol{0} \,. \tag{2.27}$$

This forms a system of nonlinear implicit equations in $\boldsymbol{s}_{OC_k}$ which is solved numerically by e.g. a multidimensional fixed-point or Newton iteration. For simple contact pairs, e.g. sphere-sphere contacts, the required equations can be set up and solved analytically. The analytical calculation yields the exact solution with in general a faster solution process than its numerical approximation. The numerical solution of the four nonlinear equations in (2.27) with the four unknowns $\boldsymbol{s}_{OC_1}, \boldsymbol{s}_{OC_2}$ is not necessarily unique and therefore the solution with the minimal gap distance

$$g_N = \boldsymbol{n}_1^T \left(\boldsymbol{r}_{OC_2} - \boldsymbol{r}_{OC_1}\right) \tag{2.28}$$

has to be chosen. The relative location of both bodies is expressed by the sign of the gap distance. For $g_N = 0$, the two bodies are touching. A positive sign means that they are separated and a negative sign means that they are penetrated. If $g_N \leq 0$, the bodies are said to be in contact. The normal and tangential relative velocities of the contact points can be calculated out of the vector difference of the absolute velocities ($\boldsymbol{v}_{OC_k} = \dot{\boldsymbol{r}}_{OC_k}$) of the contact points

$$\dot{g}_N = \boldsymbol{n}_1^T \left(\boldsymbol{v}_{OC_2} - \boldsymbol{v}_{OC_1}\right) , \qquad \dot{\boldsymbol{g}}_T = \begin{pmatrix} \boldsymbol{t}_1^T \\ \boldsymbol{b}_1^T \end{pmatrix} \cdot \left(\boldsymbol{v}_{OC_2} - \boldsymbol{v}_{OC_1}\right) . \tag{2.29}$$

Projecting the local absolute velocities into the global space of generalised velocities $\boldsymbol{u}$ by the corresponding Jacobian matrices, the relative velocities can be expressed depending on the generalised velocities, the generalised coordinates and the time

$$\dot{g}_N = \dot{g}_N(\boldsymbol{u}, \boldsymbol{q}, t) \,, \quad \dot{\boldsymbol{g}}_T = \dot{\boldsymbol{g}}_T(\boldsymbol{u}, \boldsymbol{q}, t) \,. \tag{2.30}$$

For details on that issue see [59].

2.4 Set-valued force laws

Still $\boldsymbol{\lambda}$ and $\boldsymbol{\Lambda}$ are unknown in (2.18) and have to be specified with additional equations. With the preparatory work of the contact kinematics of Section 2.3 this is done by means of set-valued force laws. Together with the MDEs they form a measure differential inclusion. The theory of this section is based on the field of set-valued and convex analysis. Introductorily, some definitions are given following [29].

A *set-valued map* assigns to each preimage at least one image. More general, it is a mapping in the set of all nonempty compact subsets of $\mathbb{R}^m$. Therefore, the graph of these functions can have 'vertical' segments. A simple example is the planar Coulomb friction law in the case of no slip, cf. Figure 2.4*c*.

The *normal cone* $N_C(\boldsymbol{x})$ of a convex set $C \subset \mathbb{R}^n$ in $\boldsymbol{x} \in C$ is given by

$$N_C(\boldsymbol{x}) := \left\{\boldsymbol{y} \in \mathbb{R}^n\,; \quad \boldsymbol{y}^T(\boldsymbol{x}^* - \boldsymbol{x}) \leq 0,\ \forall \boldsymbol{x}^* \in C\right\}\,. \tag{2.31}$$

It can easily be seen that the zero vector is always element of the normal cone. An equivalent definition of the normal cone can be given by means of the prox function, see [2]. The *proximal point* of the convex set $C \subset \mathbb{R}^n$ to a point $\boldsymbol{x} \in \mathbb{R}^n$ is defined as

$$\underset{C}{\mathbf{prox}}(\boldsymbol{x}) = \arg\min_{\boldsymbol{x}^* \in C} \|\boldsymbol{x} - \boldsymbol{x}^*\|_2\,. \tag{2.32}$$

It is the closest point in C to $\boldsymbol{x}$, as it minimises the Euclidean distance between the point $\boldsymbol{x}$ and all points in C. With the prox function the normal cone in $\boldsymbol{x} \in C$ can also be written as

$$N_C(\boldsymbol{x}) = \left\{\boldsymbol{y} \in \mathbb{R}^n\,; \quad \underset{C}{\mathbf{prox}}(\boldsymbol{x} + r\boldsymbol{y}) = \boldsymbol{x},\ \forall r > 0\right\}. \tag{2.33}$$

Further, it holds for $\boldsymbol{x} \in \mathbb{R}^n$ that [29]

$$\boldsymbol{x} - \underset{C}{\mathbf{prox}}(\boldsymbol{x}) \in N_C\left(\underset{C}{\mathbf{prox}}(\boldsymbol{x})\right), \tag{2.34}$$

which is well-defined as $\mathbf{prox}_C(\boldsymbol{x}) \in C$. This shows the close link between the normal cone and the proximal point formulation. The value r in (2.33) is positive and shows the characteristic of a cone that, if a vector is contained in a cone then also every positive multiple is included.

The concept of the proximal point is illustrated in Figure 2.3. In the case that $\boldsymbol{x} \notin C$ then $\mathbf{prox}_C(\boldsymbol{x})$ maps on the boundary of C. This mapping is done by a perpendicular projection of $\boldsymbol{x}$ onto C (cf. $\boldsymbol{x}_1$). If the boundary of C is not smooth but has a kink, then the image is not unique, see $\boldsymbol{x}_3$. All points of the shaded cone with both lines normal to the set C are projected onto the same corner. This cone corresponds to the normal cone shifted from the origin into $\mathbf{prox}(\boldsymbol{x}_3)$. In the other case, if $\boldsymbol{x} \in C$, then the prox function maps on itself, see $\boldsymbol{x}_2$.

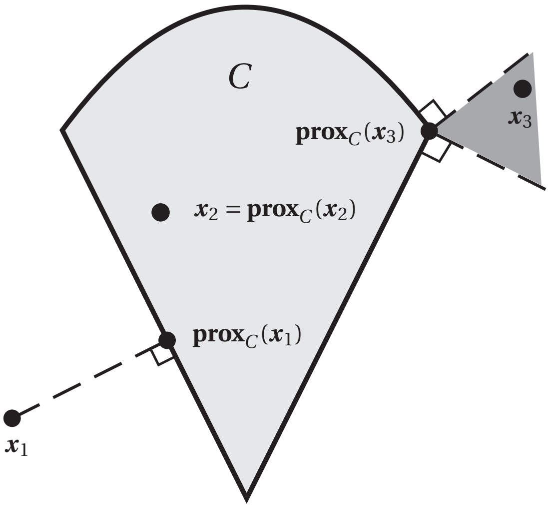

Figure 2.3: Concept of proximal point with a convex set C [29]

With the help of these definitions, three set-valued force laws are given in equivalent formulations following [29, 47]. They are illustrated in Figure 2.4. The laws can be formulated on three kinematic levels - position, velocity or acceleration, cf. [18]. The contact laws and impact laws have to be distinguished. They are sub-divided into normal and tangential directions. The contact force in normal direction is denoted with λ_N and the tangential contact force with

$$\boldsymbol{\lambda}_T = \begin{pmatrix} \lambda_{T,1} \\ \lambda_{T,1} \end{pmatrix}, \tag{2.35}$$

their respective directions are shown in Figure 2.2. The contact laws in normal direction are shown first, which include the unilateral and bilateral laws. After that, a friction law in tangential direction is given.

The *unilateral contact law* can be modelled by a complementarity formulation (the Signorini-Fichera-condition) between the normal gap distance g_N and the normal contact force λ_N. A push force avoids penetration. The so called unilateral primitive, i.e. both positive coordinate axes including the origin, is the corresponding set, see Figure 2.4*a*. This law is given on position level in three equivalent formulations - the complementarity, proximal point and normal cone formulation:

$$U_C = \left\{(g_N, \lambda_N) \in \mathrm{I\!R} \times \mathrm{I\!R}; \quad g_N \geq 0,\ \lambda_N \geq 0,\ g_N \lambda_N = 0\right\}, \tag{2.36a}$$

$$U_P = \left\{(g_N, \lambda_N) \in \mathrm{I\!R} \times \mathrm{I\!R}; \quad \underset{\mathrm{I\!R}^+}{\mathrm{prox}}(\lambda_N - r\, g_N) = \lambda_N,\ r > 0\right\}, \tag{2.36b}$$

$$U_N = \left\{ (g_N, \lambda_N) \in \mathrm{I\!R} \times \mathrm{I\!R}; \quad -g_N \in N_{\mathrm{I\!R}^+}(\lambda_N) \right\}, \tag{2.36c}$$

with $\mathrm{I\!R}^+ = \{x \in \mathrm{I\!R};\ x \geq 0\}$.

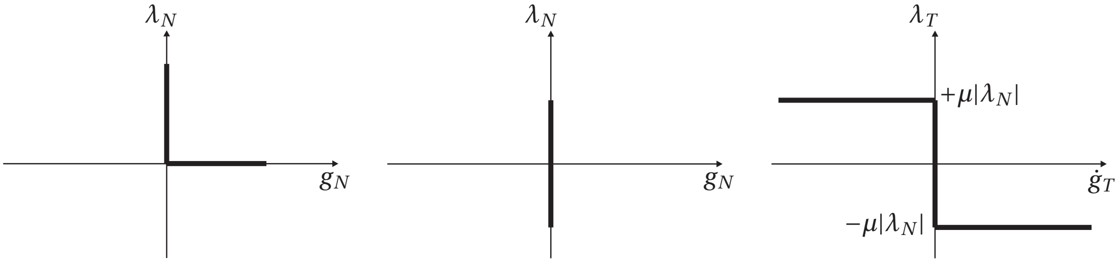

(a) Unilateral constraint (b) Bilateral constraint (c) Planar Coulomb friction

Figure 2.4: Set-valued force laws [45, p. 7]

The *bilateral contact law* allows no separation of the bodies which is realised by both, push and pull forces. The equivalent equations on position level are

$$B_C = \left\{ (g_N, \lambda_N) \in \mathrm{I\!R} \times \mathrm{I\!R}; \quad g_N = 0,\ \lambda_N \lesseqgtr 0 \right\}, \tag{2.37a}$$

$$B_P = \left\{ (g_N, \lambda_N) \in \mathrm{I\!R} \times \mathrm{I\!R}; \quad \operatorname*{prox}_{\mathrm{I\!R}}(\lambda_N - r\, g_N) = \lambda_N,\ r > 0 \right\}. \tag{2.37b}$$

As $N_{\mathrm{I\!R}}(\lambda_N)$ is not defined according to (2.31), the normal cone formulation is not given. In contrast to the unilateral law, the bilateral constraint causes no discontinuities in the velocities as no impact can occur.

Coulomb's friction law is a set-valued friction law for the tangential directions of a closed contact. Two different cases, sticking and sliding, are distinguished. With the friction coefficient μ, it holds on velocity level

$$T_C = \left\{ (\dot{\boldsymbol{g}}_T, \boldsymbol{\lambda}_T) \in \mathrm{I\!R}^2 \times \mathrm{I\!R}^2; \quad \begin{cases} \|\boldsymbol{\lambda}_T\| \leq \mu|\lambda_N|, & \text{if } \dot{\boldsymbol{g}}_T = \boldsymbol{0} \\ \boldsymbol{\lambda}_T = -\dfrac{\dot{\boldsymbol{g}}_T}{\|\dot{\boldsymbol{g}}_T\|}\mu|\lambda_N|, & \text{if } \dot{\boldsymbol{g}}_T \neq \boldsymbol{0} \end{cases} \right\}, \tag{2.38a}$$

$$T_P = \left\{ (\dot{\boldsymbol{g}}_T, \boldsymbol{\lambda}_T) \in \mathrm{I\!R}^2 \times \mathrm{I\!R}^2; \quad \operatorname*{\mathbf{prox}}_{C_T(\lambda_N)} (\boldsymbol{\lambda}_T - r\, \dot{\boldsymbol{g}}_T) = \boldsymbol{\lambda}_T,\ r > 0 \right\}, \tag{2.38b}$$

$$T_N = \left\{ (\dot{\boldsymbol{g}}_T, \boldsymbol{\lambda}_T) \in \mathrm{I\!R}^2 \times \mathrm{I\!R}^2; \quad -\dot{\boldsymbol{g}}_T \in N_{C_T(\lambda_N)}(\boldsymbol{\lambda}_T) \right\}, \tag{2.38c}$$

with $C_T(\lambda_N) = \{\boldsymbol{x} \in \mathrm{I\!R}^2\ ;\ \|\boldsymbol{x}\| \leq \mu|\lambda_N|\}$. In general, Coulomb's friction law invokes a spatial friction cone, whereof a horizontal cut is shown in Figure 2.5.

The impact laws are the non-smooth analogon to the contact laws. The impulsive percussions $\boldsymbol{\Lambda}$ are used instead of the contact forces $\boldsymbol{\lambda}$. If they are described on velocity level, then the right-limit of the normal gap resp. tangential velocities have to be used

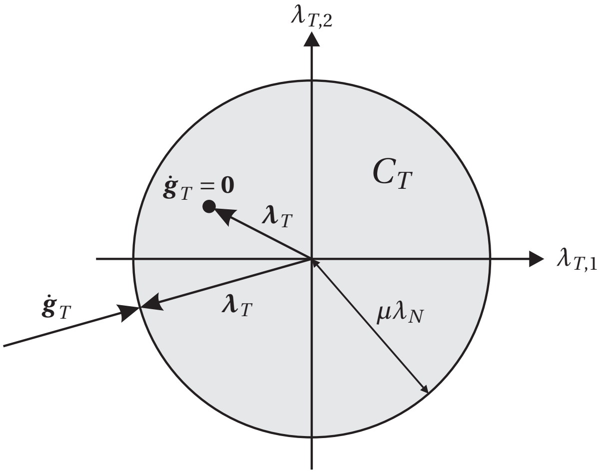

Figure 2.5: Planar cut through Coulomb's friction cone [29, p. 89]

as they effect discontinuities in the velocities. The impact laws are not part of this introduction and are studied in detail e.g. in [6].

Elastic contacts The (rigid) set-valued formulation of the force laws presented here is of course not the only modelling possibility of contact forces. Their goal is to avoid any penetration of the bodies and to allow for possible stick-slip transitions. Single-valued force laws, also called *elastic contacts*, are modelled as alternative spring damper laws. They permit small penetrations and are applied in most commercial multibody simulation software. The original set-valued maps are regularised to obtain single-valued functions. Therefore, they can directly be added into the right hand side of the smooth Newton-Euler equations. No MDEs and no additional constraints are required if only elastic contacts are applied. By these, the elasticity of a rigid body can be considered quasi-statically within the interactions. As disadvantage often stiff ordinary differential equations (ODEs) result because of the required spring stiffness. For some details on single-valued force laws, see [59]. In this study, a combination of set- and single-valued force laws is used depending on the specific contact situation.

2.5 Equations of motion

There are several methods to derive the equations of motion of multibody systems, each with its own advantages and disadvantages. For details on this see e.g. [48, 38]. The projected Newton-Euler formalism results from the prinicple of linear and angular momentum of the single bodies. It will be modularly extendable if the number of bodies is increased. The Euler-Lagrange equations build on energetic principles and may be derived from d'Alembert's principle. They may also arise from Hamilton's principle using the calculus of variations. In this study, Hamilton's principle is shown as it is used to deduce the equations of motion of a Cosserat rod in Section 6.2. It is valid for both, rigid and flexible bodies. The explanation follows [48].

Consider a multibody system with f bodies, then the vector of the generalised coordinates

$$\boldsymbol{q} = \begin{pmatrix} \boldsymbol{q}_1 \\ \vdots \\ \boldsymbol{q}_f \end{pmatrix} \in \mathrm{I\!R}^d \tag{2.39}$$

comprises the generalised coordinates of the single bodies. The dimension d is the sum of the dimensions of the f bodies. The Lagrangian (functional) is defined as

$$L := T - V, \tag{2.40}$$

with the (translatory and rotatory) kinetic energy T and the (strain, curvature and gravitational) potential energy V. Hamilton's principle minimises the integral of the Lagrangian between two points in time

$$\delta \int_{t_1}^{t_2} L \,\mathrm{d}t + \int_{t_1}^{t_2} \delta W^{nc} \,\mathrm{d}t = 0. \tag{2.41}$$

The virtual work δW^{nc} of non-conservative forces is expressed as

$$\delta W^{nc} = (\boldsymbol{Q}^e)^T \delta \boldsymbol{q}, \tag{2.42}$$

with the external generalised forces $\boldsymbol{Q}^e$ and the system virtual displacements $\delta \boldsymbol{q}$. Thus, it follows from calculus of variations

$$\int_{t_1}^{t_2} \left[\frac{\mathrm{d}}{\mathrm{d}\,t} \left(\frac{\partial L}{\partial \dot{\boldsymbol{q}}} \right) - \frac{\partial L}{\partial \boldsymbol{q}} \right] \delta \boldsymbol{q} \,\mathrm{d}t - \int_{t_1}^{t_2} (\boldsymbol{Q}^e)^T \delta \boldsymbol{q} \,\mathrm{d}t = 0. \tag{2.43}$$

Since all δq_j are arbitrary, the following equation results with the fundamental lemma of calculus of variations

$$\frac{\mathrm{d}}{\mathrm{d}\,t} \left(\frac{\partial L}{\partial \dot{\boldsymbol{q}}} \right) - \frac{\partial L}{\partial \boldsymbol{q}} - (\boldsymbol{Q}^e)^T = \boldsymbol{0}^T. \tag{2.44}$$

In mechanical systems (in particular multibody systems) the following dependency is valid [59]

$$L(\boldsymbol{q}, \dot{\boldsymbol{q}}) = T(\boldsymbol{q}, \dot{\boldsymbol{q}}) - V(\boldsymbol{q}). \tag{2.45}$$

Therefore, Equation (2.44) can be simplified to

$$\frac{\mathrm{d}}{\mathrm{d}t}\left(\frac{\partial T}{\partial \dot{\boldsymbol{q}}}\right) - \frac{\partial T}{\partial \boldsymbol{q}} + \frac{\partial V}{\partial \boldsymbol{q}} = (\boldsymbol{Q}^e)^T. \tag{2.46}$$

With an additional damping by the non-conservative dissipation D, the equations of motion of multibody systems are given by

$$\frac{\partial^2 T}{\partial \dot{\boldsymbol{q}}^2}\ddot{\boldsymbol{q}} = (\boldsymbol{Q}^e)^T - \frac{\partial^2 T}{\partial \dot{\boldsymbol{q}}\partial \boldsymbol{q}}\dot{\boldsymbol{q}} + \frac{\partial T}{\partial \boldsymbol{q}} - \frac{\partial V}{\partial \boldsymbol{q}} - \frac{\partial D}{\partial \dot{\boldsymbol{q}}}, \tag{2.47}$$

$$\boldsymbol{M}\ddot{\boldsymbol{q}} = \boldsymbol{h}. \tag{2.48}$$

The terms are summarised in the symmetric positive definite mass matrix $\boldsymbol{M}$ and the generalised force vector $\boldsymbol{h}$. This is the same result as obtained by the Lagrangian formalism. Details on the adding of the constraints to the system (2.47) can be found in [1].

2.6 Flexible bodies

In flexible multibody systems, both rigid and deformable bodies are interconnected. Large and small deformations are distinguished for the flexible bodies corresponding to a geometrical nonlinear resp. linear model. In addition, large and small strains lead to a physical nonlinear or linear theory of elasticity. Further, different discretisation methods for the deformable bodies exist, e.g. the method of finite elements. The equations of motion for rigid and deformable bodies can both be derived with the energetic principles of Section 2.5. For a detailed explanation of flexible multibody systems see [48, 59]. A classification and a review of the literature can be found in [57]. Here, only the different ideas are presented according to [7, 57]. The type of frame used to describe the deformation classifies the models of flexible bodies into three categories. Either an intermediate reference frame or a global inertial frame is used.

The *floating frame formulation* splits up the rigid body motion and the deformation by introducing one floating frame of reference for each flexible body. This intermediate frame is fixed to the flexible body and moves with the mean rigid body motion of it. The deformation is described with respect to the floating frame. This approach is classically used for the simulation of small deformations in combination with a linear material law.

The *co-rotational frame formulation* uses an intermediate frame fixed on each element of the flexible body to describe the deformation. In contrast to the floating frame formulation, in general more than one frame moves with the flexible body. It is assumed, "that the local displacements in the element are small with respect to this frame" [7, p. 22]. The kinematic equations of the elements are linearised, because infinitesimal coordinates are utilised as nodal coordinates. Finite rotations are modelled by a succession of small rotations of the individual elements. Classically, a linear material law is applied. The advantage of this approach is that large deformations can be described. The co-rotated approach is used in this study for the pushbelt CVT model. Therefore, it is illustrated in Figure 2.6 by means of a flexible belt with a number of elements. Their large motion is given by the translation and rotation of the fixed co-rotated frames with respect to the inertial frame. The deformation of each element is described in the intermediate frames.

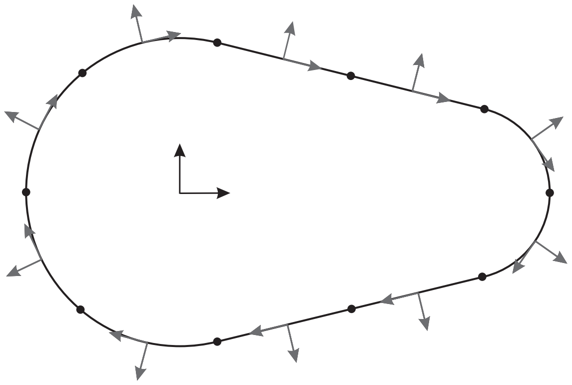

Figure 2.6: Co-rotated frames on flexible belt

The *inertial frame approach* describes both, the rigid body motion and the deformation with absolute nodal translation and rotation coordinates in the global inertial reference frame. One example of this category, the absolute nodal formulation, uses absolute position and gradient coordinates instead of nodal coordinates [48]. Again, it can model the large deformation problem. Further, nonlinear material laws are used.

2.7 Integration schemes

Smooth multibody systems can be represented by standard ODEs resp. differential algebraic equations (DAE). Their numerical solution strategies are almost fully developed, see [21, 4]. The non-smooth counterpart on the other side, especially with a multitude of impacts, has advanced, but is still a research topic today. A very detailed reference explaining the different methods for non-smooth dynamical systems is found in [1]. The solution strategies for MDEs with set-valued force laws can be separated into the three categories event-driven schemes and time-stepping schemes with and without step size control. The first two are described following [46].

Event-driven integration schemes

Event-driven integration schemes track down and calculate the exact periods of transition of the discontinuities and use smooth solvers for the parts in-between. The calculation starts with the smooth solver until the first event. Then, these integration schemes solve the impact equations and laws at the transition time, update the system and again invoke ODE resp. DAE integrators until the next discontinuity, see e.g. [1]. They benefit from all the advantages of the highly advanced smooth solvers, e.g. higher order schemes, step size control and are therefore very accurate. However, as the resolving of the exact transition period is very costly, event-driven integration schemes are only feasible for systems with a small number of discontinuities [46]. That is the reason why they are not used for the described model of the pushbelt CVT system and are not treated further.

Time-stepping integration schemes

Time-stepping integration schemes discretise the MDEs including the constraints with a fixed step size and do not resolve the discontinuities. According to [16] they are robust and efficient in application especially for systems with many discontinuities. However, the applied time-stepping schemes are only of first order. The main methods applied in the pushbelt CVT model is the half explicit time-stepping scheme of [16] on velocity level:

1. Position: $\boldsymbol{q}^{i+1} = \boldsymbol{q}^i + \boldsymbol{T}^i \boldsymbol{u}^i \Delta t$,
2. Active set a: $\mathscr{J} = \left\{ j \in \{1, \ldots, n_c\}; \quad g_{N,j}^{i+1} \leq 0 \right\}$ of all n_c contacts,
3. Velocity and constraints:

$$\boldsymbol{u}^{i+1} = \boldsymbol{u}^i + \boldsymbol{M}(\boldsymbol{q}^{i+1})^{-1} \left(\boldsymbol{h}(\boldsymbol{u}^i, \boldsymbol{q}^{i+1}, t^{i+1}) \Delta t + \boldsymbol{W}_a(\boldsymbol{q}^{i+1}) \boldsymbol{\Lambda}_a^{i+1} \right), \tag{2.49}$$

$$\dot{\boldsymbol{g}}_a^{i+1} = \dot{\boldsymbol{g}}_a^{i+1}(\boldsymbol{u}^{i+1}, \boldsymbol{q}^{i+1}, t^{i+1}), \tag{2.50}$$

$$\boldsymbol{\Lambda}_a^{i+1} = \mathbf{proj}(\dot{\boldsymbol{g}}_a^{i+1}, \boldsymbol{\Lambda}_a^{i+1}). \tag{2.51}$$

The index set $\mathscr{J}$ of all active contacts (index a) at the end of the interval is gained by the gap distances of all unilateral contacts. If a contact closes or opens in-between the interval, it is not considered. The constraints are discretised on velocity level at the end time t_{i+1} for both normal and tangential direction. The unknown contact reactions of active contacts are taken at the end of the time step $\boldsymbol{\Lambda}_a^{i+1}$ to ensure that the contact configuration at the end is again physically consistent, cf. [38]. The set-valued force laws are calculated with the proximal point formulation according to Section 2.4 denoted by **proj**. The r factor inside the **proj** equation is chosen to guarantee a fast converging and stable fixed-point or Newton iteration [16].

Time-stepping schemes with step size control

Usually, time-stepping schemes are integrated with a fixed step size. But recently, a *time-stepping scheme with step size control* was introduced in [22]. No error estimation can be done for the non-smooth case because of discontinuities in the velocities. Thus, the classical step size control is no longer feasible. The different heuristics for a step size control of the non-smooth equations suggested from [22] can be categorised into error tolerances and gap control. For the error tolerances, it is suggested to either exclude the velocities from the step size control and the error estimation or include the velocities scaled with the step size. In addition, a gap control is introduced which is a simple event-detection with different strategies. One can choose between the largest time step, the largest time step fulfilling a given penetration tolerance or the smallest penetration and therefore the smallest time step. The selection of the step size in [22] focuses on robustness and stability rather than accuracy, as for discontinuous sections a real error estimation is not possible. According to the comparisons in [22], the most promising method for the current study is to scale the velocities in combination with the gap control using the largest time step. Higher order schemes gained by the extrapolation method are not used in this study.

2.8 Software MBSim

MBSim [31] is the software for non-smooth dynamical systems developed at the Institute of Applied Mechanics of the Technische Universität München. The basis was laid by the works [16, 59]. An introduction is given in [46]. Practical examples of the used theory can be found in [38, 60]. This software is utilised for the modelling and simulation of the spatial CVT model in this study. The visualisation in this study is done by the Open Multi Body Viewer *OpenMBV* [36] and the plotting by means of *MATLAB*[2].

---

[2] http://www.mathworks.com/products/matlab/

3 Spatial Pushbelt CVT Model

This chapter focuses on the spatial pushbelt CVT model. First, some basics about CVTs are summed up. Then, the model [45] is explained, which is the point of departure for this work.

3.1 Continuously variable transmissions

This section gives a brief view of the global transmission market concerning CVTs and explains its functional principle. According to [35, p. 69], the global trend in transmission manufacturing is heading towards individual solutions instead of one uniform transmission system. This trend is closely connected with the motor market for passenger cars. Just as there is a great variety of automobiles, many competing gear box designs exist today. This diversification was rapid and has been taken place in the last two decades.

3.1.1 Global market

In Europe for example, the predominance of the manual transmission (MT) is declining but persisting. In 1990, one transmission system, the five speed MT, predominated in Europe with about 85% of the market. In 2015, however, the five and six speed MTs together are predicted to have only about 50% market share cf. [35]. This shows clearly the strong competition posed by the other transmission systems forecasted to share the other half of the market. Regarding the CVT in Europe, the customer acceptance is clearly lacking. This is due to a variety of reasons. The lack of knowledge of this concept is one important factor. Thus, most Europeans have never heard of the CVT nor know its advantages. Only a handful of people have already driven an automobile with CVT, most of whom find it unfamiliar, since one does not feel the acceleration in the driver's seat and does not hear the ramping up of the engine while accelerating. These are two important factors for MT drivers. Besides this, the still predominating prejudices about automatic transmissions in Europe (see e.g. [14]) make it even harder for any automatic transmission including the CVT. These handful of reasons show why the breakthrough for the CVT in Europe with a transmission market share of about 3% in 2010 [35] is so difficult.

However, looking at the continents Asia and North America, where primarily automatic transmissions are used, a different picture can be seen. The share of all different kinds of automatic transmissions in passenger cars in the United States of America has been at about 90% and in Japan at about 85% for many years [14]. An opposite situation compared to Europe is found and MTs only play a secondary role. Thus, the CVT does not have to fight against the prejudices about automatic transmissions and has a neutral field to develop. The CVT is gaining more and more importance there. In Japan it already has a market share of about 19% and in North America at least about 6% in the year 2010 cf. [35]. So the CVT is the second most important transmission system in Japan beside the conventional automatic transmission that has a market share of about 60% in the year 2010 [35] [1]. Looking only at the newly produced passenger cars in Japan, [53] states in 2009 that the CVT has a share of 45% and of the (new passenger) cars with a four-cylinder engine already a share of 63%. The true advantages of the CVT are the reason why it succeeds in these areas in such a strong way. The CVT customers value its high driving-comfort (its smooth continuous acceleration) as well as its fuel economy compared to other automatic transmissions. Especially in Japan, the wide distribution can be explained by the specific regional conditions. As the country is only very small, the population drives less on countryside highways with constant speed than in the city with a lot of traffic, varying driving speeds and lots of stop and go. In addition, smaller cars than in Europe or in the US are used. Thereby, the full benefits of the CVT can be exploited. Nevertheless, the newest generations of CVTs are not restricted to smaller cars. They can now handle engines with up to 400 N m of torque cf. [52].

Leaving this global view of the CVT market, the following text leads to the functional principle of CVTs, which is as simple as it is ingenious. The idea already originates from the 15th century from Leonardo da Vinci. About 400 years later (ca. 1900), the CVT was introduced into the automotive industry, cf. [8], where some milestones in the history of development of CVTs can be found. The functional principle is based on a simple idea, however, it leads to complex processes which is underlined by the still ongoing research concerning CVTs.

3.1.2 Functional principle

A general transmission is defined according to [25, p. 9] as a machine element that transmits mechanical power and thereby transforms forces resp. torques and velocities resp. angular velocities. A CVT is a special automatic transmission for vehicles. In contrast to other transmissions, CVTs transfer power continuously without interruption as no discrete ratios are used. The main advantage of the CVT is the optimal usage of the area between the largest and smallest transmission ratio [14, p. 10]. Consequently, the engine can generate the required power for each driving speed always in its optimal operating point concerning economy or performance, cf. [8]. This means, as an example, that the vehicle can be accelerated at the same engine speed only by changing the transmission ratio [25, p. 131 f.]. Thereby, the fuel consumption and emissions are

---

[1] Note, that these numbers from [35] on the year 2010 are based on predictions although the 2nd edition of the book was published in 2011.

reduced using mainly the large overdrive area to operate the engine at low speeds. Actually, the CVT is only competitive through this shifting of the engine into its optimal operating point, as it compensates for its slightly reduced efficiency compared to gear transmissions cf. [25, p. 132]. A further advantage is the additional comfort resulting from no gear shifts while changing the transmission ratio and the resulting continuous acceleration.

CVTs exist in mechanical, electrical and hydraulic versions. Here, only the most commonly used variant with mechanical power transmission is explained which is realised through friction. Three different mechanical CVTs are illustrated in Figure 3.1 - the pushbelt, chain and toroid CVT. For series-produced passenger cars usually belt drives with variable pulleys are utilised [35]. Belt drives can again be subdivided into a flexible belt, a tension-based chain and a pushbelt. The differences between these groups are explained e.g. in [24].

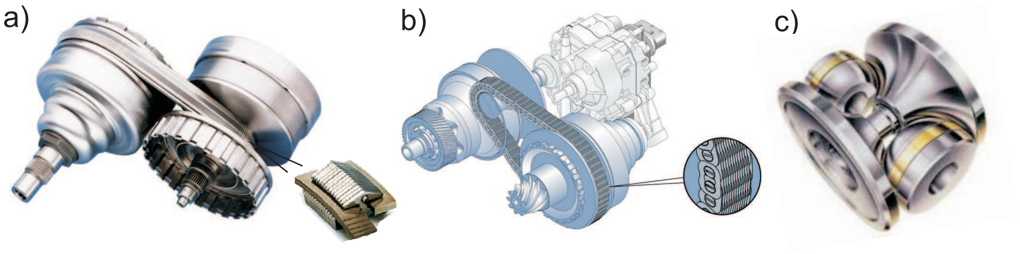

Figure 3.1: Different kinds of CVTs: a) pushbelt, b) chain and c) toroid [8, p. 15]

In belt drives, the belt runs between two pulleys, i.e. the primary and secondary pulley. Each pulley has two conical V-shaped sheaves. One of them is axially movable by a hydraulic pressure and thus called the loose sheave. The other sheave is fixed. To minimise the misalignment, the two loose sheaves are built on opposite sides of the pulleys, cf. Figure 3.6. To ensure enough friction between belt and pulley for a power transmission, the pressure on the belt is controlled by a clamping force. The right pressure is critical, as a too high pressure would lead to less efficiency and a too low pressure to a slipping of the belt, which would result in scuffing cf. [35, p. 187]. The continuous change of the transmission ratio is done reciprocally. The pushbelt is forced to a new running radius by increasing the sheave distance on one pulley and simultaneously decreasing it on the other pulley. Within this study the focus is on the variator with a pushbelt developed by Van Doorne (today Bosch Transmission Technology), see Figure 3.2. It consists of two steel ring sets, each with 9 - 12 ring layers, which guide about 400 steel elements. The power transmission in the pushbelt is achieved mainly by push forces between the elements and secondary by tension through the ring sets.

Figure 3.2: Bosch's pushbelt CVT variator [5]

3.2 Modelling background

The point of departure for this work is the model [45] which is explained following [9, 45] to give the necessary background information. The model is based on the theory of non-smooth flexible multibody system dynamics presented in Section 2. Hence, the model description can be divided into the modelling of the different bodies and the associated interactions like e.g. contacts.

3.2.1 Bodies

The pushbelt CVT is modelled with three different bodies with inertia, the elements, the ring sets and the pulley sheaves, see Figure 3.2. The shaft is modelled as a joint between two sheaves of one pulley which secures the same angular velocity. Its inertia is added to the sheaves.

Elements

The slender elements are modelled as rigid bodies. Each element has six rigid degrees of freedom (DOFs) for the spatial motion. The centre of gravity is defined by three translational DOFs. Three Cardan angles model the rotation. Elasticity is considered only in the interactions quasi-statically. The number of elements in the model (N_E) can be freely chosen. As this number can be different than the number of elements in reality (N_{E_0}), all parameters depending on the thickness of the elements are scaled with N_{E_0}/N_E, see [45]. The element is depicted in Figure 3.3 with the element reference coordinate system situated in the centre of gravity C. The names of the different parts of the elements can also be found in that figure.

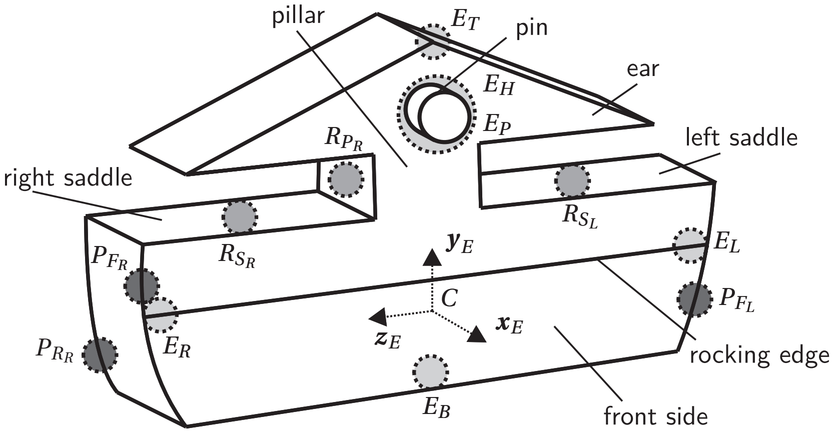

Figure 3.3: Element - with reference coordinate system [45, p. 14]

Ring sets

The ring sets have to be modelled by spatial flexible bodies with large deformation as they deform strongly while running from one straight part into a pulley and out of the pulleys into the other straight part. A dynamic geometrical nonlinear beam model with large translations and deflections has been chosen. The material laws, however, are modelled linearly. The relative motion of the different ring layers in one ring set is neglected and one ring with width $\tilde{w}_R$ and height $\tilde{h}_R$ represents the ring set for each side, see Figure 3.4. Its area moment of inertia, however, considers the structure with different layers without internal friction. With the neutral fibre and its Frenet frame the motion of the beam is characterised.

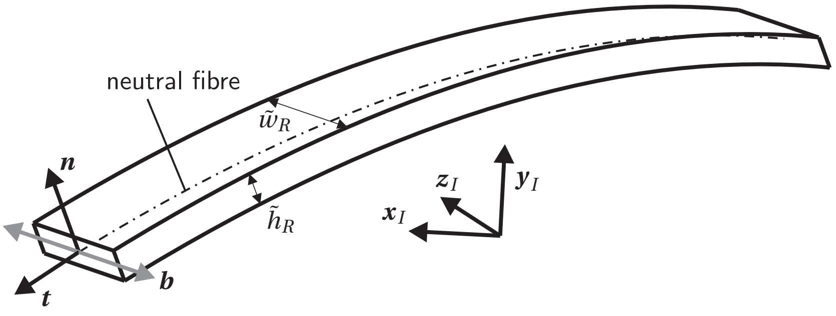

Figure 3.4: One ring set [45, p. 20]

One ring set is separated into $\tilde{N}_B$ beams with large deformation. For each one the Euler-Bernoulli beam theory in connection with a co-rotational approach has been applied. The entire ring is modelled so that the coordinate systems of the finite elements run with the belt and are not at a fixed position concerning the inertial frame, which is the idea of the co-rotational approach. Two coordinate sets - an internal and a global one - are used. Each of this coordinate sets is utilised in the area where it has its advantages. As only one coordinate set is enough, the method is called *redundant coordinate method* (RCM). The rotation is described by a reversed Cardan parameterisation [45], i.e. Cardan angles with a reversed rotation sequence ($z-y-x$). The multibody equations of motion for each element are set in the internal coordinates $\boldsymbol{q}_i$ according to the Lagrange II formalism. This decouples the rigid and elastic body motion and leads to compact equations of motion [45].

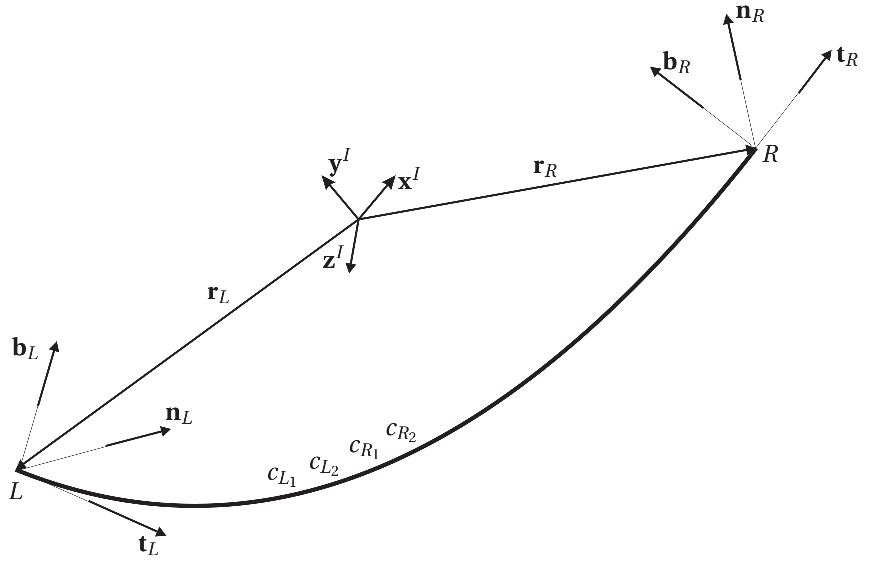

Figure 3.5: Global coordinates of redundant coordinate method [45, p. 22]

For the assembling, ideas of the finite element method are utilised. Thereby, the global coordinates

$$\boldsymbol{q}_g := \left(x_L, y_L, z_L, \varphi_{L0}, \varphi_{L1}, \varphi_{L2}, c_{L_1}, c_{R_1}, c_{L_2}, c_{R_2}, x_R, y_R, z_R, \varphi_{R0}, \varphi_{R1}, \varphi_{R2}\right)^T \quad (3.1)$$

are used with the rigid coordinates at the boundaries of each finite element, cf. Figure 3.5. Hence, constraint equations are bypassed and a minimal representation of the system is gained. The global coordinates are, in addition, used for the contact calculation. The transformation between the two coordinate sets results in a nonlinear system of equations

$$\boldsymbol{F}(\boldsymbol{q}_i, \boldsymbol{q}_q) = 0, \quad (3.2)$$

which has to be solved in each time step numerically using a Newton solver. The solver does not find a solution if the time step size is too large. So the step size is restricted by this solution process. As a compromise only 12 finite elements are used for each ring set which is actually a too coarse discretisation. This is a real drawback of this approach. In addition, damping strategies have been implemented into the model.

Pulleys

The pulley sheaves are modelled as rigid bodies and elasticity is taken into account quasi-statically in the interactions. Each pulley consists of two sheaves, a fixed (FS) and a loose (LS) one, which are arranged opposite, see Figure 3.6. The loose sheaves have three DOFs for rotation (axial rotation as well as tilting) and one for the translation in axial direction. The fixed sheaves have one DOF for rotation around the z-axis. The inertial frame (I) is positioned at the centre of the secondary pulley. The sheaves' centres of gravity are denoted by C. The inertia of the shafts is considered in the inertia tensors of the sheaves.

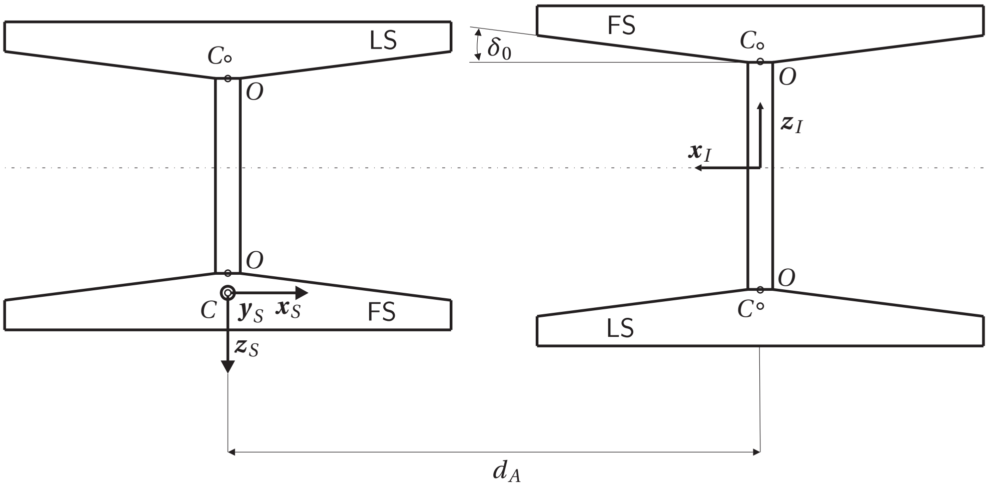

Figure 3.6: Pulleys and inertial frame [45, p. 27]

3.2.2 Interactions

One element can be in contact with the two neighbouring elements, both ring sets and each pulley sheave. As the contact configuration and position can change with time, the contact kinematics have to be calculated at each time step. Hence, the contact modelling was chosen for each combination in a simple analytical way to reduce the computing time, yet, simultaneously to secure a high accuracy.

Element - element contacts

There are five different element - element contact possibilities. One element can be in contact with the plane rear side of the predecessor at the element top E_T and at the element bottom E_B, cf. Figure 3.3. Two circular arcs at the rocking edges, at E_R and E_L, enable a rolling up. The pin-hole contact (E_P - E_H) centres the elements and is modelled by a circle - frustum contact. Hence, the relative movement between the elements is minor and the contacts are described without friction. As the elements can detach, all five contacts are unilateral with a flexible force law which considers the elasticity of the elements in contact.

Element - ring set contacts

The element - ring set contacts are modelled as point - flexible band contacts. The flexible band is situated around the neutral fibre of the beams in half width resp. half height distance in binormal resp. normal direction, see Figure 3.4. On each side of the element two contact points at the saddle R_S and the pillar R_P guide the two ring sets without detaching. A mutual rotational dependence is omitted. The contacts are bilateral rigid with friction in longitudinal direction at the saddle.

Element - pulley contacts

The two circular arcs at the front and rear side of each element, P_F and P_R, are in contact with the frustum sheaves. The contacts are modelled unilateral flexible with spatial friction. Hence, the elasticity is considered within the contact. Altogether, friction torques and clamping can be described. The tilting of the loose sheaves and the axial stiffness of the elements enable a representation of the spiral running. However, the elements in contact are not coupled by the elasticity of the sheave.

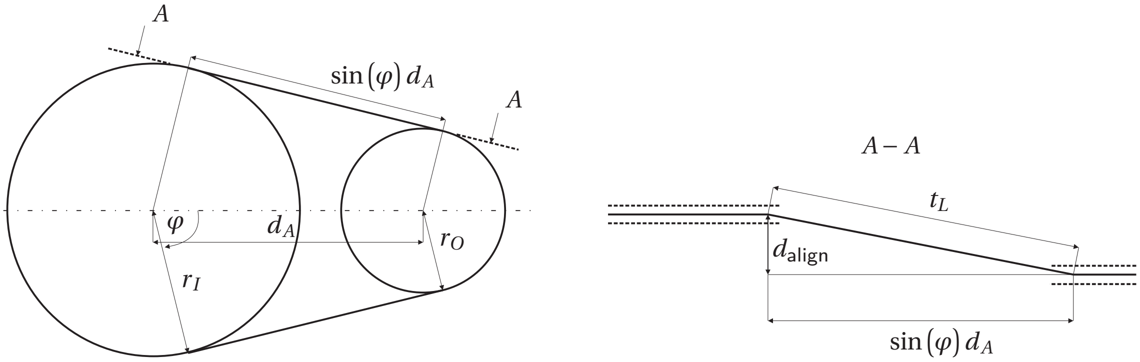

Figure 3.7: Kinematic initialisation (axial view and view A-A) [45, p. 48]

3.2.3 Initialisation

The initialisation is done by a kinetic planar belt model [44] for the case of a kinetic boundary setting at the secondary and a kinematic setting at the primary pulley. The velocity is initialised out of this model to represent stationary cases, which is the main focus of the model. Run-up cases can also be depicted but require a much higher computing time. The kinematic initialisation is done by a simple geometric calculation as shown in Figure 3.7. By means of a nonlinear system solver, the angle φ and the two radii of primary and secondary, r_I and r_O, are calculated considering the misalignment. This reference line is utilised to initialise the neutral fibre of the two ring sets. Then, the elements are uniformly distributed over the ring sets and the sheave position is adapted to the specified boundary conditions.

A first validation of the model with measurements has been done resulting in good correlations. But still a large room for improvements was present.

4 Enhancements concerning Initialisation

After these two introductory chapters, the explanation of the different model enhancements of this study starts in this chapter. It combines three enhancements which are linked to the initialisation of the CVT model. First, variable CVT boundary conditions enable the presetting of a multiplicity of new boundary specifications for primary and secondary pulley to operate and test the CVT model in different situations. This model enhancement causes a new belt velocity initialisation resulting from a kinetic model. Second, tapered elements i.e. a changed element geometry lead to a revised geometric or kinematic initialisation. The overall initialisation process is explained in detail here. Third, a planar pre-integration concept is shown focusing on computing time which results in a numerical initialisation of the spatial model. Note that the three enhancements affect not only the initialisation but the whole simulation, e.g. a changed element geometry changes the motion of single elements and therefore the overall dynamics. However, the model changes are mainly located in the area of the initialisation.

4.1 Variable boundary conditions

The pulley sheaves are the chosen model border in [45]. At the pulleys, the boundary conditions - kinematic values (positions, speeds) and kinetic values (forces, torques) - have to be specified. They define the pulley - environment interaction, i.e. the operating mode of the pushbelt CVT. The boundary conditions are illustrated in Figure 4.1 for the so-called two extreme transmission settings LOW and OD. The boundary conditions are specified by means of a timetable to also simulate running-up cases. This table is linearly interpolated.

For the variable boundary conditions, the structure of describing the input parameters on primary and secondary pulley had to be revised. This has been done together with the help of the student assistant Kilian Grundl. The new framework makes it possible to define on each pulley (primary or secondary) one rotational and one translational input. The rotational input can either be kinematic - an angular velocity - or kinetic - a torque. In the same way, the translational input can either be kinematic - an end stop - or kinetic - a clamping force. This distinction is made by means of a rotational and a translational switch specified by the user. An end stop describes the position z_C of the loose sheave. As the positions of the loose sheaves are already gained by the kinematic initalisation process of [45], the clamping velocity $\dot{z}_C$ of the loose sheave (in the following called end stop) is defined instead of the position. To secure the same angular velocity for both sheaves of one pulley, a shaft is used to connect the two sheaves.

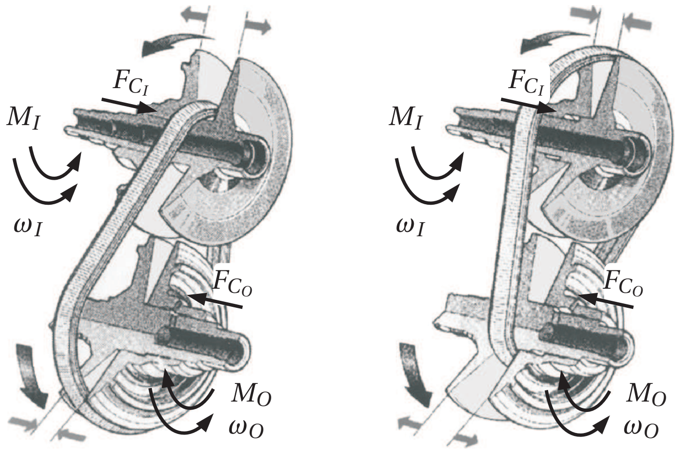

Figure 4.1: Boundary conditions for LOW and overdrive (OD) [17, p. 30]

Both sheaves of one pulley are fixed with a bilateral rotational joint around the rotating axis of the shaft. The rotational input - angular velocity resp. torque - is now applied directly to the shaft of each pulley. The translational input - end stop or clamping force - is applied only to the loose sheave of each pulley. Thus, the shafts and loose sheaves are the system borders between the model and the environment similar to [17].

In the pushbelt CVT model [45] it was possible to predefine a kinetic setting at the secondary pulley (i.e. secondary torque and clamping force) in combination with a kinematic setting at the primary pulley (i.e. primary angular velocity and end stop velocity) as well as a geometric transmission ratio. This boundary condition represents only one specification of pulley-environment interaction whereby not the entire range of operation of the CVT is covered. Therefore, the model has been enhanced by increasing the options for prescribing load conditions on the model to the six different cases in Table 4.1. They can be classified into the triplet

- primary end stop
- secondary end stop
- without end stop

each in combination either with secondary torque or with secondary speed. The restriction to these six practical relevant cases has been done in agreement with the industrial partner. Hence, primary and secondary end stop cases as well as cases with primary torque are not considered.

The main challenge in adding more boundary conditions to the model is the belt velocity initialisation. For the simulation of stationary and shifting cases, an advanced model for the velocity initialisation is required to avoid unnecessary computing time needed for a run-up simulation. For this purpose the Sattler model from [44] is utilised, which is an analytic stationary kinetic belt model. It describes a planar continuum belt

Table 4.1: Variable CVT boundary settings

Description	secondary torque	secondary speed
primary end stop	$\omega_I,\, \dot{z}_{C_I} \mid M_O,\, F_{C_O}$	$\omega_I,\, \dot{z}_{C_I} \mid \omega_O,\, F_{C_O}$
secondary end stop	$\omega_I,\, F_{C_I} \mid M_O,\, \dot{z}_{C_O}$	$\omega_I,\, F_{C_I} \mid \omega_O,\, \dot{z}_{C_O}$
without end stop	$\omega_I,\, F_{C_I} \mid M_O,\, F_{C_O}$	$\omega_I,\, F_{C_I} \mid \omega_O,\, F_{C_O}$

with longitudinal elasticity by means of an ODE system, resulting from the balance of forces. In contrast to a pushbelt, it works only with tensile and not push forces.

The kinematic setting for the initalisation is calculated in [45, p. 48 f.] with a simple geometric model resulting in the circular measure angle φ and both radii r_I as well as r_O with a given initial transmission ratio

$$i_r = \frac{r_O}{r_I}. \tag{4.1}$$

The kinetic Sattler model, capable to calculate the admissible torque capacity and necessary clamping forces of a CVT, has been modified in [45] to initialise the belt velocity v. The velocity of the undeformed part is denoted with v_0. The model was simplified to an Euler-Eytelwein description for the longitudinal force L [45, p. 53]

$$L(\theta) = [L_0 - K]\, \mathrm{e}^{\pm\mu^*(\theta-\theta_0)} + K, \tag{4.2}$$

with

$$\mu^* := \frac{\mu}{\sin(\delta_0)}, \quad K := \frac{m^* v_0^2 EA}{EA - m^* v_0^2}\,. \tag{4.3}$$

The parameters according to [45] are the cross-section A, Young's Modulus E, the friction coefficient μ and the undeformed belt's local mass distribution m^*. The half wedge angle δ_0 is illustrated in Figure 3.6. This description results in nonlinear equations instead of an ODE system as it is the case in [44]. The longitudinal force equivalence for the setting of Figure 4.2 is given by [45]

$$L_{O_{in}} = L_{I_{out}} = [L_{O_{in}} - K]\mathrm{e}^{\mu^*(\Phi_O-\Phi_I)} + K, \tag{4.4}$$

with the angles of the active parts Φ. The modification of [45] is the basis for the following enhancements which were accomplished together with student assistant Zhan Wang.

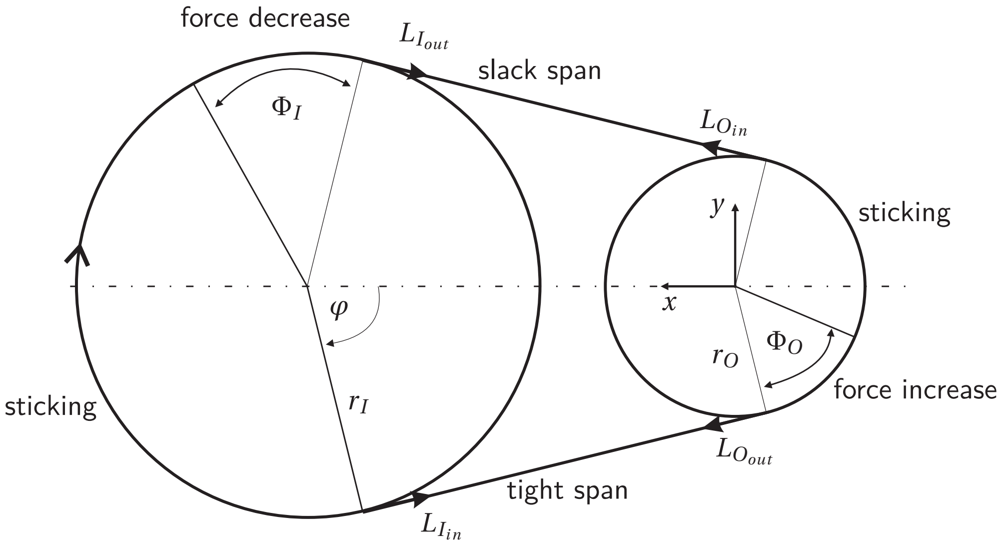

Figure 4.2: Belt kinematics (adapted after [45])

4.1.1 Primary end stop

The end stop at one pulley always occurs in combination with the clamping force at the other pulley, see Table 4.1. In the CVT boundary situation with primary end stop, the input parameters are:

Primary end stop $\dot{z}_{C_I}$ and secondary clamping force F_{C_O} with either

- primary angular velocity ω_I and secondary torque M_O or
- primary angular velocity ω_I and secondary angular velocity ω_O.

In the modified Sattler model of [45, p. 54], the two unknowns ω_O and v_0 are gained by the solution of two nonlinear equations. The first equation results from the sticking condition at the primary pulley

$$r_I \omega_I = v_0 \left[1 + \frac{\left(L_{O_\mathrm{in}} - K\right) \mathrm{e}^{\mu^* \Phi_O} + K}{EA} \right], \tag{4.5}$$

and the second equation is gained by the axial equality of forces at the secondary pulley

$$F_{C_O} = \frac{EA - m^* v_0^2}{2 \tan(\delta_0) EA} \left[2 L_{O_\mathrm{in}} \varphi + \left(L_{O_\mathrm{in}} - K\right) \left(\frac{\mathrm{e}^{\mu^* \Phi_O} - 1}{\mu^*} - \Phi_O \right) \right] - \frac{m^* v_0^2 \varphi}{\tan(\delta_0)}. \tag{4.6}$$

The active wrapped angle at the secondary pulley is given by

$$\Phi_O = \frac{1}{\mu^*} \ln \left[\frac{M_O}{r_O \left(L_{O_\mathrm{in}} - K\right)} + 1 \right]. \tag{4.7}$$

This set of equations has been simplified significantly in the current study to ease the basis equations of the variable boundary conditions resulting in only one nonlinear equation. This equation transformation process is shown below.

Simplification of the two equations

Starting with the simplification of Equation (4.5), the equality of torques at the secondary pulley is given by [45, p. 54]

$$M_O = r_O(L_{O_{out}} - L_{O_{in}}) \; . \tag{4.8}$$

In the same way, the primary torque can be described by

$$M_I = r_I(L_{I_{out}} - L_{I_{in}}) \; , \tag{4.9}$$

cf. Figure 4.2. The longitudinal forces at the end of one pulley and at the beginning of the other are equal $L_{O_{in}} = L_{I_{out}}$ and $L_{O_{out}} = L_{I_{in}}$, because the longitudinal force remains constant in the straight parts [44]. Thereby, a relation between the two torques can be derived depending on the initial geometric transmission ratio

$$M_O = -\frac{r_O}{r_I} M_I \; . \tag{4.10}$$

By substituting Equation [45, (2.210)] in the following form

$$\left(L_{O_{in}} - K\right) e^{\mu^* \Phi_O} = \frac{M_O}{r_O} + \left(L_{O_{in}} - K\right) \tag{4.11}$$

and Equation [45, (2.212)]

$$L_{O_{in}} = \frac{EAr_O\omega_O}{v_0} - EA \tag{4.12}$$

into (4.5), the nonlinear equation can be simplified into a linear relationship

$$r_I\omega_I = \frac{v_0 M_O}{EAr_O} + r_O\omega_O \; . \tag{4.13}$$

For the simplification of (4.6), Equation [45, (2.210)] can be reformulated to

$$\left(L_{O_{in}} - K\right)\left(e^{\mu^* \Phi_O} - 1\right) = \frac{M_O}{r_O} \; . \tag{4.14}$$

From the definition of $L_{O_{in}}$ in (4.12) and of K in (4.3) another preparatory formula results in

$$\frac{\left(L_{O_{in}}-K\right)}{EA}=\frac{r_O\omega_O}{v_0}-\frac{EA}{EA-m^*{v_0}^2}. \tag{4.15}$$

Using the relationships (4.14), (4.15) and (4.12), Equation (4.6) can be simplified to

$$\begin{aligned}2F_{C_O}\tan(\delta_0)=\left(EA-m^*{v_0}^2\right)\Bigg[2\varphi\left(\frac{r_O\omega_O}{v_0}-1\right)+\frac{M_O}{\mu^* r_O EA}\\ -\left(\frac{r_O\omega_O}{v_0}-\frac{EA}{EA-m^*{v_0}^2}\right)\Phi_O\Bigg]-2m^*{v_0}^2\varphi\,.\end{aligned} \tag{4.16}$$

Combination of the two equations

For the additional five boundary conditions, the two Equations (4.13) and (4.16) are combined into one equation depending only on the two angular velocities and the belt velocity. Therefore, the definition of the active wrapped angle at the secondary pulley has to be expressed in forms of ω_I, ω_O and v_0 by solving (4.13) for M_O:

$$M_O=\frac{(r_I\omega_I-r_O\omega_O)r_O EA}{v_0}\,. \tag{4.17}$$

By inserting (4.15) and (4.17) into Equation (4.7), a transformed formulation for Φ_O is obtained

$$\Phi_O=\frac{1}{\mu^*}\ln\left[\frac{r_I\omega_I(EA-m^*{v_0}^2)-EAv_0}{r_O\omega_O(EA-m^*{v_0}^2)-EAv_0}\right]. \tag{4.18}$$

Substituting (4.17) in (4.16), one general nonlinear equation is derived

$$\begin{aligned}2F_{C_O}\tan(\delta_0)=\left(EA-m^*{v_0}^2\right)\Bigg[2\varphi\left(\frac{r_O\omega_O}{v_0}-1\right)+\frac{r_I\omega_I-r_O\omega_O}{\mu^* v_0}\\ -\left(\frac{r_O\omega_O}{v_0}-\frac{EA}{EA-m^*{v_0}^2}\right)\frac{1}{\mu^*}\ln\left[\frac{r_I\omega_I(EA-m^*{v_0}^2)-EAv_0}{r_O\omega_O(EA-m^*{v_0}^2)-EAv_0}\right]\Bigg]\\ -2m^*{v_0}^2\varphi.\end{aligned} \tag{4.19}$$

As (4.19) depends only on the two angular velocities and the belt velocity, it can be used for all boundary conditions where F_{C_O} and ω_O is given as an input parameter. If the secondary torque is specified instead of the secondary angular velocity, Equation (4.13) can be solved for ω_O:

$$\omega_O=\frac{r_I\omega_I}{r_O}-\frac{v_0 M_O}{EA{r_O}^2}\,. \tag{4.20}$$

Therefore, it becomes possible to also solve the boundary case with primary end stop and secondary torque from Table 4.1 with (4.19). Finally, it depends only on the unknown v_0 and can be solved e.g. by a one-dimensional Newton method. The starting value for v_0 in the case of a secondary torque unequal to zero is taken from the special case of a secondary torque equal to zero (4.22).

Special case of a secondary torque equal to zero

In the special case of a zero torque at the secondary pulley, the calculation of v_0 is simplified cf. [45, p. 55f.]. It is $\Phi_I = \Phi_O = 0$, $F_{C_O} \neq 0$, $L_{I_{in}} = L_{O_{in}} \neq 0$ and a quadratic equation for v_0 is obtained:

$$r_I \omega_I \varphi m^* {v_0}^2 + (F_{C_O} \tan(\delta_0) + EA\varphi) v_0 - EA r_I \omega_I \varphi = 0. \tag{4.21}$$

As the velocity is always greater or equal to zero, $v_0 \geq 0$, the quadratic equation in (4.21) can easily be solved analytically, cf. [45, p. 55]:

$$v_0 = \frac{\sqrt{\left(F_{C_O} \tan(\delta_0) + EA\varphi\right)^2 + 4EAm^* r_I^2 \omega_I^2 \varphi^2} - EA\varphi - F_{C_O} \tan(\delta_0)}{2m^* r_I \omega_I \varphi}\,. \tag{4.22}$$

4.1.2 Secondary end stop

For the situation with secondary end stop the following boundary parameters are given: Primary clamping force F_{C_I} and secondary end stop $\dot{z}_{C_O}$ with either

- primary angular velocity ω_I and secondary torque M_O or
- primary angular velocity ω_I and secondary angular velocity ω_O.

All equations can be derived for this situation similar to the previous subsection resulting in one formula for F_{C_I} where both cases with secondary end stop of Table 4.1 are covered.

Equation for primary clamping force

The sticking equation [45, (2.208)] for the primary pulley can be reformulated to

$$L_{I_{in}} = \frac{EA r_I \omega_I}{v_0} - EA\,, \tag{4.23}$$

and the relationship of $L_{I_{out}}$ and $L_{I_{in}}$ is expressed by the Euler-Eytelwein Equation (4.2)

$$L_{I_{out}} - L_{I_{in}} = (L_{I_{in}} - K)(e^{-\mu^* \Phi_I} - 1). \tag{4.24}$$

As the longitudinal force decreases from $L_{I_{in}}$ to $L_{I_{out}}$, the negative sign has to be chosen for the exponent. With (4.24), the equilibrium of torques at the primary pulley satisfies

$$M_I = r_I(L_{I_{out}} - L_{I_{in}}) = r_I(L_{I_{in}} - K)(e^{-\mu^*\Phi_I} - 1)\ . \tag{4.25}$$

Finally, the axial equality of forces on the primary pulley is the integral over the derivative of the sheave expansion force S (cf. [45])

$$\begin{aligned}
F_{C_I} &= -\int\limits_{\varphi_I} S'\,\mathrm{d}\theta \\
&= -\int\limits_{\varphi_I} \frac{L(EA - m^* {v_0}^2) - m^* {v_0}^2 EA}{2\tan(\delta_0)EA}\,\mathrm{d}\theta \\
&= -\frac{EA - m^* {v_0}^2}{2\tan(\delta_0)EA}\int\limits_{-(\pi-\varphi)}^{\pi-\varphi} L\,\mathrm{d}\theta + \frac{m^* {v_0}^2(\pi-\varphi)}{\tan(\delta_0)} \\
&= -\frac{EA - m^* {v_0}^2}{2\tan(\delta_0)EA}\left[2L_{I_{in}}(\pi-\varphi) + (L_{I_{in}} - K)\left(\frac{e^{-\mu^*\Phi_I} - 1}{-\mu^*} - \Phi_I\right)\right] + \frac{m^* {v_0}^2(\pi-\varphi)}{\tan(\delta_0)}.
\end{aligned} \tag{4.26}$$

Thereby, the integral over the longitudinal force has been split into a constant and non constant part

$$\begin{aligned}
\int\limits_{-(\pi-\varphi)}^{\pi-\varphi} L\,\mathrm{d}\theta = \int\limits_{-(\pi-\varphi)}^{\pi-\varphi-\Phi_I} L\,\mathrm{d}\theta \qquad &+ \int\limits_{\pi-\varphi-\Phi_I}^{\pi-\varphi} L\,\mathrm{d}\theta \\
= L_{I_{in}}(2\pi - 2\varphi - \Phi_I) \quad &+ \int\limits_{\pi-\varphi-\Phi_I}^{\pi-\varphi} \left((L_{I_{in}} - K)e^{-\mu^*(\theta-(\pi-\varphi-\Phi_I))} + K\right)\mathrm{d}\theta.
\end{aligned} \tag{4.27}$$

Equation (4.26) can be simplified similar to (4.16) resulting in

$$\begin{aligned}
2F_{C_I}\tan(\delta_0) = -\left(EA - m^* {v_0}^2\right)\Bigg[2(\pi-\varphi)\left(\frac{r_I\omega_I}{v_0} - 1\right) + \frac{M_I}{(-\mu^*)r_I EA} \\
-\left(\frac{r_I\omega_I}{v_0} - \frac{EA}{EA - m^* {v_0}^2}\right)\Phi_I\Bigg] + 2m^* {v_0}^2(\pi-\varphi).
\end{aligned} \tag{4.28}$$

Combination of the two equations

Again (4.13) is combined with (4.28). This time the torque ratio (4.10) is used to express the unknown primary torque. If $M_I \neq 0$, then the secondary torque is also unequal to zero, as the ratio of the radii cannot be zero in (4.10). If the torque at the secondary pulley is unequal to zero, $M_O \neq 0$, this necessarily implies $\Phi_I = \Phi_O$ and $L_{O_{in}} \neq K$, see [45].

Therefore, Equation (4.25) can be solved for the active wrapped angle at the primary pulley

$$\Phi_I = -\frac{1}{\mu^*} \ln\left[\frac{M_I}{r_I(L_{I_{in}} - K)} + 1\right]. \tag{4.29}$$

The argument of the natural logarithm has to be greater than zero, hence it is only defined for $M_I \geq r_I(K - L_{I_{in}})$. Analogously to (4.18), Equation (4.29) can be transformed to

$$\Phi_I = \frac{1}{-\mu^*} \ln\left[\frac{r_O\omega_O(EA - m^* {v_0}^2) - EAv_0}{r_I\omega_I(EA - m^* {v_0}^2) - EAv_0}\right]. \tag{4.30}$$

Finally, Equation (4.28) can be expressed depending only on the velocities ω_I, ω_O and v_0:

$$\begin{aligned} 2F_{C_I}\tan(\delta_0) = &-\left(EA - m^* {v_0}^2\right)\Bigg(2(\pi-\varphi)\left(\frac{r_I\omega_I}{v_0} - 1\right) + \frac{r_O\omega_O - r_I\omega_I}{-\mu^* v_0} \\ &- \left(\frac{r_I\omega_I}{v_0} - \frac{EA}{EA - m^* {v_0}^2}\right)\frac{1}{-\mu^*}\ln\left[\frac{r_O\omega_O(EA - m^* {v_0}^2) - EAv_0}{r_I\omega_I(EA - m^* {v_0}^2) - EAv_0}\right]\Bigg) \\ &+ 2m^* {v_0}^2(\pi - \varphi). \end{aligned} \tag{4.31}$$

Equation (4.31) can be used for both cases with secondary end stop. In the case where the secondary torque is specified, ω_O has to be substituted by M_O by means of (4.20). As a result, Equation (4.31) depends only on the unknown v_0 and can be solved with the starting value provided by the following special case (4.33).

Special case of a secondary torque equal to zero

If the torque at the secondary pulley is equal to zero, again the equation for v_0 results in a quadratic relationship. Under the conditions $\Phi_I = \Phi_O = 0$, $F_{C_I} \neq 0$ and $L_{I_{in}} \neq 0$, cf. [45], it follows

$$r_O\omega_O(\pi - \varphi)m^* {v_0}^2 + (-F_{C_I}\tan(\delta_0) + EA(\pi - \varphi))v_0 - EAr_O\omega_O(\pi - \varphi) = 0. \tag{4.32}$$

And as $v_0 \geq 0$, solving (4.32) results in

$$\begin{aligned} v_0 = &\frac{\sqrt{\left(-F_{C_I}\tan(\theta_0) + EA(\pi - \varphi)\right)^2 + 4EAm^* {r_O}^2{\omega_O}^2(\pi - \varphi)^2}}{2m^* r_O\omega_O(\pi - \varphi)} \\ &+ \frac{-EA(\pi - \varphi) + F_{C_I}\tan(\delta_0)}{2m^* r_O\omega_O(\pi - \varphi)}. \end{aligned} \tag{4.33}$$

4.1.3 No end stop

In the cases without end stop, both clamping forces are specified. The following combinations have been chosen:

Primary clamping force F_{C_I} and secondary clamping force F_{C_O} with either

- primary angular velocity ω_I and secondary torque M_O or
- primary angular velocity ω_I and secondary angular velocity ω_O.

For the calculation of v_0 the equation for primary clamping force (4.31) and secondary clamping force (4.19) are used together. This is in contrast to the cases with end stop where only one equation for one clamping force was given. This results in an overdetermined nonlinear system with two equations and one unknown. As the initial radii from the kinematic initialisation change due to the two given clamping forces, they have to be adapted. Hence, one kinematic equation is added to the kinetic initialisations and a nonlinear system with three equations and three unknowns is gained. The original two equations with the two unknowns r_I and φ from the kinematical initialisation of [45, p. 48] are substituted into one equation, to add one equation and two unknowns to the nonlinear system. The relation between the transmission radii is solved for r_I

$$r_I = r_O + \cos(\varphi) d_A, \tag{4.34}$$

cf. Figure 3.7. The total length of the ring sets $\tilde{l}_R$ is composed of the four curve sections of the geometric setting in the non-tapered cases

$$\tilde{l}_R = 2t_L + b_I + b_O. \tag{4.35}$$

The lengths of the upper and lower straight part t_L, the primary arc b_I as well as the secondary arc b_O are given by [45]

$$t_L = \sqrt{\sin^2(\varphi) d_A^2 + d_{align}^2}, \tag{4.36}$$

$$b_I = 2r_I(\pi - \varphi), \tag{4.37}$$

$$b_O = 2r_O\varphi, \tag{4.38}$$

with the alignment d_{align} and the distance of the axes d_A, cf. Figure 3.7. Substituted with the relation (4.34), Equation (4.35) can be reduced to the unknown secondary transmission radius r_O and φ. The additional nonlinear equation yields

$$2\left(\sqrt{\sin^2(\varphi) d_A^2 + d_{align}^2} + r_O\pi + \cos(\varphi) d_A(\pi - \varphi)\right) - \tilde{l}_R = 0. \tag{4.39}$$

The starting values for the secondary radius r_O and the angle φ are set according to [45,

p. 48] for the case $i_r = 1.0$:

$$r_{O_S} = \left(0.5\tilde{l}_R - \sqrt{d_A^2 + d_{align}^2}\right)/\pi, \tag{4.40}$$

$$\varphi_S = \pi/2. \tag{4.41}$$

The starting value for v_0 is chosen according to (4.33). Equation (4.39) combined with the two kinetic equations for the clamping forces (4.19) and (4.31) have the unknowns r_O, φ and v_0.

4.1.4 Classification of all boundary conditions

With the help of the derived equations of this subsection, the initial velocity can be gained for all six variable CVT boundary settings by means of a nonlinear system solver. The required equations are shown in Table 4.2.

Table 4.2: Classification of CVT boundary settings to formulas

	ω_I, M_O	ω_I, ω_O
$\dot{z}_{C_I}$, F_{C_O}	substitute (4.20) solve (4.19)	solve (4.19)
F_{C_I}, $\dot{z}_{C_O}$	substitute (4.20) solve (4.31)	solve (4.31)
F_{C_I}, F_{C_O}	substitute (4.20) solve (4.39), (4.19), (4.31)	solve (4.39), (4.19), (4.31)

The corresponding starting values for the calculation of v_0 with the Newton solver are explained in the respective sections. In the cases where both angular velocities are given, the initial geometric transmission ratio is calculated from the speed ratio $i_s = \omega_I/\omega_O$ and has not to be specified separately. To guarantee a robust initialisation process, the starting value v_{0_S} is directly used for v_0 if the Newton solver does not converge. The final belt velocity can be calculated from v_0 with the formula from [45]:

$$v = \left[1 + \frac{L}{EA}\right] v_0. \tag{4.42}$$

4.2 Tapered elements

The thickness t of the elements is not constant over the height resulting from the manufacturing process. In fact the elements have shaped contact zones or are tapered, i.e. the element front and rear planes are not perfectly parallel. On the one hand, to reproduce this variability of the production process in the model, and on the other hand to enable an optimisation of the element shape for this process, a new variable t_R - the width at the rocking edge - was introduced in addition to the existing width t_T at the top, see Figure 4.3. This study is restricted to the case $t_T \geq t_R > 0$. The difference between both thicknesses is in the magnitude of micrometres compared to a physical width of $t_R \approx 1.5\,\text{mm}$. The notation 'straight part' in this context is used synonymously for the strand, i.e. the part of the pushbelt between the two pulleys. In a pushbelt CVT there are two different straight parts, the loose and the push part. Unlike the word indicates, the run in the straight parts does not have to be straight but can be curved, depending on the dynamical behaviour of the pushbelt.

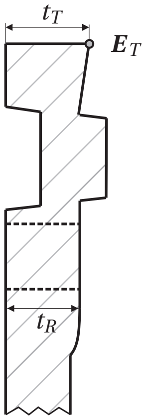

Figure 4.3: Modelling top width t_T differently than rocking edge width t_R

As the top contact between two elements is modelled as a point-plane contact, no further changes have to be made for the contact kinematics than to reposition the point $\boldsymbol{E}_T$ depending on t_T. However, the concept of the geometric initialisation of the pushbelt has to be adapted due to the modified element geometry. The arrangement of the elements in the straight parts, formerly defined by the respective (straight) tangent on both circles, is influenced by a larger top width. The elements no longer fit in a straight run. The resulting course is convex, similar to a cat's arched back. This phenomenon is not limited to the initialisation, but is as well formed in the dynamical simulation. Therefore, it is already included in the initialisation process for the tapered case. The course in the circular pulley arcs, in contrast, is not influenced by the tapered elements as the curvature of the circles causes the element top contacts to be open, cf. Figure 4.4 for an extreme transmission ratio.

The course in the straight parts influences the overall dynamics of the system. In addition to the cat's back, the phenomenon of a dog's back - a concave run - in the straight parts exists. It results for the case $t_R \geq t_T > 0$. The running-in in the pulleys from the straight part is smoother with a cat's back arc compared to a dog's back arc. The transmission of forces from element to element is distributed mainly on the rocking edge in both cases, but the force ratio of the top contact increases in the dog's back case

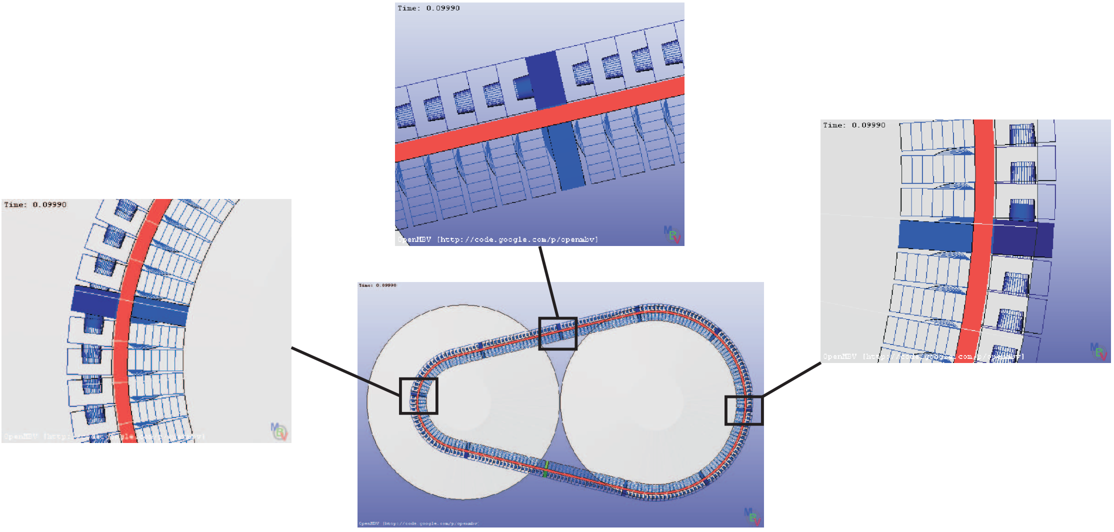

Figure 4.4: Open element-element top contact in arcs and closed contact in straight parts

compared to the cat's back case. Therefore, the effect of the dog's back is not desired and is not treated in this study.

With the changed element geometry the question arises how to describe the curve in the straight parts analytically. For the geometric initialisation it is assumed that all elements in the upper and lower straight part are in contact at the top and rocking edge with the rear plane of the predecessor. Thus, wedges are gained which are placed tightly next to each other. This results in good approximation in a circular course - the cat's back - with a variable radius r_{st} - the cat's back radius - around the midpoint M_{st}, see Figure 4.5*a*. The radius depends on the taperedness t_T. It is the smaller, the greater the taperedness is. This cat's back radius is derived in the following in the element coordinate system. As the in-plane (x, y) and out-of-plane (z) coordinates are decoupled in the geometric initialisation, only the planar description is shown in the first parts of this section. In a second step, the belt deflection (z variable) is added.

4.2.1 Geometric calculation

The curve of the neutral fibre of the ring sets is the reference line for the initialisation process in the spatial model. The ring sets are then initialised around this curve and the elements adapt to the ring sets. The pulley position does not change by the tapered elements. Therefore, it suffices to describe the curve of the ring sets and utilise the same algorithm for the elements and pulleys as in [45]. The relevant quantities for the initialisation are derived in the following.

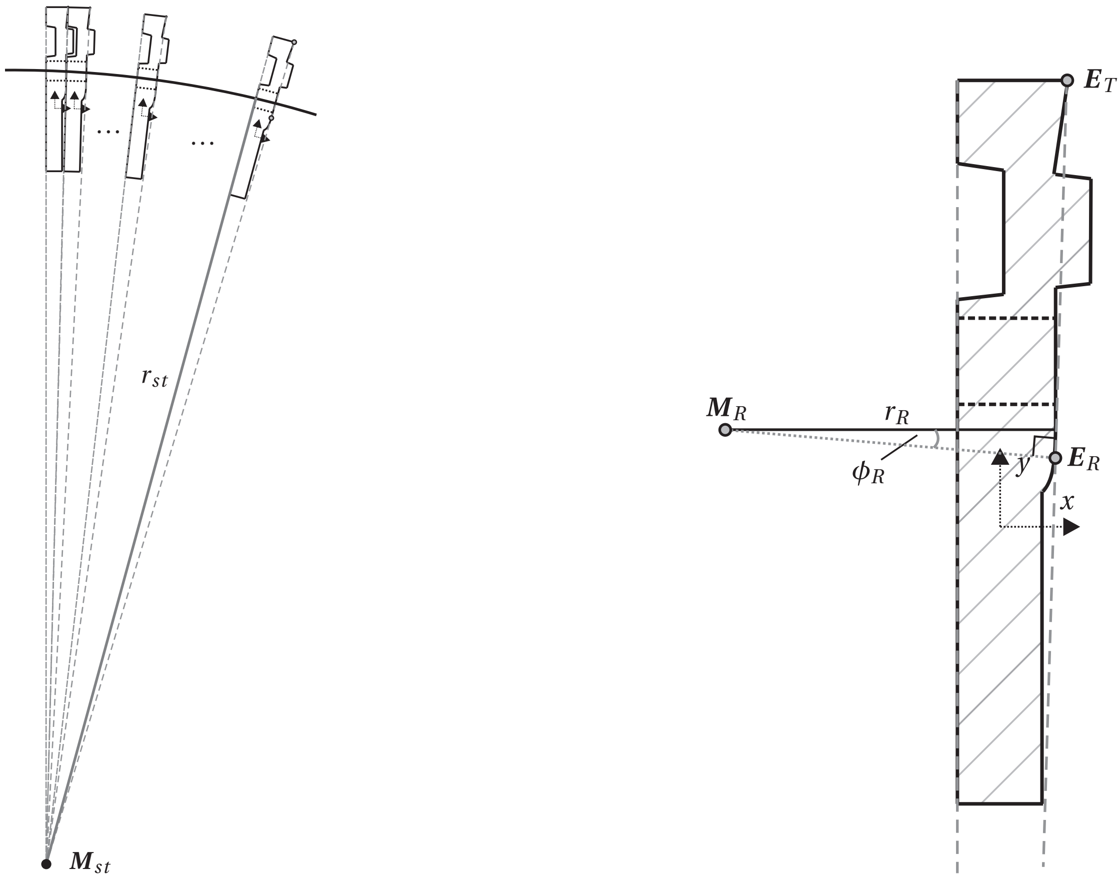

(a) Tapered elements together (b) Tangent on rocking edge circle

Figure 4.5: Taperedness approximated with circle in straight part

Calculation of the cat's back radius

The cat's back arc describes the initial position of the neutral fibre of the ring set which runs through the elements between saddle and pillar, see Figure 4.5*a*. Then, the elements are placed perpendicular on the ring set.

In this subsection all vectors are given in the element reference coordinate system E situated in the element centre of gravity (see Figure 4.6). Therefore, the notation ${}_E(\cdot)$ is neglected. The deflection coordinate is added later. The element top points at rear and front are

$$\boldsymbol{R}_T = \begin{pmatrix} -t_S \\ h_T - h_S \end{pmatrix}, \qquad \boldsymbol{E}_T = \begin{pmatrix} t_T - t_S \\ h_T - h_S \end{pmatrix}, \tag{4.43}$$

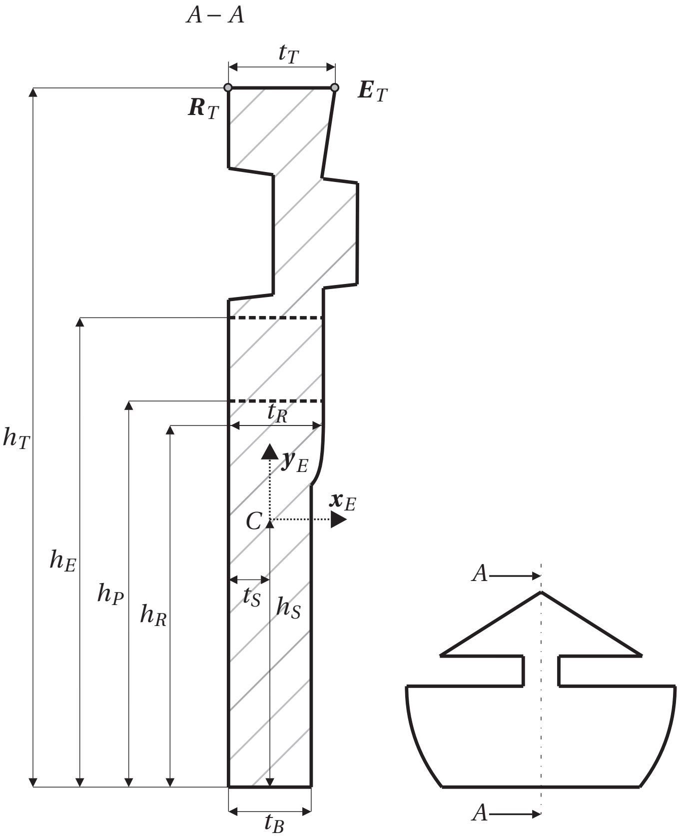

Figure 4.6: Element - side view [45, p. 16]

and the midpoint of the rocking edge arc is (cf. Figure 4.5*b*)

$$\boldsymbol{M}_R = \begin{pmatrix} t_R - t_S \\ h_R - h_S \end{pmatrix} - \begin{pmatrix} r_R \\ 0 \end{pmatrix}. \tag{4.44}$$

At the rocking edge the elements are in contact with the rear plane of the predecessor at two circular arcs (left and right). This circle-plane contact enables rolling up, i.e. the contact point moves along the circle in one direction. With the assumption that all elements in the straight parts are in contact at the top and rocking edge, the contact point on the rocking edge has to be found. This point $\boldsymbol{E}_R$ is obtained by the tangent on the rocking edge arc through the point $\boldsymbol{E}_T$ which is shown in Figure 4.5*b*. As the initialisation is done symmetrically around the x-y-plane, one circular arc around the midpoint $\boldsymbol{M}_R$ in the x-y-plane is used. As $\boldsymbol{E}_R$ lies on the circle it can be expressed depending on the angle ϕ_R with $r_R \neq 0$

$$\boldsymbol{E}_R(\phi_R) = \boldsymbol{M}_R + r_R \begin{pmatrix} \cos\phi_R \\ \sin\phi_R \end{pmatrix}. \tag{4.45}$$

This angle can be calculated by a nonlinear equation using the fact that both the normal and the tangent on the circle through $\boldsymbol{E}_R$ depend on ϕ_R and are orthogonal. An outward pointing normal in point $\boldsymbol{E}_R$ on the circle satisfies

$$\boldsymbol{E}_R - \boldsymbol{M}_R = r_R \begin{pmatrix} \cos\phi_R \\ \sin\phi_R \end{pmatrix}, \tag{4.46}$$

and a tangent can be expressed with $\boldsymbol{E}_R - \boldsymbol{E}_T$. The angle ϕ_R can now be obtained under the condition that tangent and normal in $\boldsymbol{E}_R$ have to be orthogonal

$$(\boldsymbol{E}_R - \boldsymbol{E}_T) \cdot (\boldsymbol{E}_R - \boldsymbol{M}_R) = 0. \tag{4.47}$$

Inserting the definition of $\boldsymbol{E}_R$ yields

$$r_R \left((\boldsymbol{M}_R - \boldsymbol{E}_T) \cdot \begin{pmatrix} \cos\phi_R \\ \sin\phi_R \end{pmatrix} + r_R \right) = 0. \tag{4.48}$$

This leads to the nonlinear system in ϕ_R

$$f(\phi_R) = a_1 \cos\phi_R + a_2 \sin\phi_R + r_R = 0, \tag{4.49}$$

with the abbreviation

$$\begin{pmatrix} a_1 \\ a_2 \end{pmatrix} := \boldsymbol{M}_R - \boldsymbol{E}_T = \begin{pmatrix} t_R - r_R - t_T \\ h_R - h_T \end{pmatrix}.$$

The system (4.49) is solved by the Newton method with the starting value $\phi_{R,0} = 0$ from the case $t_T = t_R$. The derivative for the Newton method is given by

$$f'(\phi_R) = -a_1 \sin\phi_R + a_2 \cos\phi_R. \tag{4.50}$$

With the resulting angle ϕ_R, the point $\boldsymbol{E}_R$ can be calculated by (4.45).

The next step is to find the intersection of the two straight lines, $\overline{\boldsymbol{E}_T\boldsymbol{E}_R}$ and the rear line of the element, as illustrated in Figure 4.5*b*. The straight line equations are given by

$$g_1 : \boldsymbol{r}_1 = \boldsymbol{E}_T + \lambda_1 (\boldsymbol{E}_R - \boldsymbol{E}_T), \tag{4.51}$$

$$g_2 : \boldsymbol{r}_2 = \boldsymbol{R}_T + \lambda_2 \begin{pmatrix} 0 \\ -1 \end{pmatrix}. \tag{4.52}$$

As the vertical (yaw) axis is parallel to the rear line [45], the rear line is expressed through the top point $\boldsymbol{R}_T$ and the vector in negative y direction to simplify the resulting linear system. The intersection of both straight lines $g_1 \cap g_2$ yields the midpoint of the cat's back circle in the element reference system. Both equations (4.51) and (4.52) are identified which leads to a linear system with the two unknowns λ_1 and λ_2:

$$\begin{pmatrix} \boldsymbol{E}_R - \boldsymbol{E}_T & \begin{pmatrix} 0 \\ 1 \end{pmatrix} \end{pmatrix} \begin{pmatrix} \lambda_1 \\ \lambda_2 \end{pmatrix} = \boldsymbol{R}_T - \boldsymbol{E}_T, \tag{4.53}$$

$$\begin{pmatrix} t_R - t_T + r_R(\cos\phi_R - 1) & 0 \\ h_R - h_T + r_R \sin\phi_R & 1 \end{pmatrix} \begin{pmatrix} \lambda_1 \\ \lambda_2 \end{pmatrix} = \begin{pmatrix} -t_T \\ 0 \end{pmatrix}. \tag{4.54}$$

The linear system can be solved analytically to

$$\lambda_1 = \frac{-t_T}{t_R - t_T + r_R(\cos\phi_R - 1)}, \tag{4.55}$$

$$\lambda_2 = -(h_R - h_T + r_R \sin\phi_R)\,\lambda_1 = \frac{(h_R - h_T + r_R \sin\phi_R)\; t_T}{t_R - t_T + r_R(\cos\phi_R - 1)}. \tag{4.56}$$

The absolute value of λ_2 is the distance between $\boldsymbol{R}_T$ and the midpoint expressed on the rear line of the element, according to the construction of the straight line equation (4.52). To obtain the radius r_{st} out of $|\lambda_2|$, the distance between $\boldsymbol{R}_T$ and the level of the neutral fibre of the ring set has to be subtracted

$$r_{st} = |\lambda_2| - h_T + h_P + \frac{1}{2}\tilde{h}_r, \tag{4.57}$$

with h_P describing the height of the element pillar (cf. Figure 4.6) where the ring set is situated and $\tilde{h}_r$ the height of the ring set. Thereby, it is assumed that the ring sets are in contact with the elements on the saddle.

Now the question arises how to calculate the midpoint of the circular arc with the obtained radius r_{st}. This subject is dealt with in the next subsection.

Calculation of midpoint of the cat's back arc

The circular arc is put through the former tangent points $\boldsymbol{T}_O$ and $\boldsymbol{T}_I$, cf. Figure 4.7. This is legitimate as the modelling set up should converge for $t_T \rightarrow t_R$ in the straight part of the non-tapered case with the resulting cat's back radius going to infinity. The vectors in this subsection are all expressed in the inertial coordinate system (situated in the centre of the secondary pulley), therefore the addition ${}_I(\cdot)$ has been neglected. The two transition points from secondary and primary pulley to the upper straight part are

$$\boldsymbol{T}_O = r_O \begin{pmatrix} -\cos\varphi \\ \sin\varphi \end{pmatrix}, \qquad \boldsymbol{T}_I = \begin{pmatrix} d_A \\ 0 \end{pmatrix} + r_I \begin{pmatrix} -\cos\varphi \\ \sin\varphi \end{pmatrix}$$

with the angle φ. The midpoint of the straight connection from $\boldsymbol{T}_O$ to $\boldsymbol{T}_I$ satisfies

$$\boldsymbol{t}_m = \frac{1}{2}(\boldsymbol{T}_O - \boldsymbol{T}_I), \tag{4.58}$$

and the length of the straight part in the plane (without the misalignment) is

$$t_L = \sin(\varphi) d_A, \tag{4.59}$$

cf. Figure 4.7. Together with the radius r_{st} calculated in the previous subsection and the theorem of Pythagoras the distance d_m from the upper straight part midpoint

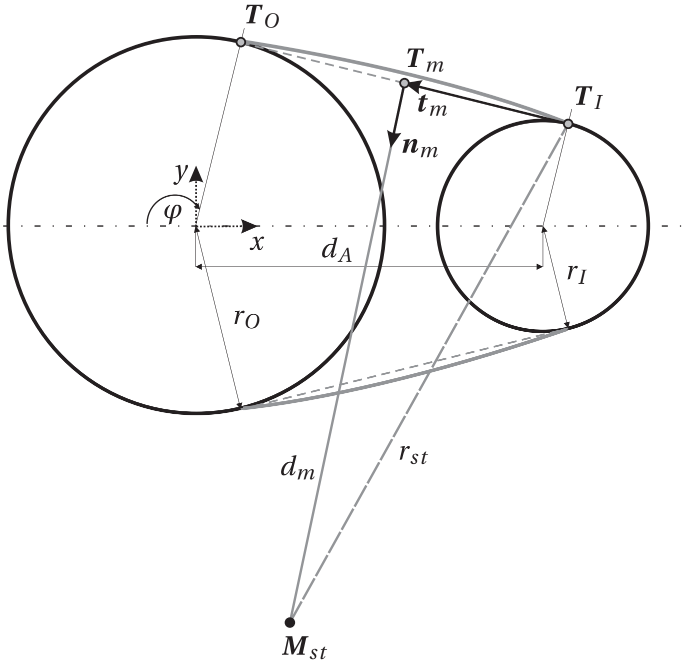

Figure 4.7: Identifying the midpoint $\boldsymbol{M}_{st}$ of upper circular arc

$$\boldsymbol{T}_m = \frac{1}{2}(\boldsymbol{T}_O + \boldsymbol{T}_I) \tag{4.60}$$

to the midpoint of the arc $\boldsymbol{M}_{st}$ can be calculated

$$d_m = \sqrt{r_{st}^2 - (t_L/2)^2}. \tag{4.61}$$

Finally, only the direction from $\boldsymbol{T}_m$ to $\boldsymbol{M}_{st}$ is missing. The normalised normal from $\boldsymbol{T}_m$ to $\boldsymbol{M}_{st}$ can easily be found as the orthogonal complement of $\boldsymbol{t}_m$

$$\boldsymbol{n}_m = \frac{2}{t_L}\begin{pmatrix} -\boldsymbol{t}_m(2) \\ \boldsymbol{t}_m(1) \end{pmatrix}. \tag{4.62}$$

Altogether, the midpoint of the upper cat's back arc satisfies

$$\boldsymbol{M}_{st} := \boldsymbol{M}_{st,u} = \boldsymbol{T}_m + d_m \boldsymbol{n}_m. \tag{4.63}$$

The midpoint of the lower arc can be gained directly from the upper one for reasons of symmetry

$$\boldsymbol{M}_{st,l} = \begin{pmatrix} \boldsymbol{M}_{st}(1) \\ -\boldsymbol{M}_{st}(2) \end{pmatrix}. \tag{4.64}$$

The overall curve with all in all four circular arcs is C^0 continuous and takes into account the taperedness of the elements. However, at the transitions of two neighbouring arcs a kink is located. The curve for the geometric initialisation of the pushbelt should at least be as smooth as in the non-tapered case, i.e. C^1 continuous. Then, also a smooth running-in in the pulley arcs can be guaranteed in the starting phase.

Calculation of smooth transitions

In order to get smooth transitions between two circular arcs, two different concepts have been worked out. The first approach is to use a clothoid (Euler spiral) which connects the two circular arcs with a curve starting from the curvature of the first arc (e.g. $1/r_{st}$) and increasing or decreasing linearly to the curvature of the second arc (e.g. $1/r_I$). Hence, the clothoid connection guarantees per definition the equality of the second derivative (curvature) of the curve at each point. For the special geometric constellation of the pushbelt CVT where start and endpoint of the curve are fixed, this approach is not feasible as the clothoid has too few parameters to secure additionally the equality of the first derivative in both transitions. Only C^0 continuity could be achieved with the clothoid concept.

The second solution strategy connects two arcs around a transition point with one tangent to both of them. Thereby, a C^1 curve with circle-straight line-circle transitions results. This concept has been implemented for the initialisation of the pushbelt CVT model and is explained below. The geometric task is to find the tangent on two intersecting circles next to the specified intersection, see Figure 4.8. This can be restated in finding the two tangential points $\boldsymbol{T}_1$ and $\boldsymbol{T}_2$ of the tangent line on the circles. These two points can be expressed by the corresponding midpoint $\boldsymbol{M}_i$, a radius r_i and an angle γ_i, $i = 1{,}2$:

$$\boldsymbol{T}_1 = \boldsymbol{M}_1 + r_1 \begin{pmatrix} \cos\gamma_1 \\ \sin\gamma_1 \end{pmatrix},$$

$$\boldsymbol{T}_2 = \boldsymbol{M}_2 + r_2 \begin{pmatrix} \cos\gamma_2 \\ \sin\gamma_2 \end{pmatrix}.$$

Connecting both intersection points with their respective midpoints $\boldsymbol{M}_1$ and $\boldsymbol{M}_2$, these two lines are parallel as they are both at a right angle with the tangent, cf. Figure 4.8. Then, considering the straight line connecting both midpoints, it follows from the Euclidean parallelism that the angles are equal. Therefore, also the two parameterising

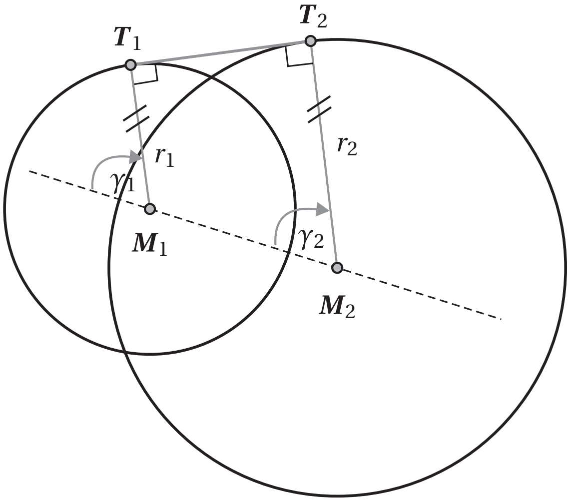

Figure 4.8: Tangent on two intersecting circles

angles are equal

$$\gamma := \gamma_1 = \gamma_2.$$

This angle γ has to be calculated which is shown using the example of the secondary pulley, illustrated in Figure 4.9. The two points in this case are the tangential points at the secondary pulley $\boldsymbol{T}_{Ot}$ and at the straight part $\boldsymbol{T}_{Ot,st}$. The vector between the

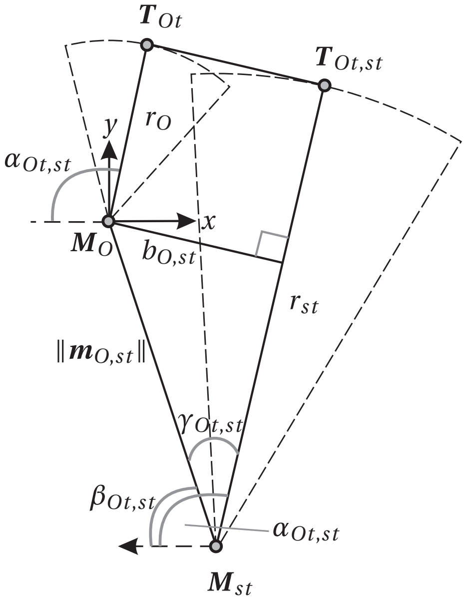

Figure 4.9: Angles for a tangent transition between two intersecting circles

midpoints $\boldsymbol{M}_{st}$ and $\boldsymbol{M}_O$ is denoted with

$$\boldsymbol{m}_{O,st} := \boldsymbol{M}_{st} - \boldsymbol{M}_O.$$

The distance between $\boldsymbol{M}_O$ and the line $[\boldsymbol{M}_{st}, \boldsymbol{T}_{Ot,st}]$ is calculated by the theorem of Pythagoras to

$$b_{O,st} = \sqrt{\|\boldsymbol{m}_{O,st}\|^2 - (r_{st} - r_O)^2}. \tag{4.65}$$

This is also the distance between the two tangent intersection points, which is required to calculate the entire arc length of the initialisation curve. The angle $\gamma_{Ot,st}$ can be derived from the right angle triangle which results through this perpendicular projection

$$\gamma_{Ot,st} = \arccos\left(\frac{r_{st} - r_O}{\|\boldsymbol{m}_{O,st}\|}\right). \tag{4.66}$$

For the initialisation explained in Subsection 4.2.2, the angle to the x-axis has to be specified, too, which is obtained by the dot product between $\boldsymbol{m}_{O,st}$ and the first unit vector $\boldsymbol{e}_1$ representing the x-axis

$$\beta_{Ot,st} = \arccos\left(\frac{\left|\boldsymbol{e}_1^T \boldsymbol{m}_{O,st}\right|}{\|\boldsymbol{e}_1\|_2 \cdot \left\|\boldsymbol{m}_{O,st}\right\|_2}\right) = \arccos\left(\frac{\left|\boldsymbol{m}_{O,st}(1)\right|}{\left\|\boldsymbol{m}_{O,st}\right\|_2}\right). \tag{4.67}$$

Depending on the geometric transmission ratio, two cases have to be distinguished because of the definition of the angle via the dot product.

$$\alpha_{Ot,st} = \begin{cases} \beta_{Ot,st} + \gamma_{Ot,st}, & \text{for } \boldsymbol{M}_{st}(1) \geq \boldsymbol{M}_O(1), \\ (\pi - \beta_{Ot,st}) + \gamma_{Ot,st}, & \text{for } \boldsymbol{M}_{st}(1) < \boldsymbol{M}_O(1). \end{cases} \tag{4.68}$$

Analogously, for the primary pulley the values can be calculated to

$$\boldsymbol{m}_{I,st} = \boldsymbol{M}_{st} - \boldsymbol{M}_I \tag{4.69}$$

$$b_{st,I} = \sqrt{\|\boldsymbol{m}_{I,st}\|^2 - (r_{st} - r_I)^2} \tag{4.70}$$

$$\gamma_{st,It} = \arccos\left(\frac{r_{st} - r_I}{\|\boldsymbol{m}_{I,st}\|}\right) \tag{4.71}$$

$$\beta_{st,It} = \arccos\left(\frac{\left|\boldsymbol{e}_1^T \boldsymbol{m}_{I,st}\right|}{\|\boldsymbol{e}_1\|_2 \cdot \left\|\boldsymbol{m}_{I,st}\right\|_2}\right) = \arccos\left(\frac{\left|\boldsymbol{m}_{I,st}(1)\right|}{\left\|\boldsymbol{m}_{I,st}\right\|_2}\right) \tag{4.72}$$

$$\alpha_{st,It} = \begin{cases} \beta_{st,It} - \gamma_{st,It}, & \text{for } \boldsymbol{M}_{st}(1) \geq \boldsymbol{M}_I(1) \\ (\pi - \beta_{st,It}) - \gamma_{st,It}, & \text{for } \boldsymbol{M}_{st}(1) < \boldsymbol{M}_I(1). \end{cases} \tag{4.73}$$

No further cases can occur as $\boldsymbol{M}_{st}$ is always situated within the two parallels $\overline{\boldsymbol{M}_O\boldsymbol{T}_O}$ and

$\overline{\boldsymbol{M}_I\boldsymbol{T}_I}$. Altogether, the overall geometric initialisation for the pushbelt CVT considering tapered elements is illustrated in Figure 4.10.

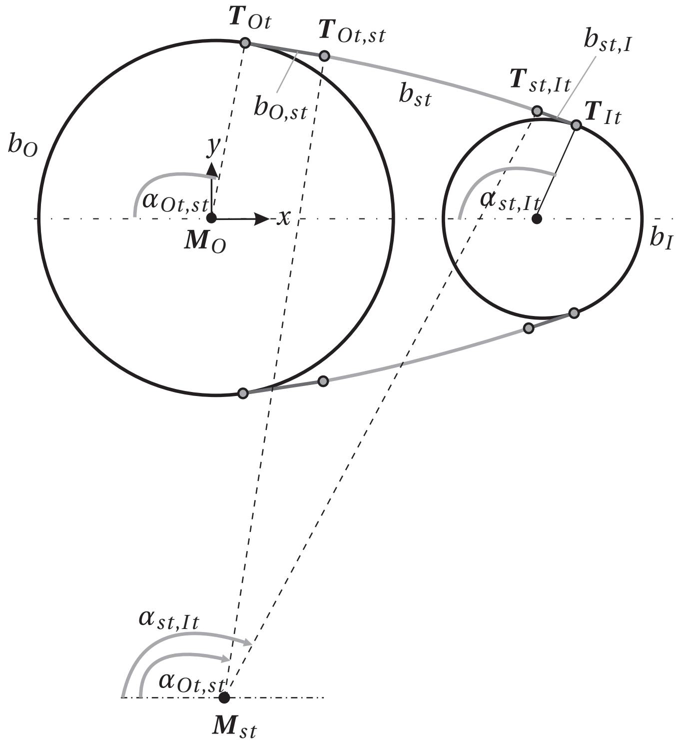

Figure 4.10: Overall geometric initialisation for pushbelt CVT with tapered elements

The overall planar initialisation curve for the neutral fibre of the ring set is known. Because of the discretisation with $\tilde{N}_B$ finite elements, this information is passed to the neutral fibre in the initialisation only at discrete specific points. To represent the tapered curve a minimum number of finite elements is required so that at least one knot is situated in each curve section. These discrete points are interpolated by a smooth curve. This process is shown in Figure 4.11, where for one exemplary setting the planar curve is interpolated with a closed cubic spline. The discrete points are displayed and the tangent transition points are plotted to see each curve section. This shows that a number of 12 finite elements (FE) do not represent the tapered curve sufficiently, as not in every tangent transition one FE knot is located.

Adding the belt deflection

Resulting from different transmission ratios the CVT has to operate in, the belt runs not only in the plane of motion but is deflected according to the misalignment of the pulleys. The belt deflection in z-direction is assumed to be decoupled in the initialisation. Therefore, it is added to the planar curve of the neutral fibre derived before. For the

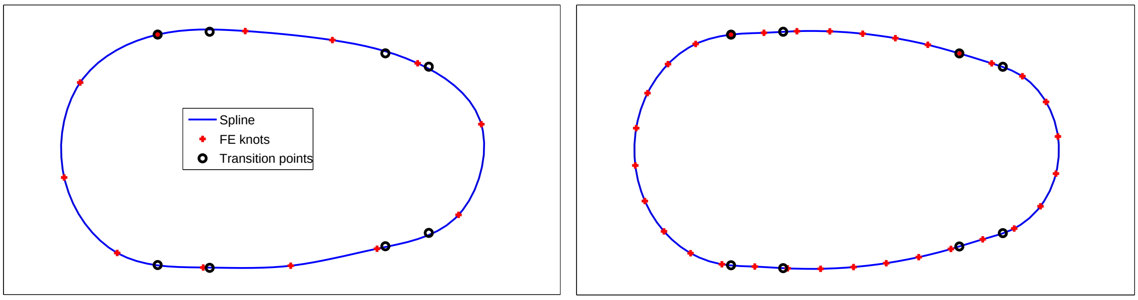

Figure 4.11: Discretisation of a tapered curve with 12 and 32 knots and interpolation with cubic splines

calculation of the belt deflection, the transition points between pulley and push or loose part are of interest. These points are shifted in the case of the tapered elements compared to the non-tapered case. The new transition points between pulleys and upper straight part are $\boldsymbol{T}_{Ot}$ and $\boldsymbol{T}_{It}$ (cf. Figure 4.12), as the curve starts to differ at these points from the circuit paths of the pulleys.

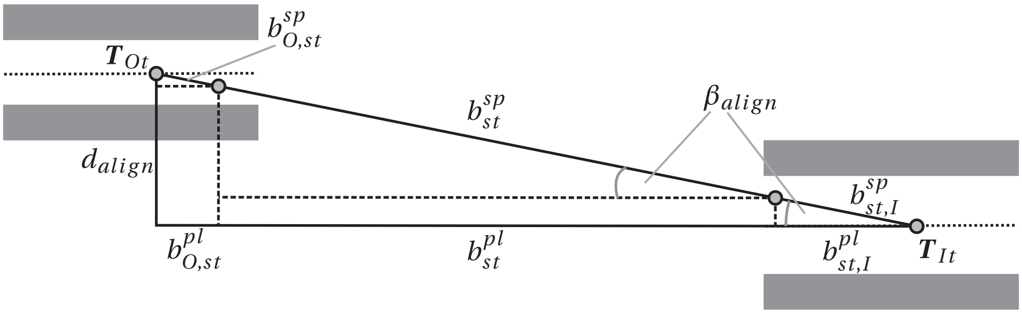

Figure 4.12: Adding the belt deflection

In the pulleys the z-coordinate is constant, i.e. $q_{0_{O_M}}$ for the secondary and $q_{0_{I_M}}$ for the primary pulley. In the straight parts (including tangent transition, cat's back arc, tangent transition) these values are connected linearly, e.g. for the upper part, the mean z position of the ring set satisfies

$$z(s) = \left(1 - \frac{s}{b_{O,st} + b_{st} + b_{st,I}}\right) q_{0_{O_M}} + \frac{s}{b_{O,st} + b_{st} + b_{st,I}} q_{0_{I_M}}, \tag{4.74}$$

for $s \in [0, b_{O,st} + b_{st} + b_{st,I}]$. The variable b_{st} denotes the length of the remaining cat's back arc between the two tangents. For the left resp. right ring set only $\frac{w_S + w_P}{4}$ has to be added resp. subtracted, cf. [45, p. 58].

The misalignment has to also be considered in the arc length of the sections between the pulleys. The alignment angle for the tapered case is (cf. Figure 4.12)

$$\beta_{align} = \left| \arctan\left(\frac{d_{align}}{|\boldsymbol{T}_{It}(1) - \boldsymbol{T}_{Ot}(1)|} \right) \right| . \tag{4.75}$$

Thereby, the adaption of the arc length is done for the three segments $b_{O,st}, b_{st}$ and $b_{st,I}$ with a stretching factor. As the initialisation is based on the planar model [44] the spatial (sp) arc lengths are gained from the planar (pl) ones with

$$b_*^{sp} = \frac{b_*^{pl}}{cos(\beta_{align})} . \tag{4.76}$$

The calculation with the stretching factor is valid under the assumption that the curvature is close to zero which corresponds to a straight line because of the small taperedness of the elements.

The curve is parametrised by the arc length with ring set length $\tilde{l}_r$. This is the length of the neutral fibre of the ring set in the relaxed state. The different sections added up for the tapered case are slightly longer than the relaxed length

$$2b_{O,st} + 2b_{st} + 2b_{st,I} + b_I + b_O > \tilde{l}_r, \tag{4.77}$$

that means a prestressing of the belt is indirectly introduced with this approach. However, this prestressing is not based on kinetic assumptions, e.g. the force equilibrium.

4.2.2 Initialisation

For the initialisation of the spatial RCM beam, the DOFs of the individual finite elements representing the neutral fibre of the beam have to be set:

$$\boldsymbol{q}_{g_e} = \left(\ldots, x_i, y_i, z_i, \alpha_i, \beta_i, \gamma_i, c_{i,L_1}, c_{i,R_1}, c_{i,L_2}, c_{i,R_2}, x_{i+1}, \ldots\right). \tag{4.78}$$

Note that there are two ring sets which differ only in the z-coordinate as the initialisation is done symmetrically. This can be seen by the plus-minus sign in the formulas for the z-coordinate. Each finite element has ten DOFs, six rigid and four flexible ones. In the first part the six rigid DOFs are shown starting from the secondary pulley at $\boldsymbol{T}_{Ot}$ going anticlockwise over $\boldsymbol{T}_{Ot,st}$. For simplification the following arc length sections are introduced

$$\begin{aligned} s_{1,Ot,st} &= b_{O,st}, \\ s_{2,st,It} &= b_{O,st} + b_{st}, \\ s_{3,It} &= b_{O,st} + b_{st} + b_{st,I}, \\ s_{4,Ib} &= b_{O,st} + b_{st} + b_{st,I} + b_I, \end{aligned} \tag{4.79}$$

which are the sections that have to be distinguished for the initialisation process. For background information on the initialisation process of the spatial RCM beam see [45, p. 19 ff.]. The DOFs are set node per node, therefore all nodes $i = 0, \dots, \tilde{N}_B - 1$ are gone through with a constant length for each FE of $l_0 = \tilde{l}_R / \tilde{N}_B$. As an example, the upper part is demonstrated in the following.

Rigid coordinates

The two rotational directions are decoupled for $|d_{align}| \ll |d_A|$, see [45]. The current node location is denoted by $s = i l_0$. Node per node, the current node location is compared to the arc lengths of the different sections (4.79) to determine where it is situated. The position is described by the three coordinates x_i, y_i, z_i and the rotation by the Cardan angles $\alpha_i, \beta_i, \gamma_i$ with reversed rotation sequence $(z - y - x)$.

$0 \le i l_0 < s_{1,Ot,st}$ - **first tangent** between secondary top and upper cat's back:

$$\begin{pmatrix} x_i \\ y_i \end{pmatrix} = \boldsymbol{T}_{Ot} + \frac{i l_0}{s_{1,Ot,st}} (\boldsymbol{T}_{Ot,st} - \boldsymbol{T}_{Ot}), \tag{4.80}$$

$$z_i = \left(1 - \frac{i l_0}{s_{3,It}}\right) q_{0_{O_M}} + \frac{i l_0}{s_{3,It}} q_{0_{I_M}} \pm \frac{w_S + w_P}{4}, \tag{4.81}$$

$$\alpha_i = 0, \tag{4.82}$$

$$\beta_i = \arctan\left(\frac{q_{0_{O_M}} - q_{0_{I_M}}}{\sin(\varphi) d_A}\right), \tag{4.83}$$

$$\gamma_i = 0.5\pi - \alpha_{Ot,st}. \tag{4.84}$$

$s_{1,Ot,st} \le i l_0 < s_{2,st,It}$ - **upper cat's back** with $\alpha_{up} = \frac{i l_0 - s_{1,Ot,st}}{r_{st}}$:

$$\begin{pmatrix} x_i \\ y_i \end{pmatrix} = \boldsymbol{M}_{st} + r_{st} \begin{pmatrix} -\cos(\alpha_{Ot,st} + \alpha_{up}) \\ \sin(\alpha_{Ot,st} + \alpha_{up}) \end{pmatrix}, \tag{4.85}$$

$$z_i = \left(1 - \frac{i l_0 - s_{1,Ot,st}}{s_{3,It}}\right) q_{0_{O_M}} + \frac{i l_0 - s_{1,Ot,st}}{s_{3,It}} q_{0_{I_M}} \pm \frac{w_S + w_P}{4}, \tag{4.86}$$

$$\alpha_i = 0, \tag{4.87}$$

$$\beta_i = \arctan\left(\frac{q_{0_{O_M}} - q_{0_{I_M}}}{\sin(\varphi) d_A}\right), \tag{4.88}$$

$$\gamma_i = 0.5\pi - \alpha_{Ot,st} - \alpha_{up}. \tag{4.89}$$

$s_{2,st,It} \le i l_0 < s_{3,It}$ - **second tangent** between upper cat's back and primary top:

$$\begin{pmatrix} x_i \\ y_i \end{pmatrix} = \boldsymbol{T}_{st,It} + \frac{i l_0 - s_{2,st,It}}{b_{st,I}} (\boldsymbol{T}_{It} - \boldsymbol{T}_{st,It}), \tag{4.90}$$

$$z_i = \left(1 - \frac{i l_0 - s_{2,st,It}}{s_{3,It}}\right) q_{0_{O_M}} + \frac{i l_0 - s_{2,st,It}}{s_{3,It}} q_{0_{I_M}} \pm \frac{w_S + w_P}{4}, \tag{4.91}$$

$$\alpha_i = 0, \tag{4.92}$$

$$\beta_i = \arctan\left(\frac{q_{0_{O_M}} - q_{0_{I_M}}}{\sin(\varphi) d_A}\right), \tag{4.93}$$

$$\gamma_i = 0.5\pi - \alpha_{st,It}. \tag{4.94}$$

$s_{3,It} \leq i l_0 < s_{4,Ib}$ - **primary arc** with $\alpha_I = \frac{i l_0 - s_{3,It}}{r_I}$:

$$\begin{pmatrix} x_i \\ y_i \end{pmatrix} = \boldsymbol{M}_I + r_I \begin{pmatrix} -\cos(\alpha_{st,It} + \alpha_I) \\ \sin(\alpha_{st,It} + \alpha_I) \end{pmatrix}, \tag{4.95}$$

$$z_i = q_{0_{I_M}} \pm \frac{w_S + w_P}{4}, \tag{4.96}$$

$$\alpha_i = 0, \tag{4.97}$$

$$\beta_i = 0, \tag{4.98}$$

$$\gamma_i = 0.5\pi - \alpha_{st,It} - \alpha_I. \tag{4.99}$$

The second half from $s_{4,Ib}$ to the end is done analogously.

Deflection coordinates

Again, both directions are decoupled as $|d_{align}| \ll |d_A|$. One finite element with arc length l_0 is divided into four equal sections

$$0 < \frac{l_0}{4} < \frac{l_0}{2} < \frac{3 l_0}{4} < l_0. \tag{4.100}$$

The flexible or deflection coordinates model the relative beam deflection measured from the points on the neutral fibre at $l_0/4$ resp. $3l_0/4$ to the tangent on the midpoint of each finite element which correlates to c_{L_*} resp. c_{R_*} (cf. e.g. Figure 4.13). They are constant (but in general unequal to zero) within each curve section. The deflections of the out-of-plane motion are denoted with 1 (c_{L_1}, c_{R_1}) and the ones of the in-plane motion with 2 (c_{L_2}, c_{R_2}). In the chosen approach with the smooth transitions, only straight line - circular arc - straight line transitions occur in the plane of motion and straight line - straight line transitions in the out-of-plane motion. This is similar to the non-tapered case, and therefore the calculation can be done analytically and follows [45, p. 58 ff].

If a finite element is situated completely inside one geometric element (straight line resp. circular arc), the flexible coordinates can easily be calculated from the deflection of this geometric element. This is shown as an example for one finite element which is completely inside a circular arc in Figure 4.13. The deflection c_{R_2} is the distance of the projection of the point at $3l_0/4$ to the tangent on the midpoint. This yields

$$\psi = \frac{l_0/4}{r_I}, \tag{4.101}$$

$$c_{R_2} = -(r_I - \cos(\psi) r_I), \tag{4.102}$$

as the bending is in negative direction. Otherwise, if a finite element is situated between two geometric elements, a combination of the deflection of these has to be applied. This more complicated case is dealt with below.

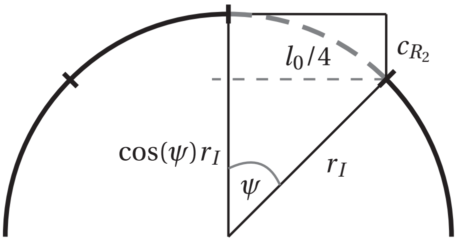

Figure 4.13: Deflection of one finite element in a circular arc

In the initialisation process with tapered elements, only two cases are possible for the in-plane deflections. They are the transition from a straight line to a circular arc and vice versa from a circular arc to a straight line. The first case describes the run-out of the straight line which equals the running-in in the circular arc. The second case includes the run-out of the circular arc, which is the running-in in the straight line. Regarding the out-of-plane deflections (in the x-z-plane), only the transition points between straight parts and pulleys are of interest cf. Figure 4.12. In each pulley, the course (restricted to the x-z-plane) is straight and parallel to the x-axis. Both straight lines have different z-coordinates and are connected linearly with two identical straight lines for the course in the straight parts.

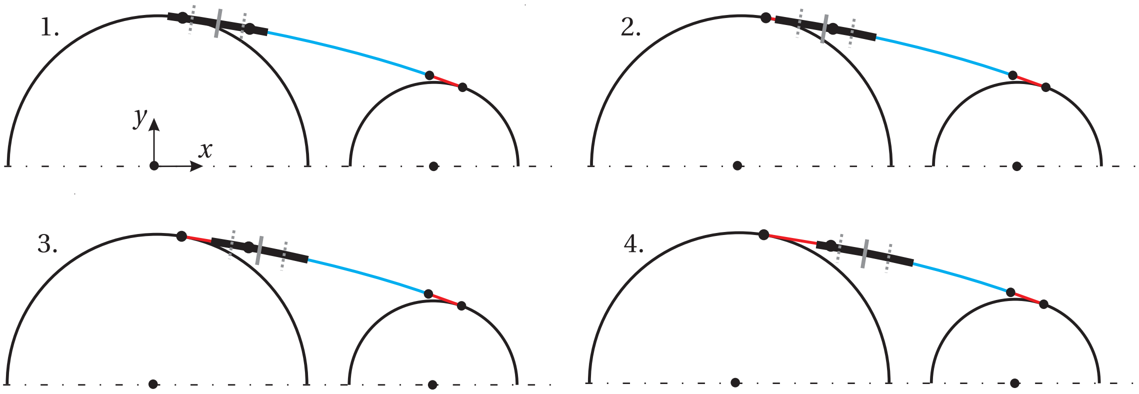

Figure 4.14: Four cases of in-plane deflection for running-in in cat's back arc

For the calculation of the flexible DOFs, the ratio at which the transition point divides the finite element has to be distinguished. Each finite element ($0 < s < l_0$) is divided into four parts with a length of $l_0/4$. The corresponding four possible cases are shown in Figure 4.14 for the transition point at the length $s_{1,Ot,st}$. The cases are classified as how much of the finite element is inside the the upper cat's back arc. These are

1. at most one forth,
2. more than one forth and at most one half,
3. more than one half and at most three forth,
4. at least three forth.

In the cases 2. and 3. the deflections of the straight line and the arc have to be combined. Again the knots of the finite elements are executed step by step with the variable i multiplied by the finite element length. The actual length il_0 is used to initalise the deflection coordinates $c_{i-1,*}$ of the last finite element. How far the end knot il_0 has entered the next section is distinguished by means of the arc length of the individual sections. Hereby, it is assumed that one fourth of the finite element is smaller than the arc length of the tangents $l_0/4 < b_{O,st}, b_{st,I}$.

To show all the different possible transitions, two examples are chosen from which all the other cases can be derived. First, one transition inside the straight part is demonstrated where all c_{i,L_1}, c_{i,R_1} are equal to zero. Considering the in-plane deflection, it shows the case running from a straight part into an arc.

Transition first tangent - upper cat's back arc (running-in in cat's back arc)
$il_0 - s_{1,Ot,st} \leq \frac{l_0}{4}$:

$$c_{i-1,L_1} = 0, \tag{4.103}$$
$$c_{i-1,R_1} = 0, \tag{4.104}$$
$$c_{i-1,L_2} = 0, \tag{4.105}$$
$$c_{i-1,R_2} = 0. \tag{4.106}$$

$\frac{l_0}{4} < il_0 - s_{1,Ot,st} \leq \frac{l_0}{2}$:

$$c_{i-1,L_1} = 0, \tag{4.107}$$
$$c_{i-1,R_1} = 0, \tag{4.108}$$
$$c_{i-1,L_2} = 0, \tag{4.109}$$
$$c_{i-1,R_2} = r_{st}\left(\cos\left(\frac{il_0 - s_{1,Ot,st} - \frac{l_0}{4}}{r_{st}}\right) - 1\right). \tag{4.110}$$

$\frac{l_0}{2} < i\,l_0 - s_{1,Ot,st} \le \frac{3l_0}{4}$:

$$c_{i-1,L_1} = 0, \tag{4.111}$$

$$c_{i-1,R_1} = 0, \tag{4.112}$$

$$\begin{aligned} c_{i-1,L_2} = r_{st}\left(\cos\left(\frac{i\,l_0 - s_{1,Ot,st} - \frac{l_0}{2}}{r_{st}}\right) - 1\right) \\ - \left(\frac{3l_0}{4} - i\,l_0 + s_{1,Ot,st}\right)\sin\left(\frac{i\,l_0 - s_{1,Ot,st} - \frac{l_0}{2}}{r_{st}}\right), \end{aligned} \tag{4.113}$$

$$c_{i-1,R_2} = r_{st}\left(\cos\left(\frac{l_0}{4r_{st}}\right) - 1\right). \tag{4.114}$$

$i\,l_0 - s_{1,Ot,st} \ge \frac{3l_0}{4}$:

$$c_{i-1,L_1} = 0, \tag{4.115}$$

$$c_{i-1,R_1} = 0, \tag{4.116}$$

$$c_{i-1,L_2} = r_{st}\left(\cos\left(\frac{l_0}{4r_{st}}\right) - 1\right), \tag{4.117}$$

$$c_{i-1,R_2} = r_{st}\left(\cos\left(\frac{l_0}{4r_{st}}\right) - 1\right). \tag{4.118}$$

The second example shows the out-of-plane deflections of the transition from pulley to straight part and the run-out of an arc concerning the in-plane deflection.

Transition primary pulley - following tangent (run-out primary arc)

$i\,l_0 - s_{4,Ib} \le \frac{l_0}{4}$:

$$c_{i-1,L_1} = 0, \tag{4.119}$$

$$c_{i-1,R_1} = 0, \tag{4.120}$$

$$c_{i-1,L_2} = r_I\left(\cos\left(\frac{l_0}{4r_I}\right) - 1\right), \tag{4.121}$$

$$c_{i-1,R_2} = r_I\left(\cos\left(\frac{l_0}{4r_I}\right) - 1\right). \tag{4.122}$$

$\frac{l_0}{4} < i\,l_0 - s_{4,Ib} \le \frac{l_0}{2}$:

$$c_{i-1,L_1} = 0, \tag{4.123}$$

$$c_{i-1,R_1} = \sin\left(\arctan\left(\frac{q_{0_{I_M}} - q_{0_{O_M}}}{\sin(\varphi)\,d_A}\right)\right)\left(\frac{l_0}{4} - (i-1)\,l_0 + s_{4,Ib}\right), \tag{4.124}$$

$$c_{i-1,L_2} = r_I\left(\cos\left(\frac{l_0}{4r_I}\right) - 1\right), \tag{4.125}$$

$$\begin{aligned} c_{i-1,R_2} = r_I &\left(\cos\left(\frac{\frac{l_0}{2} - i\,l_0 + s_{4,Ib}}{r_I}\right) - 1\right) \\ &- \left(i\,l_0 - s_{4,Ib} - \frac{l_0}{4}\right)\sin\left(\frac{\frac{l_0}{2} - i\,l_0 + s_{4,Ib}}{r_I}\right). \end{aligned} \tag{4.126}$$

$\frac{l_0}{2} < i\,l_0 - s_{4,Ib} \leq \frac{3l_0}{4}$:

$$c_{i-1,L_1} = \sin\left(\arctan\left(\frac{q_{0_{I_M}} - q_{0_{O_M}}}{\sin(\varphi)\,d_A}\right)\right)\left((i-1)\,l_0 - s_{4,Ib} + \frac{3l_0}{4}\right), \tag{4.127}$$

$$c_{i-1,R_1} = 0, \tag{4.128}$$

$$c_{i-1,L_2} = r_I\left(\cos\left(\frac{\frac{3l_0}{4} - i\,l_0 + s_{4,Ib}}{r_I}\right) - 1\right), \tag{4.129}$$

$$c_{i-1,R_2} = 0. \tag{4.130}$$

$i\,l_0 - s_{4,Ib} \geq \frac{3l_0}{4}$:

$$c_{i-1,L_1} = 0, \tag{4.131}$$

$$c_{i-1,R_1} = 0, \tag{4.132}$$

$$c_{i-1,L_2} = 0, \tag{4.133}$$

$$c_{i-1,R_2} = 0. \tag{4.134}$$

After the initialisation of the ring sets, the elements are set perpendicular on top of them. This initialisation is done in a similar manner to [45, p. 60 ff.] and is not elaborated any further.

Velocity initialisation

The initialisation of the planar pushbelt velocities is done via a planar analytic belt model explained in Section 4.1. The gained longitudinal belt velocity v is assumed to be constant in the push and loose part but variable in the pulleys. The longitudinal velocity in the cat's back is projected by the current angle γ from the rigid coordinates in the x and y direction via

$$\dot{x} = -\cos(\gamma)\,v \tag{4.135}$$

$$\dot{y} = -\sin(\gamma)\,v. \tag{4.136}$$

The angular velocity for the pulleys in the plane is initialised by the given boundary condition and calculated by the analytic model. The remaining velocities, out-of-plane and flexible DOFs, are initialised by zero.

4.3 Planar pre-integration

The main goal of the presented concept of a planar pre-integration is to use the fast planar CVT model of Subsection 6.1 to optimise the initial state of the spatial CVT model. The planar model is initialised with a geometric and quasi-static approach as described in Section 4.2 and 4.1 for the tapered or non-tapered case. Then, a dynamical planar pre-integration is executed. The results are exported and transformed to a spatial curve. With this information, the states for the spatial model initialisation are gained from the dynamical planar pre-integration. The flow of the simulation process is illustrated in Figure 4.15.

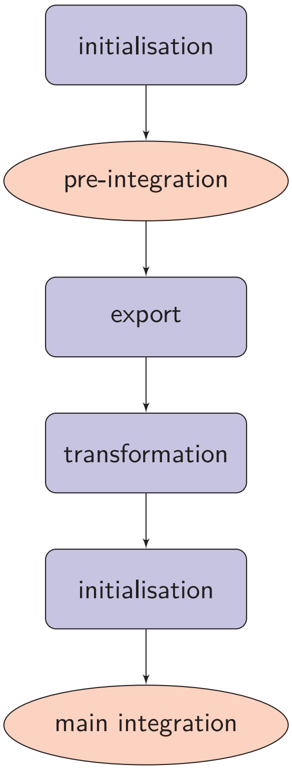

Figure 4.15: Simulation process with pre- and main integration

4.3.1 Interface set-up

The interface between planar pre- and spatial main integration (export and transformation) is explained in the following.

Export result of planar pre-integration

To enable a variable setting in the spatial main integration compared to the planar pre-integration, the state-vectors of the planar case have to be known continuously and not only at the nodes. As the initialisation of the pushbelt CVT model is based on the state of the ring sets, only this state vector is required. A closed NURBS (Non-Uniform Rational B-Spline) interpolation [39] is chosen to interpolate the discrete positions $\boldsymbol{r}_n$ and velocities $\boldsymbol{v}_n$ of the neutral fibre of the planar ring set

$$ {}_I\boldsymbol{r}(s) = \sum_n N_{r,n}(s)\, {}_I\boldsymbol{r}_n, \tag{4.137} $$

$$ {}_K\boldsymbol{v}(s) = \sum_n N_{v,n}(s)\boldsymbol{A}_{KI}\, {}_I\boldsymbol{v}_n. \tag{4.138} $$

Hereby, $\{N_{r,n}\}_n$ and $\{N_{v,n}\}_n$ are the basis functions for the interpolation. The flexible coordinates and rotations of the beam model are calculated from the position curve. The variable n denotes the number of nodes of the finite elements in the planar pre-integration. Note that the planar velocities are rotated into the local Frenet-frame before interpolation. This is required to successfully initialise the transformed spatial curve afterwards. The NURBS curves of the position and velocity of the planar ring set at the end of the pre-integration are written into a file which is the starting point for the following transformation. The required information for the initialisation of the spatial RCM beams and the other bodies is calculated from this information numerically. With this approach, e.g. a different number of finite elements for the ring sets and a different number of (steel) elements should become possible for the two integrations.

Transformation from planar to spatial

The z-coordinate (belt deflection) for the spatial case has to be added to the interpolated closed planar curve. For this purpose, the transition points from the pulleys to the straight parts have to be detected from the NURBS curve. This process has been done numerically by means of analysing the curvature with the help of student assistant Kilian Grundl. For the numerical detection of the transition points out of a spatial closed curve, the curvature of the curve is calculated at n_k equidistant points

$$ \kappa(s_i) = \left\| \boldsymbol{r}''\left(\frac{il}{n_k}\right) \right\|, \qquad \text{for } i = 0, \dots, n_k - 1. \tag{4.139} $$

These discrete curvature values are interpolated with NURBS to gain $\kappa(s)$ and the first derivative $\kappa'(s)$ is calculated. With some heuristics from the knowledge of where the transition points can be situated, they are gained by finding the largest jumps in the derivatives of the curvature. With the transition points the belt deflection is now added to the planar curve in the straight parts. Then, the resulting curve is again interpolated with NURBS resulting in the spatial initialisation curve.

4.3.2 Spatial numerical initialisation

The translational coordinates at the specified nodes for the spatial case are gained directly from the continuous position curve. In addition, the derivatives with respect to the arc length s can be calculated from the NURBS curve which are required for the next step.

Rotational coordinates

The angles from the reversed Cardan parametrisation are calculated from the position curve by means of differential geometry. The Frenet frame is derived from the curve by the derivatives with respect to the arc length and the cross product

$$
{}_I\boldsymbol{t}(s) = \frac{{}_I\boldsymbol{r}'(s)}{\|{}_I\boldsymbol{r}'(s)\|}, \quad {}_I\boldsymbol{n}(s) = \frac{{}_I\boldsymbol{r}''(s)}{\|{}_I\boldsymbol{r}''(s)\|}, \quad {}_I\boldsymbol{b}(s) = {}_I\boldsymbol{t}(s) \times {}_I\boldsymbol{n}(s). \tag{4.140}
$$

This information can be calculated continuously. A possible setting is shown in Figure 4.16. The three vectors of the numerically calculated Frenet frame form the transformation matrix from the body fixed system K into the inertial system I

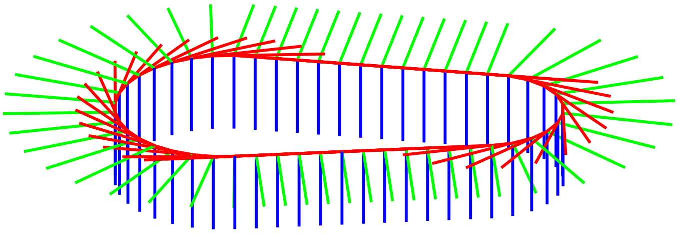

Figure 4.16: Frenet frames in CVT setting

$$
\boldsymbol{A}_{IK}(s) = \begin{pmatrix} a_{00} & a_{01} & a_{02} \\ a_{10} & a_{11} & a_{12} \\ a_{20} & a_{21} & a_{22} \end{pmatrix} = \Big({}_I\boldsymbol{t}(s), {}_I\boldsymbol{n}(s), {}_I\boldsymbol{b}(s)\Big). \tag{4.141}
$$

The matrix $\boldsymbol{A}_{IK}$ of the reverse Cardan parametrisation can be calculated analytically to

$$
\boldsymbol{A}_{IK} = \begin{pmatrix} \cos\gamma\cos\beta & \cos\gamma\sin\beta\sin\alpha - \sin\gamma\cos\alpha & \cos\gamma\sin\beta\cos\alpha + \sin\gamma\sin\alpha \\ \sin\gamma\cos\beta & \sin\gamma\sin\beta\sin\alpha + \cos\gamma\cos\alpha & \sin\gamma\sin\beta\cos\alpha - \cos\gamma\sin\alpha \\ -\sin\beta & \cos\beta\sin\alpha & \cos\beta\cos\alpha \end{pmatrix}. \tag{4.142}
$$

The three angles are obtained by equating (4.141) with (4.142):

$$
\beta = \arcsin(-a_{20}), \tag{4.143}
$$

$$\alpha = \begin{cases} \arctan\left(\frac{a_{21}}{a_{22}}\right), & \text{if } \cos\left(\beta\right) \neq 0, \\ 0, & \text{else,} \end{cases} \tag{4.144}$$

$$\gamma = \begin{cases} \arctan\left(\frac{a_{10}}{a_{00}}\right), & \text{if } \cos\left(\beta\right) \neq 0, \\ \arctan\left(-\frac{a_{01}}{a_{11}}\right), & \text{else.} \end{cases} \tag{4.145}$$

The two cases have to be distinguished to avoid dividing by zero. For $\cos(\beta) = 0$, the two rotation axes coincide and therefore one DOF for the rotation is lost. This is illustrated for the case $\beta = \pi/2$ where the rotation matrix reduces to

$$\boldsymbol{A}_{IK} = \begin{pmatrix} 0 & \sin(\alpha-\gamma) & \cos(\alpha-\gamma) \\ 0 & \cos(\alpha-\gamma) & \sin(\gamma-\alpha) \\ -1 & 0 & 0 \end{pmatrix}, \tag{4.146}$$

which is obtained by trigonometric identities. So in this case one angle is sufficient and the angle α is set to zero. In the current application of the pushbelt CVT the singularity does not occur as the x-y-plane is chosen in such a way that the angle β does not cross the critical values.

Deflection coordinates

As the in-plane and out-of-plane deflections are decoupled (as explained in Section 4.2.2), the two cases can be treated separately. All information required for the flexible DOFs can be gained from the position curve. The deviation of the straight run in the plane of motion (x-y-plane) is described by c_{L_2} and c_{R_2} and the deviation of the straight run in x-z-plane is described by c_{L_1} and c_{R_1}, see Figure 4.17. In this figure, the vectors are

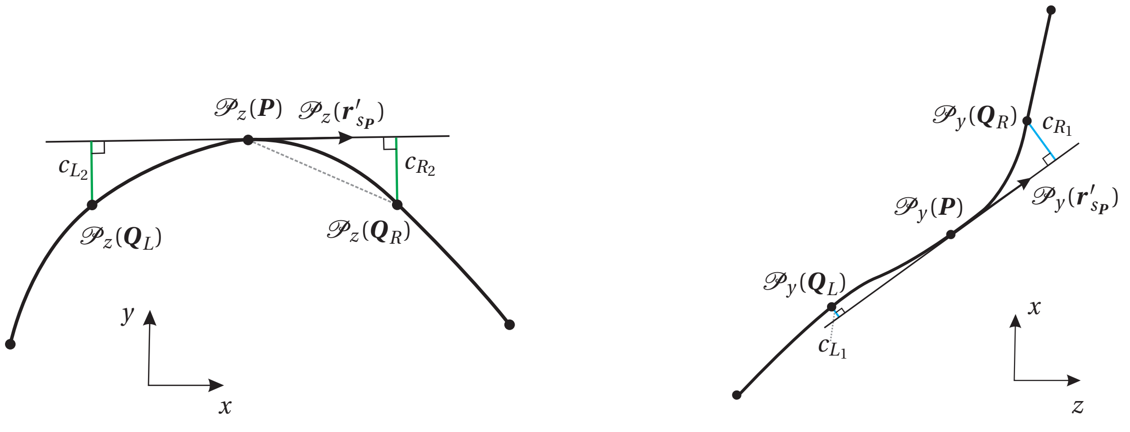

(a) Deflection in-plane (b) Deflection out-of-plane

Figure 4.17: Decoupled deflections of spatial RCM beam

projected into the correspondent planes, so the projector $\mathscr{P}_z$ projects the z-component to zero and thereby the vector into the x-y-plane

$$\mathscr{P}_z(\begin{pmatrix} r_x \\ r_y \\ r_z \end{pmatrix}) = \begin{pmatrix} r_x \\ r_y \\ 0 \end{pmatrix}. \tag{4.147}$$

Likewise, the projector $\mathscr{P}_y$ projects the y-component to zero. The position curve is known as a continuous curve. Therefore, the coordinates of the midpoint $\boldsymbol{P}$ of a finite element and the points $\boldsymbol{Q}_L$ and $\boldsymbol{Q}_R$ with a distance of $\mp l_0/4$ to $\boldsymbol{P}$ can be obtained from the NURBS curve. The deflection can now be interpreted as the distance of the points $\boldsymbol{Q}_L$ resp. $\boldsymbol{Q}_R$ to the tangent line through $\boldsymbol{P}$ given by $\boldsymbol{r}'(s_{\boldsymbol{P}})$. Generally, the distance of a point to a straight line has to be found. A formula from analytical geometry for the spatial case solves this problem. It results from equating the area of a triangle (cf. dotted line in Figure 4.17*a* with standard (half base · height) and cross product formula

$$\frac{1}{2} b \|\boldsymbol{r}'(s_{\boldsymbol{P}})\| \cdot c_* = \frac{1}{2} \|(\boldsymbol{Q}_* - \boldsymbol{P}) \times b\boldsymbol{r}'(s_{\boldsymbol{P}})\|, \tag{4.148}$$

whereby c_* denotes either the left (L) or right (R) distance which has to be calculated. Dividing both sides with the length of the base b and solving for c_*, the deflections are given by

$$c_* = \frac{\|(\boldsymbol{Q}_* - \boldsymbol{P}) \times \boldsymbol{r}'(s_{\boldsymbol{P}})\|}{\|\boldsymbol{r}'(s_{\boldsymbol{P}})\|} . \tag{4.149}$$

For the decoupled case, deflections for both directions can be calculated and the indexes 1 and 2 can be generated for c_*. From the spatial curve the two decoupled planes are derived by projecting the three vectors $(\boldsymbol{Q}, \boldsymbol{P}, \boldsymbol{r}')$ with $\mathscr{P}_z$ into the x-y- resp. with $\mathscr{P}_y$ into the x-z-plane (cf. Figure 4.17). After that Equation (4.149) is applied for the in-plane resp. out-of-plane vectors. In detail, c_{L_2} and c_{R_2} can be calculated from the x-y-components of the vectors and c_{L_1} and c_{R_1} out of the x-z-components as follows. Because of its structure, the cross product reduces vectors in the x-y-plane to the z-component and vectors in the x-z-plane to the y-component:

$$(\boldsymbol{Q}-\boldsymbol{P})\times\boldsymbol{r}' = \begin{cases} \begin{pmatrix} 0 \\ 0 \\ (q_x-p_x)r'_y-(q_y-p_y)r'_x \end{pmatrix}, & \text{if } \boldsymbol{Q},\boldsymbol{P},\boldsymbol{r}' \in \{\boldsymbol{w}\in\mathbb{R}^3; \quad w_z=0\}, \\ \\ \begin{pmatrix} 0 \\ (q_z-p_z)r'_x-(q_x-p_x)r'_z \\ 0 \end{pmatrix}, & \text{if } \boldsymbol{Q},\boldsymbol{P},\boldsymbol{r}' \in \{\boldsymbol{w}\in\mathbb{R}^3; \quad w_y=0\}. \end{cases} \tag{4.150}$$

Consequently, the deflection coordinates for in-plane (2) and out-of-plane (1) motion are given by

$$c_{*_2} = \frac{|(q_{*,x}-p_x)r'_y-(q_{*,y}-p_y)r'_x|}{\sqrt{(r'_x)^2+(r'_y)^2}}, \tag{4.151}$$

$$c_{*_1} = \frac{|(q_{*,z}-p_z)r'_x-(q_{*,x}-p_x)r'_z|}{\sqrt{(r'_x)^2+(r'_z)^2}}, \tag{4.152}$$

for the left resp. right value $\boldsymbol{Q}_L$ and $\boldsymbol{Q}_R$.

Velocity initialisation

The imported velocity vector in the K system is transformed back into the I system by means of the matrix (4.141). Thereby, the three velocity components u_x, u_y and u_z are obtained

$$\begin{pmatrix} u_x \\ u_y \\ u_z \end{pmatrix}(s) = \left({}_I\boldsymbol{t}(s), {}_I\boldsymbol{n}(s), {}_I\boldsymbol{b}(s)\right) {}_K\boldsymbol{v}(s). \tag{4.153}$$

The transformation of the velocity into the coordinate system K in (4.138) has to be done because of the geometric transformation from the planar to the spatial curve. As a result, the z-coordinate and the velocity direction of the curve is changed. Therefore, the local velocities in the K system are exported which can easily be transformed by the new transformation matrix of the changed curve position.

5 Enhancements concerning Interactions

This chapter treats enhancements concerning the interactions in the pushbelt CVT model. It is split into the unilateral element - ring set contact and the coupled quasi-static contact model for the element - sheave interaction. Both enhancements increase the level of detail of the contact models. A more accurate contact modelling effects the movement of single elements and hence the global dynamics of the pushbelt CVT model. Therefore, the contact modelling is of great importance for the quality of the simulation model. Some ideas of this chapter have been presented by the author in a compact form in [9].

5.1 Unilateral element - ring set contact

In the previous CVT model the ring sets were fixed in vertical and lateral direction (of the local element system) to the element by bilateral contacts. The movement of the ring sets relative to the elements was only possible in longitudinal direction with a friction law that enables force transmission between rings and elements.

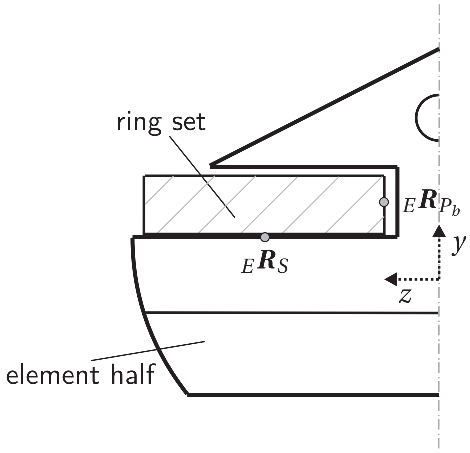

Figure 5.1: Bilateral element - ring set contact

The bilateral contact is modelled with two points at element saddle (S) and pillar (P), cf. Figure 5.1. They are given distinguishing right and left side [45]:

$$ {}_E\boldsymbol{R}_S = \begin{pmatrix} t_R/2 - t_S \\ h_P - h_S \\ \pm(w_P/4 + w_S/4) \end{pmatrix}, \qquad {}_E\boldsymbol{R}_{P_b} = \begin{pmatrix} t_R/2 - t_S \\ \tilde{h}_R + h_P - h_S \\ \pm(w_P/4 + w_S/4 - \tilde{w}R/2) \end{pmatrix}. \tag{5.1} $$

Due to the element symmetry in lateral direction, the plus-minus sign in z-direction includes both points. Through these bilateral contacts the relative movement of the ring set to the elements is disabled both in vertical and lateral direction. To lead the ring sets in a centred lateral position, the two bilateral pillar contact points ${}_E\boldsymbol{R}_{P_b}$ are not placed at the element pillar but shifted laterally, as it can be seen in Figure 5.1.

In this section, these restrictions concerning the relative element - ring movement are removed in different modular steps. The first step is the free movement in vertical direction, then additionally, in lateral direction and lastly, a ring tracking law is introduced to control the lateral movement of the ring sets.

5.1.1 Free movement in vertical direction

The bilateral saddle contact (cf. Figure 5.1) assumes an always closed contact at the saddle and no contact at the ear of the ring set and therefore no lifting of the ring sets relative to the element. In reality, the so-called ring-ear play exists and the element can move relatively to the ring sets in vertical direction. That means, a ring set can loose contact at the saddle and get into contact at the element ear.

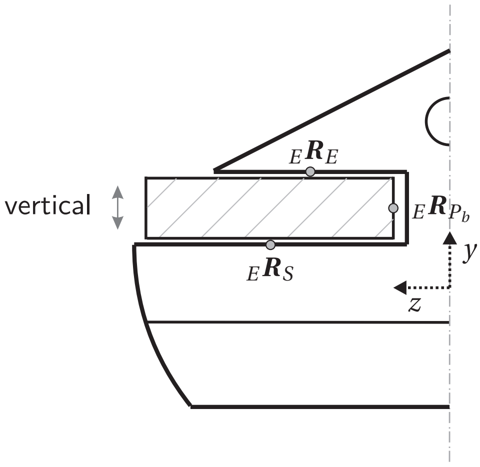

Figure 5.2: Unilateral element - ring set contact

To minimise computing time, only one additional element - ring contact point per element half is introduced. These two unilateral contact points at the element ear on the left and right side are placed at

$$
{}_E\boldsymbol{R}_E = \begin{pmatrix} t_R/2 - t_S \\ h_E - h_S \\ \pm(w_P/4 + w_E/4) \end{pmatrix}. \tag{5.2}
$$

The x-direction is chosen in the middle of the rocking edge thickness, y-direction at the ear height and z-direction at the half of the ear width, see Figure 5.2. Altogether, the vertical movement of the ring sets relative to the elements is possible - restricted by the boundaries element saddle and ear. The force laws at ${}_E\boldsymbol{R}_S$ and ${}_E\boldsymbol{R}_E$ are modelled unilateral rigid in normal direction in combination with a friction law in longitudinal direction. The bilateral saddle contacts ${}_E\boldsymbol{R}_P$ remain, hence, the lateral movement of the ring set is still locked in this configuration.

5.1.2 Free movement in lateral direction

In a second modular enhancement to the movement in vertical direction, the movement of the ring sets is enabled in lateral direction restricted by the element pillar, see Figure 5.3. To permit this movement, unilateral contact points at the element pillar are added to the pushbelt CVT model which differ only in the z-coordinate compared to the bilateral case

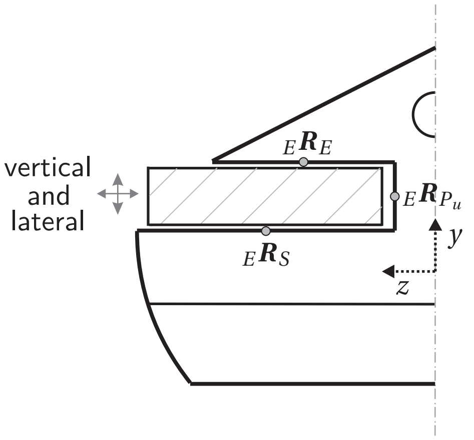

Figure 5.3: Unilateral pillar at element - ring set contact

$$
{}_E\boldsymbol{R}_{P_u} = \begin{pmatrix} t_R/2 - t_S \\ \tilde{h}_R/2 + h_P - h_S \\ \pm w_P/2 \end{pmatrix}.
$$

At both points, a unilateral rigid law is applied in normal direction. The contact points at element saddle and ear are modelled as in the last subsection.

This element - ring set contact constellation permits to investigate in which boundary settings the rings slide laterally and get in contact with the element pillar or the sheaves. These cases should not happen in reality as they cause material damages. By means of the simulation, these settings can be studied further to avoid costly experiments. This intermediate stage leads directly to the so called ring tracking.

5.1.3 Ring tracking

By ring tracking, the lateral movement of the ring sets is controlled to prevent them from contacting the boundaries. The theory behind it comes from the running behaviour of belts on crowned pulleys resulting from the stress states of a traction ring. For further information on this phenomenon see [40]. This behaviour is imitated by concave shaped element saddles, as rings on concave shaped surfaces tend to run on the top of the surface to find an equilibrium of stresses.

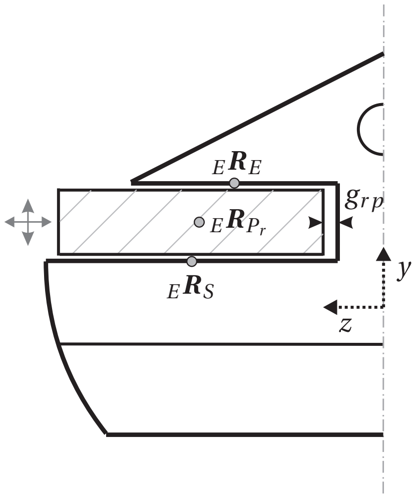

Figure 5.4: Ring tracking at element - ring set contact

In the model, a first approach to integrate this phenomenon has been realised. The lateral control of the ring is implemented by a regularised bilateral contact in normal direction including a specific force law without changing the element contour, see Figure 5.4. The aim of the ring tracking model is to penalise the movement away from the neutral lateral position by a force function. The penalisation increases with the ring set offset with respect to the centred position until it reaches a maximum distance. This maximum distance - the ring-pillar gap - is the difference between the z-coordinate of the bilateral $_E\boldsymbol{R}_{P_b}$ and unilateral pillar contact point $_E\boldsymbol{R}_{P_u}$

$$g_{rp} = \left(\frac{w_P}{4} + \frac{w_S}{4} - \frac{\tilde{w}_R}{2}\right) - \frac{w_P}{2} = \frac{w_S - w_P}{4} - \frac{\tilde{w}_R}{2} \,. \tag{5.3}$$

As the ring set is situated in the middle position of the element saddle width, the ring-pillar gap between ring set and element pillar and between ring set and sheave is equal in both lateral directions. Because of the element symmetry, g_{rp} is equal on the left and right side of the element.

The chosen force law enables and tolerates the lateral movement until half of the gap $g_{rp}/2$ in a manner of linear relationship with peak L. However, the full gap distance g_{rp} should not occur. Hence, it is penalised with a huge value F. Thereby, a collision of the ring sets with the boundaries is prevented. This yields the following symmetric interpolation problem in Table 5.1 which punishes the right and left lateral move identically. The two force variables $F \gg L$ are input parameters. This simple ring tracking law is interpolated below.

Table 5.1: Interpolation table of ring tracking model

i	0	1	2	3	4
x_i	$-g_{rp}$	$-\frac{g_{rp}}{2}$	0	$\frac{g_{rp}}{2}$	g_{rp}
y_i	F	L	0	$-L$	$-F$

A polynomial of global degree three simplifies because of point symmetry to

$$P(x) = \frac{-4F+8L}{3g_{rp}^3}\,x^3 + \frac{F-8L}{3g_{rp}}\,x. \tag{5.4}$$

The problem that arises with the polynomial approach or a spline approach is the under- and overshoot in the area $[-g_{rp}/2,\ g_{rp}/2]$ resulting from the specific data, see Figure 5.5. Therefore, the *monotone piecewise cubic interpolation* [15] was applied. It monotonically interpolates monotone data, as it is required in this case. For each subinterval $[x_i,\ x_{i+1}]$, the cubic polynomial is given by

$$\begin{aligned} p(x) &= \frac{3hs^2-2s^3}{h^3}\,y_{i+1} + \frac{h^3-3hs^2+2s^3}{h^3}\,y_i + \frac{s^2(s-h)}{h^2}\,y'_{i+1} + \frac{s(s-h)^2}{h^2}\,y'_i \\ &= H_1(x)y_{i+1} + H_2(x)y_i + H_3(x)y'_{i+1} + H_4(x)y'_i \end{aligned} \tag{5.5}$$

with a fixed

$$h = x_{i+1} - x_i = g_{rp}/2 \quad \forall i, \tag{5.6}$$

because of the equidistant nodes. The slopes y'_{i+1} and y'_i of this piecewise polynomial are calculated according to [32]. They simplify as the data is equidistant and monotone. Outside the interval $[-g_{rp},\ g_{rp}]$ the function is extended C^1 continuous by a linear function with slope y'_0 at $\pm g_{rp}$. The implementation is shown in a compact form combining the positive and negative sections because of the symmetry with respect to

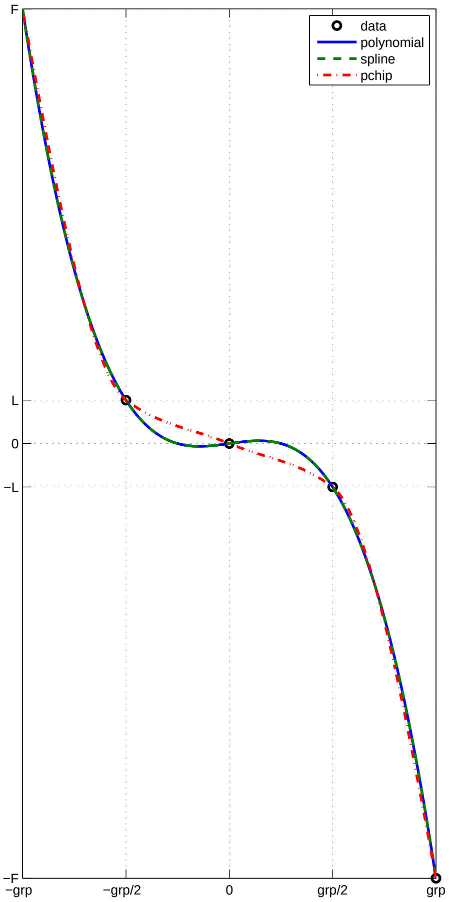

Figure 5.5: Different interpolation schemes for ring tracking force function

the origin. In total, the three sections are given by:

1. Section: $-g_{rp}/2 \le x \le g_{rp}/2$:

$$p(x) = -\operatorname{sgn}(x)\left(H_2(x)\,L + H_3(x)\,y'_2 + H_4(x)\,y'_1\right) \tag{5.7}$$

   with $s = -|x| + g_{rp}/2$.

2. Section: $-g_{rp} \le x < -g_{rp}/2$ and $g_{rp}/2 < x \le g_{rp}$:

$$p(x) = -\operatorname{sgn}(x)\left(H_1(x)\,L + H_2(x)\,F + H_3(x)\,y'_1 + H_4(x)\,y'_0\right) \tag{5.8}$$

   with $s = -|x| + g_{rp}$.

3. Section: $x < -g_{rp}$ and $x > g_{rp}$:

$$p(x) = -\operatorname{sgn}(x)\left(F + y'_0 g_{rp} - y'_0 |x|\right). \tag{5.9}$$

The unknown derivatives y'_i are determined so that the function is shape-preserving to the data. In this specific case of monotone data with equidistant nodes they equal the harmonic mean of the two neighbouring slopes. The coefficients of the polynomials are calculated to

$$d_0 = \frac{L-F}{h}, \qquad d_1 = \frac{-L}{h}, \qquad d_2 = d_1, \tag{5.10}$$

$$y'_0 = \frac{3d_0 - d_1}{2}, \qquad y'_1 = \frac{2}{1/d_0 + 1/d_1}, \qquad y'_2 = d_1. \tag{5.11}$$

This approach interpolates the given data monotonically (cf. 'pchip' in Figure 5.5) and was implemented into the pushbelt CVT model. The chosen ring tracking laws are not physically based, thus, a further model refinement would be necessary for a more detailed representation of this phenomenon.

5.2 Coupled contact law for element - sheave contact

The aim of this section is to derive a spatial coupled quasi-static contact model for the normal direction of the three-dimensional element - pulley sheave contact in the CVT model. This normal contact law is combined with a friction law in tangential directions. By the *Maxwell contact* model the elements are coupled through the elasticity of the pulley in the contact. Therefore, the sheaves deform on the whole contact arc which leads together with the pre-stressed ring sets to the phenomenon of spiral running, i.e. the running radius is not constant in the pulley arcs cf. [45]. Preliminary work has been done in the planar case in [8, 17]. This approach has been generalised to the spatial case. The structure of this section follows Chapter 3 of the supervised diploma thesis [19]. The idea and a validation on two academic examples of the Maxwell contact has been presented in [20].

5.2.1 Demonstration of coupling

The principle of a coupled quasi-static contact is demonstrated in Figure 5.6. A cantilever beam is in contact with two sticks at point 1 and 2, cf. [17]. The undeformed contours are dotted. In the case of a non-coupled contact law the two sticks are not linked by the elasticity of the beam. One contact with a rigid distance smaller than zero does not influence another contact with rigid distance smaller than zero. That means both sticks would be in contact with the beam in its undeformed position. However, in reality for the static case, the contact force of the stick 1 closer to the clamped end bends the beam so that stick 2 is not in contact. This coupling can be realised in two ways. Either the deformation is considered only quasi-statically in the contact time, as the Maxwell contact does, or dynamically by means of flexible bodies. The advantage of the Maxwell contact is that rigid body dynamics can be used which is not as expensive in calculation time as flexible body dynamics.

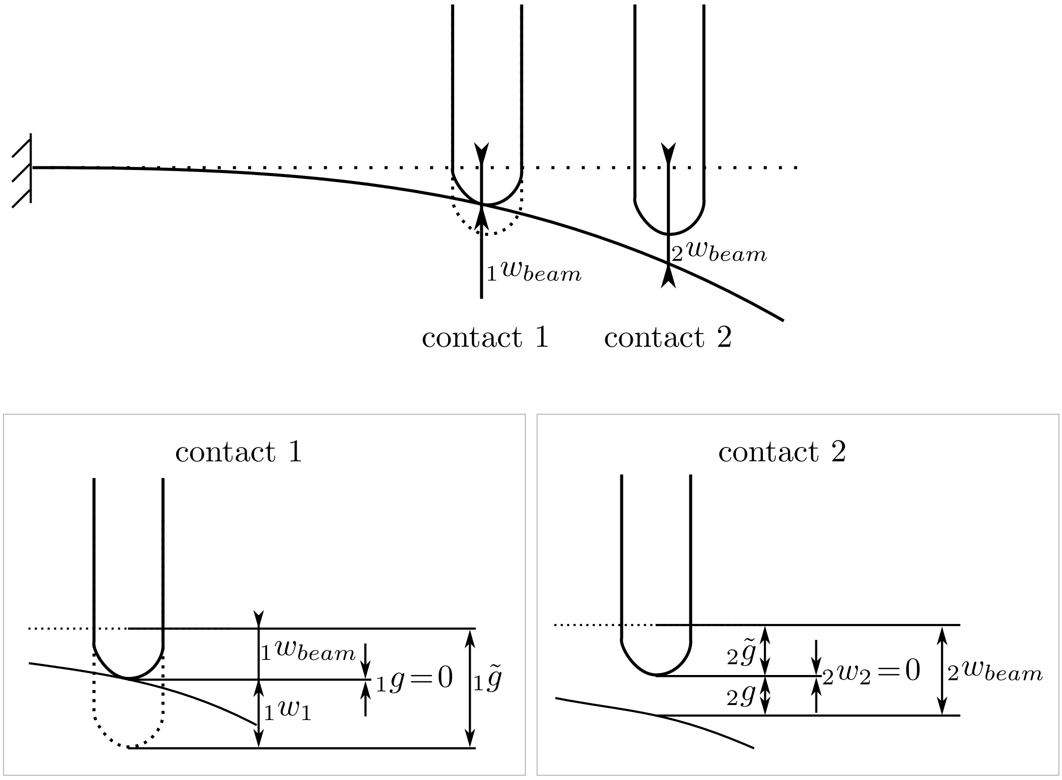

Figure 5.6: Coupling illustrated on a cantilever beam [19, p. 10]

In order to distinguish between position and contour the following notation is introduced. The left subscript denotes the position (point 1 or 2) and the right subscript the contour of the body that is in contact (beam, stick 1 and stick 2). For contact 1 shown in the bottom left of Figure 5.6 the following equation holds

$${}_1g = {}_1w_{beam} + {}_1w_1 + {}_1\tilde{g} = 0,$$

with the elastic distance g, the deformations w of both contours and the rigid distance $\tilde{g}$. The elastic distance is measured between both deformed contours and the rigid distance between the undeformed contours. As both undeformed contours are penetrated, $\tilde{g}$ is negative. The deformations of the beam, ${}_1w_{beam}$, and stick 1, ${}_1w_1$, are both positive. The elastic distance as the sum of these three variables is zero which means that contact 1 is closed. A positive contact force acts and deforms the beam and stick 1.

In contact 2, on the bottom right of Figure 5.6, also both undeformed contours are penetrated. However, because of the coupling with contact 1 and the resulting bending of the beam, contact 2 is not closed. Therefore, the deformation of stick 2, ${}_2w_2$, is equal to zero

$$ {}_2g = {}_2w_{beam} + \underbrace{{}_2w_2}_{=0} + {}_2\tilde{g} > 0. $$

The model, demonstrated on this simple example, is derived in general for the spatial case in the following.

5.2.2 Maxwell's reciprocal theorem

Maxwell's reciprocal theorem is derived out of the two principles of superposition and conservation of energy, cf. [37]. It specifies the influence between forces and deformations of linear elastic bodies in a static equilibrium. The influence matrix

$$ \boldsymbol{C} = ({}_iC_j)_{ij} \in \mathbb{R}^{n\times n} $$

stores the influence numbers ${}_iC_j$, which describe the linear relationship between a single force ${}_j\lambda$ acting on a point j and the resulting deformation ${}_iw({}_j\lambda)$ at a point i in direction of λ_i given by the formula

$$ {}_iw({}_j\lambda) = {}_iC_j\ {}_j\lambda, \tag{5.12} $$

shown in Figure 5.7. As a consequence of the principle of superposition, the deformation at a point i resulting of n forces at different points on the body is given as the sum

$$ {}_iw := {}_iw(\boldsymbol{\lambda}) = \sum_{j=1}^{n} {}_iC_j\ {}_j\lambda = {}_i\boldsymbol{c}\boldsymbol{\lambda}. \tag{5.13} $$

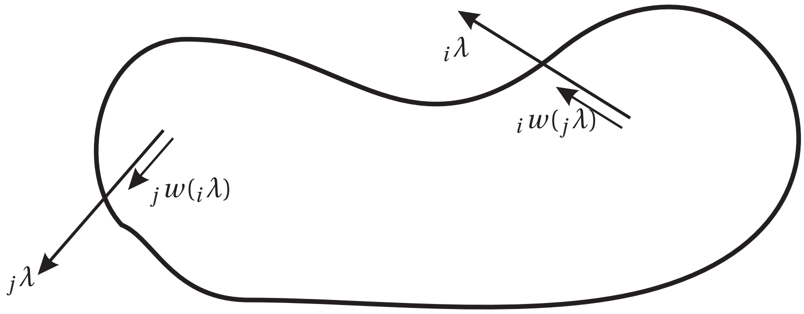

Figure 5.7: Influence between forces and deformations for a linear elastic body [19]

The vector ${}_i\boldsymbol{c}$ is the i-th row vector of the influence matrix

$$\boldsymbol{C} = \begin{pmatrix} {}_1\boldsymbol{c} \\ \vdots \\ {}_n\boldsymbol{c} \end{pmatrix}$$

and the vector $\boldsymbol{\lambda} = ({}_1\lambda, \dots, {}_n\lambda)^T$ comprises the single forces. That means the deformation at one point depends on all forces applied on the body. For the desired application of the Maxwell contact the resulting deformations are only of interest at the points where the single forces act on the body. Therefore, $\boldsymbol{C}$ is a square matrix. The n deformations are stored in the vector

$$\boldsymbol{w} = \boldsymbol{w}(\boldsymbol{\lambda}) = \boldsymbol{C}\boldsymbol{\lambda} \in \mathrm{I\!R}^n. \tag{5.14}$$

Considering two forces on the points i and j of a body, their corresponding deformations and the principle of conservation of energy, then Maxwell's theorem specifies that the influence numbers ${}_iC_j$ and ${}_jC_i$ are equal. Thus, the influence matrix is symmetric

$${}_iC_j = {}_jC_i \Leftrightarrow \boldsymbol{C} = \boldsymbol{C}^T. \tag{5.15}$$

From the physical point of view it shows the reciprocity that the deformation at a point i caused by a force at a point j is the same as the deformation on the point j caused by a force acting on a point i.

5.2.3 Local elastic contact kinematics

To derive the Maxwell force law, appropriate local contact kinematics for the elastic case in addition to the rigid case of Section 2.3 have to be predefined. A contact situation is considered where two contours (1 and 2) are in contact at a point i, cf. Figure 5.8. It shows both the undeformed and deformed state of each contour. Let $\boldsymbol{\lambda}$ be the vector of all contact forces that act on both bodies. Due to the contact forces both contours deform in point i and the resulting deformations of contour 1 and 2 are ${}_iw_1(\boldsymbol{\lambda})$ and ${}_iw_2(\boldsymbol{\lambda})$. The elastic normal distance at point i is the sum of both deformations and the rigid normal distance ${}_i\tilde{g}$

$$\begin{aligned} {}_ig(\boldsymbol{\lambda}) &= {}_iw_1(\boldsymbol{\lambda}) + {}_iw_2(\boldsymbol{\lambda}) + {}_i\tilde{g} \\ &= {}_i\boldsymbol{c}_1\boldsymbol{\lambda} + {}_i\boldsymbol{c}_2\boldsymbol{\lambda} + {}_i\tilde{g} \\ &= {}_i\boldsymbol{c}\boldsymbol{\lambda} + {}_i\tilde{g}. \end{aligned} \tag{5.16}$$

The row vector ${}_i\boldsymbol{c}_1$ comprises the influence numbers of all single forces acting on point i concerning contour 1 and ${}_i\boldsymbol{c}_2$ those concerning contour 2. Both influence vectors are

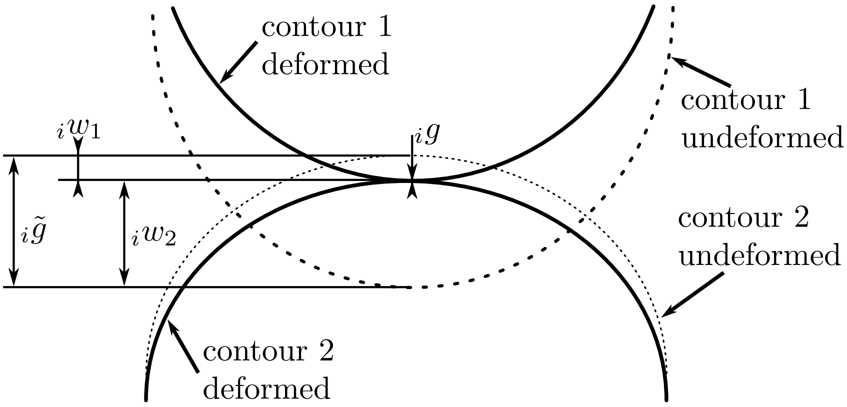

Figure 5.8: Local elastic contact kinematics [19, p. 12]

summed up in one row vector which is possible because of the linearity

$$_i\boldsymbol{c} = {_i\boldsymbol{c}_1} + {_i\boldsymbol{c}_2}. \tag{5.17}$$

Hence, every row vector $_i\boldsymbol{c}$ contains the contribution of both contours involved in a contact point i.

5.2.4 Maxwell force law

The *Maxwell force law* is a linear complementarity problem (LCP) on the basis of Maxwell's reciprocal theorem for the contact situation of Subsection 5.2.3 and a complementarity condition. The elastic distances $_ig$ are set up for all contact points i and summarised in a matrix vector notation

$$\begin{aligned} &_ig = {_i\boldsymbol{c}}\boldsymbol{\lambda} + {_i\tilde{g}} \quad \forall i = 1,\dots,n \\ &\Leftrightarrow \boldsymbol{g} = \boldsymbol{C}\boldsymbol{\lambda} + \tilde{\boldsymbol{g}}. \end{aligned} \tag{5.18}$$

The result is a linear equation with the symmetric influence matrix $\boldsymbol{C}$ where each row vector correlates to one contact point. In addition, the constraints that both the elastic distances and the contact forces are non-negative, have to be satisfied. That means the bodies cannot penetrate and only push each other. For this case the inequality conditions in the following element-wise notation are introduced

$$_ig \geq 0 \;\; \forall i = 1,\dots,n \;\; \Leftrightarrow \boldsymbol{g} \geq \boldsymbol{0} \tag{5.19}$$

$$_i\lambda \geq 0 \;\; \forall i = 1,\dots,n \;\; \Leftrightarrow \boldsymbol{\lambda} \geq \boldsymbol{0}. \tag{5.20}$$

In a third step the complementarity condition is demanded. It regulates the relationship between the elastic distance and the contact force for the possible cases of an open and a closed contact. If a contact is closed the contact force can be positive and if the contact is open the contact force has to be zero

$$
{}_i g = 0 \;\wedge\; {}_i \lambda \geq 0, \tag{5.21}
$$

$$
{}_i g > 0 \;\wedge\; {}_i \lambda = 0. \tag{5.22}
$$

Therefore, either the entry of the distance or the force vector or both entries vanish, which means that the vectors are orthogonal

$$
\boldsymbol{g}^T \boldsymbol{\lambda} = 0 \Leftrightarrow \boldsymbol{g} \perp \boldsymbol{\lambda}. \tag{5.23}
$$

Non-negativity and complementarity are summarised to an inequality complementarity condition similar to the unilateral contact, but now for the elastic distances

$$
\boldsymbol{0} \leq \boldsymbol{g} \perp \boldsymbol{\lambda} \geq \boldsymbol{0}. \tag{5.24}
$$

Altogether the *Maxwell force law* contains the LCP with the linear system and the constraints derived in the previous steps

$$
\boldsymbol{g} = \boldsymbol{C}\boldsymbol{\lambda} + \tilde{\boldsymbol{g}}, \tag{5.25a}
$$

$$
\boldsymbol{0} \leq \boldsymbol{g} \perp \boldsymbol{\lambda} \geq \boldsymbol{0}. \tag{5.25b}
$$

5.2.5 Solution of the Maxwell force law

The Maxwell force law is expressed by a LCP with the unknowns $\boldsymbol{g}$ and $\boldsymbol{\lambda}$. For its solution many strategies exist. They can be categorised in two sections, the direct and indirect methods. The direct methods are pivoting methods which test different solutions until the exact solution is found. As a special case of the pivoting methods the Lemke solver will be outlined below. The indirect methods are iterative methods which approximate the solution. Starting with an initial value, they try to get closer to the solution in each step. Here, the reformulated proximal point version of the LCP resulting in a nonlinear system is shown which is solved by a fixed-point or Newton method. Note that in the following for reasons of simplicity the subscript has been adapted so that the right subscript denotes the index of a vector.

Pivoting methods and Lemke's algorithm

Lemke's algorithm is a direct method to solve a LCP using pivoting strategies. The main ideas of pivoting methods and Lemke's algorithm are described in the following similar to [30, 58].

A *pivoting method* works as follows. In the case of $\tilde{\boldsymbol{g}} \geq \boldsymbol{0}$, a solution of the LCP (5.25) can easily be given by setting $\boldsymbol{\lambda} = \boldsymbol{0}$ and $\boldsymbol{g} = \tilde{\boldsymbol{g}}$. Otherwise, variables have to be exchanged (pivoted) in a certain way until the conditions of (5.25) are satisfied. Let $I \subset \{1, \ldots, n_{\boldsymbol{g}}\}$

and $K \subset \{1, \dots, n_{\boldsymbol{\lambda}}\}$ denote two index sets which are subsets of the indexes of $\boldsymbol{g}$ and $\boldsymbol{\lambda}$ with the same number of elements $|I| = |K|$. Let I^C and K^C denote the corresponding set complements. Then, a *partition* of the linear system is obtained by changing rows and columns of (5.25a)

$$\begin{pmatrix} \boldsymbol{g}_I \\ \boldsymbol{g}_{I^C} \end{pmatrix} = \begin{pmatrix} \boldsymbol{C}_{IK} & \boldsymbol{C}_{IK^C} \\ \boldsymbol{C}_{I^CK} & \boldsymbol{C}_{I^CK^C} \end{pmatrix} \begin{pmatrix} \boldsymbol{\lambda}_K \\ \boldsymbol{\lambda}_{K^C} \end{pmatrix} + \begin{pmatrix} \tilde{\boldsymbol{g}}_I \\ \tilde{\boldsymbol{g}}_{I^C} \end{pmatrix}, \tag{5.26}$$

so that $\boldsymbol{C}_{IK}$ is non-singular. By exchanging $\boldsymbol{g}_I$ and $\boldsymbol{\lambda}_K$, having the same number of elements, a *pivoted system*

$$\begin{pmatrix} \boldsymbol{\lambda}_K \\ \boldsymbol{g}_{I^C} \end{pmatrix} = \boldsymbol{C}' \begin{pmatrix} \boldsymbol{g}_I \\ \boldsymbol{\lambda}_{K^C} \end{pmatrix} + \tilde{\boldsymbol{g}}' \tag{5.27}$$

is gained, in which the variables are mixed. To distinguish between them, the variable set $\{\boldsymbol{\lambda}_K, \boldsymbol{g}_{I^C}\}$ is termed basic and $\{\boldsymbol{g}_I, \boldsymbol{\lambda}_{K^C}\}$ non-basic variables. The transformed matrix $\boldsymbol{C}'$ and the vector $\tilde{\boldsymbol{g}}'$ can be calculated by simple linear algebra to

$$\begin{aligned} \boldsymbol{C}' &= \begin{pmatrix} \boldsymbol{C}_{IK}^{-1} & -\boldsymbol{C}_{IK}^{-1}\boldsymbol{C}_{IK^C} \\ \boldsymbol{C}_{I^CK}\boldsymbol{C}_{IK}^{-1} & \boldsymbol{C}_{I^CK^C} - \boldsymbol{C}_{I^CK}\boldsymbol{C}_{IK}^{-1}\boldsymbol{C}_{IK^C} \end{pmatrix}, \\ \tilde{\boldsymbol{g}}' &= \begin{pmatrix} \tilde{\boldsymbol{g}}'_I \\ \tilde{\boldsymbol{g}}'_{I^C} \end{pmatrix} = \begin{pmatrix} -\boldsymbol{C}_{IK}^{-1}\tilde{\boldsymbol{g}}_I \\ \tilde{\boldsymbol{g}}_{I^C} - \boldsymbol{C}_{I^CK}\boldsymbol{C}_{IK}^{-1}\tilde{\boldsymbol{g}}_I \end{pmatrix}. \end{aligned} \tag{5.28}$$

Altogether, the goal of the pivoting strategies is to partition the LCP and pivot it so that the two index sets I and K are equal and the transformed vector $\tilde{\boldsymbol{g}}'$ in (5.27) is greater or equal to zero:

$$I = K \quad \wedge \quad \tilde{\boldsymbol{g}}' \geq \boldsymbol{0}. \tag{5.29}$$

If condition (5.29) is satisfied, the solutions can easily be found by setting the vector of the non-basic variables to zero and the basic variables to $\tilde{\boldsymbol{g}}'$. For the original LCP this results in the form

$$\boldsymbol{g} = \begin{pmatrix} \boldsymbol{0} \\ \tilde{\boldsymbol{g}}'_{I^C} \end{pmatrix}, \qquad \boldsymbol{\lambda} = \begin{pmatrix} \tilde{\boldsymbol{g}}'_I \\ \boldsymbol{0} \end{pmatrix}. \tag{5.30}$$

Trying all possible combinations by pairwise pivoting the variables will result in the solution in a finite number of steps.

This exchanging of variables is done in a strategic way in *Lemke's algorithm*. The LCP is augmented by an auxiliary variable λ_0 and a covering vector greater than zero, here $\mathbb{1} = (1, 1, \dots, 1)^T$:

$$\boldsymbol{g} = \bar{\boldsymbol{C}} \begin{pmatrix} \boldsymbol{\lambda} \\ \lambda_0 \end{pmatrix} + \tilde{\boldsymbol{g}}, \qquad \bar{\boldsymbol{C}} = \begin{pmatrix} \boldsymbol{C} & \mathbb{1} \end{pmatrix}. \tag{5.31}$$

Through this additional variable the number of elements relate subsequently

$$n_{\boldsymbol{\lambda}} = n_{\boldsymbol{g}} + 1.$$

The algorithm is splitted into the following three sections, only slightly adapted from [30, 58]. It is assumed that $\tilde{\boldsymbol{g}} \ngeq \mathbf{0}$, i.e. it has at least one negative entry, otherwise the solution can directly be given by $\boldsymbol{\lambda} = \mathbf{0}$.

1. **Initial pivot step:** Determine $r = \arg\min_i \{\tilde{g}_i\}$, pivot λ_0 with g_r and assign the driving variable y_r to λ_r. Compute $\tilde{\boldsymbol{g}}'$ and the column $\boldsymbol{c}_r'$ of $\bar{\boldsymbol{C}}'$ corresponding to the driving index r.

2. **Termination criteria:** If $\boldsymbol{c}_r' \geq \mathbf{0}$, then terminate without solution. Otherwise, calculate $s = \arg\min_i \{-\tilde{g}_i'/c_i';\ c_i' < 0\}$ and set y_s to the basic variable with index s. If $y_s = \lambda_0$, then pivot y_s and y_r and terminate succesfully - the resulting $\tilde{\boldsymbol{g}}''$ solves the LCP. Otherwise, proceed with next step.

3. **Pivot step:** Pivot y_s and y_r. Assign y_r to the complement of y_s (i.e. the corresponding entry in the non-basic variable) and go to previous step.

To find a solution it is required that the column $\boldsymbol{c}_r'$ has at least one negative entry cf. [13]. Otherwise, the Maxwell force law has either no solution or is not solvable by this method. After the initial pivot step, $\tilde{\boldsymbol{g}}' \geq \mathbf{0}$ is always valid as the covering vector has been chosen to be greater than zero. But the other condition of (5.29), that the two index sets are identical, has still to be fulfilled by removing 0 out of I and r out of J which is done if $y_s = \lambda_0$ in the second step above to gain a complementary solution.

For practical cases the total complexity of Lemke's algorithm typically is polynomial with $O(n^3)$, however, there are some problems where the complexity 'explodes' to $O(2^n)$ cf. [30]. The explained method is the standard Lemke's algorithm. More advanced versions of it exist. For a more robust variant see [58], where amongst others the possible tie in the second step is resolved as the minimum in the test

$$\underset{i \in \{1,\dots,n_{\boldsymbol{g}}\}}{\arg\min} \{-\tilde{g}_i'/c_i';\quad c_i' < 0\} \tag{5.32}$$

can occur at several arguments i. In addition, numerical problems in the inversion of the matrix $\boldsymbol{C}_{IK}$ are addressed, which could lead to inaccurate results. Another enhancement shown in [30] focuses on a faster implementation of Lemke's algorithm.

Iterative schemes using proximal point formulation

As the complementarity and proximal point formulation is equivalent [47], the constraints can be reformulated using the projection functions of Section 2.4. This yields a nonlinear system comprising the linear equation and the prox functions which can be solved by a non-smooth Newton or fixed-point iterator. In general, the iterative schemes are faster than the pivoting methods.

The reformulation of one line of the constraints yields

$$\begin{aligned} & g_i \geq 0, \quad \lambda_i \geq 0, \quad g_i \lambda_i = 0 && \text{(5.33a)} \\ \Leftrightarrow \quad & \lambda_i = \operatorname*{prox}_{\mathrm{IR}^+}(\lambda_i - r g_i), && \text{(5.33b)} \end{aligned}$$

with the one-dimensional set $\mathrm{IR}^+ := \{x \in \mathrm{IR}; \quad x \geq 0\}$ and a positive coefficient r. To point out the equivalence in (5.33), as an example, the direction (5.33b) → (5.33a) is pictured. The other direction and a deeper insight in this can be found in [47]. Two cases have to be distinguished: If $\lambda_i - r g_i < 0$, the prox function is mapped to zero and it follows

$$\lambda_i = \operatorname*{prox}_{\mathrm{IR}^+}(\lambda_i - r g_i) = 0 \quad \wedge \quad g_i > 0. \tag{5.34}$$

Otherwise, if $\lambda_i - r g_i \geq 0$, the preimage is mapped onto itself and therefore

$$\lambda_i = \operatorname*{prox}_{\mathrm{IR}^+}(\lambda_i - r g_i) = \lambda_i - r g_i \geq 0 \quad \Rightarrow g_i = 0 \quad \wedge \quad \lambda_i \geq 0. \tag{5.35}$$

Altogether, the whole LCP in element-wise notation with the proximal point formulation consists of a linear and a nonlinear system

$$\begin{aligned} g_i &= \sum_{j=1}^{n} {}_iC_j \, \lambda_j + \tilde{g}_i \qquad \forall i = 1, \ldots, n && \text{(5.36a)} \\ \lambda_i &= \operatorname*{prox}_{\mathrm{IR}^+}(\lambda_i - r g_i) \qquad \forall i = 1, \ldots, n. && \text{(5.36b)} \end{aligned}$$

The system (5.36) is solved by two different solution strategies, the fixed-point and Newton iteration. With the definition

$$\boldsymbol{x} := \begin{pmatrix} \boldsymbol{g} \\ \boldsymbol{\lambda} \end{pmatrix}, \tag{5.37}$$

the vector notation for the multidimensional fixed-point iteration is given by

$$\boldsymbol{x} = \boldsymbol{F}_F(\boldsymbol{x}) := \begin{bmatrix} \boldsymbol{C}\,\boldsymbol{\lambda} + \tilde{\boldsymbol{g}} \\ \mathbf{prox}_{\mathrm{IR}^{n+}}(\boldsymbol{\lambda} - r\boldsymbol{g}) \end{bmatrix}. \tag{5.38}$$

For this special case of the set $\mathrm{IR}^{n+} := \{\boldsymbol{x} \in \mathrm{IR}^n; \quad \boldsymbol{x} \geq \boldsymbol{0}\}$, the components x_i are decoupled. Thus, the elements of the prox functions can be assembled into one vector

$$\underset{\mathrm{I\!R}^{n+}}{\mathbf{prox}}(\boldsymbol{\lambda} - r\boldsymbol{g}) = \begin{pmatrix} \mathrm{prox}_{\mathrm{I\!R}^+}(\lambda_1 - r g_1) \\ \vdots \\ \mathrm{prox}_{\mathrm{I\!R}^+}(\lambda_n - r g_n) \end{pmatrix}. \tag{5.39}$$

The scheme for the *fixed-point iteration* has the form

$$\boldsymbol{x}^{i+1} = \boldsymbol{F}_F(\boldsymbol{x}^i), \qquad i \geq 0. \tag{5.40}$$

The starting value $\boldsymbol{x}_0 = \binom{\boldsymbol{g}_0}{\boldsymbol{\lambda}_0}$ is calculated as

$$g_{i,0} = \begin{cases} \tilde{g}_i, & \text{for } \tilde{g}_i \geq 0, \\ 0, & \text{for } \tilde{g}_i < 0, \end{cases} \tag{5.41}$$

$$\lambda_{i,0} = \begin{cases} 0, & \text{for } \tilde{g}_i \geq 0, \\ -\frac{n}{\mathrm{tr}(\boldsymbol{C})}\tilde{g}_i, & \text{for } \tilde{g}_i < 0, \end{cases} \tag{5.42}$$

with some knowledge taken from the pivoting methods. Hereby, the arithmetic mean of the trace of $\boldsymbol{C}$ is a measure for the mean eigenvalue, as the trace is equal to the sum of the eigenvalues μ_i of $\boldsymbol{C}$

$$\mathrm{tr}(\boldsymbol{C}) = \sum_{i=1}^{n} {}_iC_i \overset{!}{=} \sum_{i=1}^{n} \mu_i. \tag{5.43}$$

The system (5.36) in root formulation for the Newton method in element-wise notation satisfies

$$0 = g_i - \sum_{j=1}^{n} {}_iC_j\, \lambda_j - \tilde{g}_i \qquad \forall i = 1, \ldots, n, \tag{5.44a}$$

$$0 = \lambda_i - \underset{\mathrm{I\!R}^+}{\mathrm{prox}}(\lambda_i - r g_i) \qquad \forall i = 1, \ldots, n. \tag{5.44b}$$

With the multidimensional function

$$\boldsymbol{F}_N(\boldsymbol{x}) := \begin{bmatrix} \boldsymbol{g} - \boldsymbol{C}\,\boldsymbol{\lambda} - \tilde{\boldsymbol{g}} \\ \boldsymbol{\lambda} - \mathbf{prox}_{\mathrm{I\!R}^{n+}}(\boldsymbol{\lambda} - r\boldsymbol{g}) \end{bmatrix}, \tag{5.45}$$

the compact matrix vector notation for the *multidimensional Newton method* is given by

$$D\boldsymbol{F}_N(\boldsymbol{x}^i)\Delta\boldsymbol{x}^i = -\boldsymbol{F}_N(\boldsymbol{x}^i). \tag{5.46}$$

The Jacobian matrix is denoted with $\boldsymbol{DF}_N(\boldsymbol{x}^i)$ and the increment is given by

$$\boldsymbol{x}^{i+1} = \boldsymbol{x}^i + \Delta\boldsymbol{x}^i.$$

The Jacobian matrix can either be calculated numerically or analytically. In regard to the analytical way, the problem arises that the one-dimensional prox function with the set $\mathbb{R}^+$ is indeed continuous but has a kink at the origin:

$$\operatorname*{prox}_{\mathbb{R}^+}(x) = \begin{cases} 0, & \text{for } x < 0, \\ x, & \text{for } x \geq 0. \end{cases} \tag{5.47}$$

Therefore, its derivative has a jump at zero and can there be set to 0 or 1:

$$\frac{\mathrm{d}}{\mathrm{d}x}\operatorname*{prox}_{\mathbb{R}^+}(x) = \begin{cases} 0, & \text{for } x < 0, \\ 1, & \text{for } x > 0. \end{cases} \tag{5.48}$$

5.2.6 Application to the element - sheave normal contact

The general spatial Maxwell contact is applied in the pushbelt CVT model to the element - sheave normal contact. This application is valid under the assumption that the deformation of the pulley-axle system is linear elastic. Thereby, the elements get coupled quasi-static in the contact by the elasticity of the sheave. In contrast to an elasto-dynamic model, no dynamic influence of the oscillation is considered. The influence of the sheaves is identical to that of the planar model [17]. The influence concerning the elements is new, as it becomes feasible only by the two contact points on each side of the element used in the spatial model.

Because of the principle of superposition, it is possible to analyse the response on the sheave resulting from the linear combination of simple point forces. In addition, the sheave is rotationally symmetric, so that the response to a rotated load is the rotated response to that load at the previous position around the same angle. The overall pulley axle system deformation is the combination of the sheave deformation and the sheave tilting because of axle and hub bending. The axial deformation can be expressed as [17]

$$w_i = {}_iC_j \cos(\delta_0)\lambda_j, \tag{5.49}$$

with the half wedge angle δ_0 projecting the normal force into the axial direction. The fixed and loose sheaves are different, as the tilting due to bending of the hub occurs only at the loose sheave, modelled by a rotational stiffness. The influence coefficient ${}_iC_j$ can be described by the product of two influence functions for azimuthal and radial direction, see [17]

$${}_iC_j = c_{rad}(\bar{r}_j) \cdot c_{az}(\Delta\phi_{ij}), \tag{5.50}$$

with the mean running radius $\bar{r}_j$ and the relative angle $\Delta\phi_{ij} = \phi_i - \phi_j$. The radial part is a polynomial function of degree m

$$c_{rad}(\bar{r}_j) = a_0 + a_1\bar{r}_j + a_2\bar{r}_j^2 + \cdots + a_m\bar{r}_j^m. \tag{5.51}$$

The azimuthal function is 2π-periodic because of the rotation symmetry and is approximated by a Fourier series

$$c_{az}(\Delta\phi_{ij}) = \sum_{k=0}^{n_k} A_k \cos\left(k\Delta\phi_{ij}\right). \tag{5.52}$$

Together, the influence coefficient ${}_iC_j$, which describes the deformation at $(\bar{r}_i, \phi_i)$ due to a load at $(\bar{r}_j, \phi_j)$, is the product of the polynomial and the Fourier series. As the elements in the pulley run in good approximation on a circular arc, the radii $\bar{r}_i$ are assumed to be constant with value $\bar{r}$:

$${}_iC_j = \left(a_0 + a_1\bar{r} + \cdots + a_m\bar{r}^m\right) \sum_{k=0}^{n_k} A_k \cos\left(k\Delta\phi_{ij}\right). \tag{5.53}$$

All the parameters are obtained by a finite element method analysis of the pulley-axle system. The overall influence matrix for n contact forces at different angles ϕ_j on a circular arc for one sheave satisfies (cf. [17])

$$\boldsymbol{C}_{sh} = c_{rad}(\bar{r}) \sum_{k=0}^{n_k} A_k \begin{bmatrix} \cos\left(k\underbrace{\Delta\phi_{11}}_{=0}\right) & \ldots & \cos\left(k\Delta\phi_{1n}\right) \\ \vdots & \ddots & \vdots \\ \cos\left(k\Delta\phi_{n1}\right) & \ldots & \cos\left(k\underbrace{\Delta\phi_{nn}}_{=0}\right) \end{bmatrix}. \tag{5.54}$$

In the spatial case a further element coupling is possible as there are two instead of one contact point on each element flank and the element can move in axial pulley direction. That means that the four contact points on the two flanks of the element (two left and two right) are all coupled through the element elasticity. Because of computing time reasons, the coupling of the right and left pulley through the element has not been investigated. However, the coupling of the two contacts (element rear and front) of one element flank has been analysed. The corresponding element influence matrix satisfies

$$\boldsymbol{C}_{el} = \frac{1}{c_{el}} \begin{bmatrix} 1 & 1 & 0 & & \cdots & & 0 \\ 1 & 1 & & & & & \\ 0 & & 1 & 1 & \ddots & & \vdots \\ & & 1 & 1 & & & \\ \vdots & & \ddots & & \ddots & & 0 \\ & & & & & 1 & 1 \\ 0 & & \cdots & & 0 & 1 & 1 \end{bmatrix}, \tag{5.55}$$

with the material stiffness of the element c_{el}. The 2×2 block matrices of ones show that at the two contact points of one element flank the same flexibility $1/c_{el}$ is assumed. However, other partitions of the element flexibility to the two contact points can be chosen. If no influence on the element flank is modelled, the matrix reduces to

$$\boldsymbol{C}_{el} = \frac{1}{c_{el}} \boldsymbol{E}. \tag{5.56}$$

The overall linear equation of one pulley including fixed (f) and loose (l) sheave for a coupling on the sheaves and one element flank is given by

$$\begin{pmatrix} \boldsymbol{g}_l \\ \boldsymbol{g}_f \end{pmatrix} = \left(\begin{bmatrix} \boldsymbol{C}_{sh,l} & 0 \\ 0 & \boldsymbol{C}_{sh,f} \end{bmatrix} + \begin{bmatrix} \boldsymbol{C}_{el} & 0 \\ 0 & \boldsymbol{C}_{el} \end{bmatrix} \right) \begin{pmatrix} \boldsymbol{\lambda}_l \\ \boldsymbol{\lambda}_f \end{pmatrix} + \begin{pmatrix} \tilde{\boldsymbol{g}}_l \\ \tilde{\boldsymbol{g}}_f \end{pmatrix} . \tag{5.57}$$

6 Model Reduction

As the computing time is a big issue in [45], different strategies have been applied to reduce the model. A hybrid (planar - spatial) CVT model has been developed which covers the planar phenomena with a much lower computing time, cf. Chapter 7. For this hybrid model, a planar Cosserat rod model has been derived. In addition, nonlinear model order reduction techniques are used to truncate high numerical frequencies of the Cosserat rod model and allow for larger time step sizes during the integration.

6.1 Hybrid pushbelt CVT model

A new hybrid model (also called planar model in the following) based on [17, 45] has been modelled and implemented inside the software framework MBSim. It is an extended planar model as it consists of both planar and spatial bodies. The main advantage of the hybrid model is a significant reduction of the computing time, with a factor of about nine, compared to the spatial model. The hybrid model has been integrated into the framework of the spatial pushbelt CVT model to enable the possibility to switch between a planar or spatial simulation. Only the differences to the spatial model (as summarised in Section 3.2) and not the entire planar model is explained in this section subdivided into bodies, interactions and initialisation. The plane of motion is the x-y-plane, in the following also called in-plane.

6.1.1 Bodies

Similar to the spatial model, the hybrid model is built with the three different bodies - elements, ring sets and pulley sheaves.

Elements

The elements in the planar model have 3 rigid DOFs for the plane motion.

Ring sets

The ring set is modelled with the planar redundant coordinate beam model [59]. It is also based on the co-rotational approach and is able to describe large planar deformations.

The global coordinate vector of one finite element with two nodes left and right reduces to

$$\boldsymbol{q}_g = \left(x_L, y_L, \varphi_L, \quad c_{L_2}, c_{R_2}, \quad x_R, y_R, \varphi_R\right)^T. \tag{6.1}$$

The transformation between the internal $\boldsymbol{q}_i$ and global $\boldsymbol{q}_g$ coordinates can be evaluated in an analytic way [59]

$$\boldsymbol{q}_i = \boldsymbol{f}\left(\boldsymbol{q}_g\right). \tag{6.2}$$

No nonlinear system has to be solved numerically. Hence, the time step size is not restricted by the internal transformation as in the spatial case. Thus, a larger number of finite elements than in the spatial case can be used to describe the ring sets more accurately.

As the pushbelt can move only in the plane of motion, one single ring set is chosen for the planar model. This ring set with the double width $2\tilde{w}_r$ - of the spatial ring set - is placed in the middle of the elements, cf. Figure 6.1. The in-plane area moment of inertia is adapted with the double width to

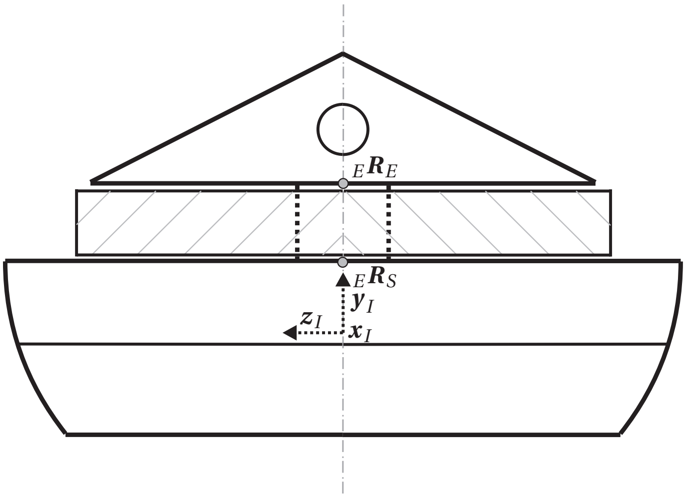

Figure 6.1: Planar centred ring set with double width

$$\tilde{I}_1 = \frac{2\tilde{w}_R \tilde{h}_R^3}{12\tilde{N}_R}. \tag{6.3}$$

Pulleys

As the planar pushbelt cannot move in the axial pulley direction, the same approach as in the spatial model with fixed and loose sheave is not possible. As in case of shifting, starting with an element on both sides in contact with the pulley sheaves, the contact on the fixed sheave would either detach or prevent the transmission change. In the first case, if the distance of the loose sheave decreases and the element is pushed to a larger running radius, the contact on the fixed sheave detaches. In the second case, if the distance of the loose sheave increases, the element stays in contact on the fixed sheave which would prevent the planar pushbelt of decreasing its running radius. The planar pushbelt cannot be pushed onto the fixed sheave and the clamping force of the loose sheave is not transferred by the belt from the loose to the fixed sheave.

To solve this problem, either only one sheave or two symmetric sheaves for one pulley are possible which both lead to different assumptions and solutions. In this study it has been chosen to model both sheaves of one pulley as two symmetric loose sheaves. Hence, both have the four DOFs for tilting, rotating and axial movement. They always move symmetrically with respect to the x-y-plane, i.e. when one sheave decreases the sheave distance, the other moves also towards it and vice versa, cf. Figure 6.2. Hence, the element-pulley contact is symmetrical on both sides of the element. In the chosen approach, the sheaves are modelled as full spatial bodies and thus, the overall model is a combination of the planar and the spatial model and therefore called hybrid model.

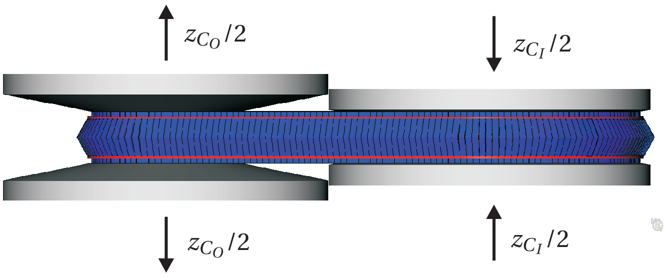

Figure 6.2: Two symmetric sheaves in the hybrid model

6.1.2 Interactions

For the planar case, the interactions of [45] have been simplified in a natural manner similar to [17].

Element - element contacts

The contacts at element top and bottom simplify to point - line contacts. At the rocking edge one circular arc (in the x-y-plane) is in contact with the line of the front element. For the pin-hole contact only three point - line contacts are necessary according to [17]. This contact is visualised in Figure 6.3. The three direction matrices of the contour

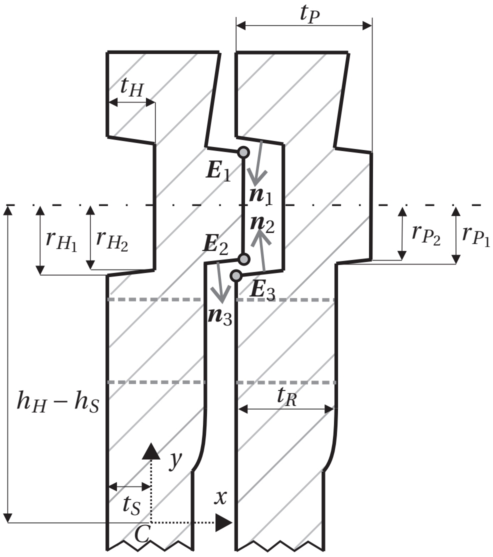

Figure 6.3: Planar element - element pin-hole contact

lines (including outward pointing normal, tangent and binormal) of one element in the element coordinate system are given by

$$\boldsymbol{A}(\phi_i) = (\boldsymbol{n}_i,\, \boldsymbol{t}_i,\, \boldsymbol{b}) = \begin{pmatrix} \cos(\phi_i) & -\sin(\phi_i) & 0 \\ \sin(\phi_i) & \cos(\phi_i) & 0 \\ 0 & 0 & 1 \end{pmatrix}, \quad i = 1,2,3 \tag{6.4}$$

with the three angles

$$\phi_1 = \frac{3\pi}{2} - \arctan\left(\frac{r_{H_1} - r_{H_2}}{t_H}\right), \tag{6.5}$$

$$\phi_2 = \frac{\pi}{2} + \arctan\left(\frac{r_{H_1} - r_{H_2}}{t_H}\right), \tag{6.6}$$

$$\phi_3 = -\frac{\pi}{2} + \arctan\left(\frac{r_{P_1} - r_{P_2}}{t_P - t_R}\right). \tag{6.7}$$

The corresponding points $\boldsymbol{E}_1$, $\boldsymbol{E}_2$ and $\boldsymbol{E}_3$ of one element are obtained from its geometry

$$\boldsymbol{E}_1 = \begin{pmatrix} t_P - t_S \\ (h_H - h_S) + r_{P_2} \\ 0 \end{pmatrix}, \qquad \boldsymbol{E}_2 = \begin{pmatrix} t_P - t_S \\ (h_H - h_S) - r_{P_2} \\ 0 \end{pmatrix}, \tag{6.8}$$

$$\boldsymbol{E}_3 = \begin{pmatrix} -t_S \\ (h_H - h_S) - r_{H_1} \\ 0 \end{pmatrix}, \tag{6.9}$$

with h_H denoting the height from bottom to the dotted line in the middle of the pin. The positions of the contact points at element top and bottom remain. For the rocking edge only one circular arc in the plane of motion is used. Thus, the rear side of the predecessor element is modelled by a line and not a plane. The contact points are chosen to be unilateral with a flexible force law.

Element - ring set contacts

Only one point (${}_E\boldsymbol{R}_S$) is required for the bilateral and two points (${}_E\boldsymbol{R}_S$ and ${}_E\boldsymbol{R}_E$) for the unilateral element - ring set contacts, cf. Figure 6.1

$$ {}_E\boldsymbol{R}_S = \begin{pmatrix} t_R/2 - t_S \\ h_P - h_S \\ 0 \end{pmatrix}, \qquad {}_E\boldsymbol{R}_E = \begin{pmatrix} t_R/2 - t_S \\ h_E - h_S \\ 0 \end{pmatrix}. \tag{6.10} $$

The lateral movement of the ring set is not possible in the planar case. Hence, no contact restriction in lateral direction is required. A friction law is applied in longitudinal direction.

Element - pulley contacts

As the pulley sheaves are full spatial bodies, also the contour is modelled spatial with a frustum contour. For the element - pulley contacts either the full spatial contact of the model [45] or a simplified point - frustum contact can be used. Both options are depicted in Figure 6.4. The extended contact is modelled with two circle - frustum contacts on each flank. In the simplified contact, only one fixed contact point $\boldsymbol{P}_R$ per element flank is in contact with the frustum contour of the sheave. With this approach the contact position on the element does not have to be calculated in each time step. The simplified contact is also applicable in the spatial model. The positions of the fixed contact points on the element flanks are chosen according to [17].

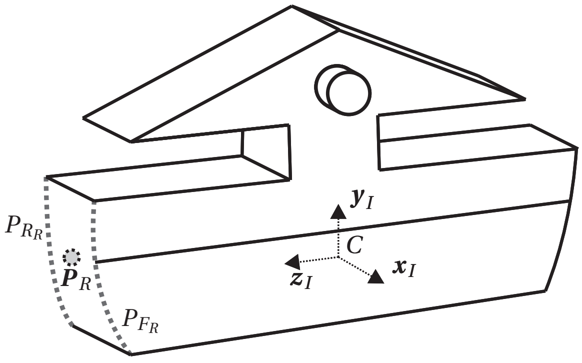

Figure 6.4: Extended or simplified element - pulley contact

Regarding the contact law in normal direction, either the decoupled law of [45] or the coupled regularised law explained in Section 5.2 can be applied in combination with a regularised spatial friction law.

6.1.3 Initialisation

The initialisation process described in Subsection 3.2.3 and Chapter 4 is used for the planar model. The ring set is initialised according to the Sattler model [44] and the elements are placed on the ring set. The pulleys adapt according to the given transmission ratio.

Ring sets

The planar DOFs of the ring set are extracted from the spatial initialisation according to Chapter 4. The entire band distance $\tilde{l}_r$ of the planar ring set is slightly shorter than of the spatial ring sets as the belt deflection (in z-direction) is neglected.

Elements

The elements are initialised according to the spatial model with only the plane DOFs. Hereby, the arc length of the neutral fibre of the ring set where the element should be positioned is calculated heuristically to distribute the elements over the whole length. Then, the position of the element's centre of gravity is gained from this position of the neutral fibre of the ring set ${}_I\boldsymbol{r}_O$ and a fixed vector between both of them ${}_E\boldsymbol{r}_{O,S}$ given in the elements frame E

$$ {}_I\boldsymbol{r}_S = {}_I\boldsymbol{r}_O + {}_{IE}\boldsymbol{A}\;{}_E\boldsymbol{r}_{O,S}\,. \tag{6.11} $$

The element's velocity is gained by the velocity of the ring package by

$$ {}_I\boldsymbol{v}_S = {}_I\boldsymbol{v}_O + {}_{IE}\mathring{\boldsymbol{A}}\,{}_E\boldsymbol{r}_{O,S} + {}_{IE}\boldsymbol{A}\,{}_E\mathring{\boldsymbol{r}}_{O,S} = {}_I\boldsymbol{v}_O + {}_{IE}\boldsymbol{\omega} \times {}_{IE}\boldsymbol{A}\,{}_E\boldsymbol{r}_{O,S}\,. \tag{6.12} $$

Pulleys

The initial positions of the centres of gravity of the sheaves have to be determined. In the spatial model [45] the two fixed sheaves have a fixed position and the loose sheave positions are depending on the transmission ratio and the curved element geometry. The positions for the planar initialisation is done symmetrically for both sheaves. Thus, the z-distance of two pulley sheaves for the spatial case is calculated and divided into two halves for each sheave in the planar model. The initial sheave positions satisfy

$$_I\boldsymbol{r}_{I_*} = \begin{pmatrix} d_A \\ 0 \\ \pm\frac{|z_{I_L}-z_{I_F}|}{2} \end{pmatrix}, \qquad _I\boldsymbol{r}_{O_*} = \begin{pmatrix} 0 \\ 0 \\ \pm\frac{|z_{O_L}-z_{O_F}|}{2} \end{pmatrix}. \tag{6.13}$$

The z-positions $z_{I_L}, z_{I_F}, z_{O_L}, z_{O_F}$ of the four sheaves at primary and secondary pulley (each time loose and fixed) are calculated as in the spatial model.

Pulley - Environment

Because of the symmetric sheave concept, the boundary settings have to be adapted. The kinematic clamping force $F_{C_{I/O}}$ is applied on both sheaves of one pulley. The half clamping distance and velocity than in the spatial model is applied for the end stop, because both sheaves of one pulley move, cf. Figure 6.2.

6.2 Planar Cosserat rod model

A fast and accurate rod model discretised with finite differences has been presented in [28]. This presentation of a geometrically exact spatial Cosserat rod model was decisive to try another rod model for the ring sets in the CVT model. As the step size of the spatial RCM beam model in [45] is restricted by the internal transformation between the two coordinate systems, this model was promising to solve this problem. The theory and implementation of a spatial Cosserat rod model in *MBSim* has been done in a joint work with Thorsten Schindler [10] resulting out of the supervised term paper [27]. The spatial Cosserat rod model is not presented here, as it would go beyond the scope of this study. Nevertheless, the planar Cosserat rod model is shown in the following which has been derived out of the spatial model [10] in the supervised diploma thesis [56]. Only the closed structure is presented which is relevant for the application in the CVT. The $\boldsymbol{t}$-$\boldsymbol{n}$-plane is chosen as the plane of motion. The contour of the spatial case is used also for the planar rod. The basis for this section is found in [28], however, many changes have been made in this derivation. For the industrial application of a pushbelt CVT which nearly runs in-plane, the quaternionic parameterisation for the rotation is not required as the singularity does not occur. Hence, a Cardan parameterisation was chosen which avoids additional constraints. A closed structure has been introduced. A NURBS contour description was implemented for the rod to enable interactions of the ring sets and the elements. For the assembling in the object-oriented framework *MBSim* a finite element description has been applied for the discretised beam segments. Parts of the text of this section are taken from the joint paper [10].

6.2.1 Continuous equations of motion

In this subsection, the energy terms in the continuous case are shown briefly according to [28] for the spatial case. The transfer to the planar case can easily be done out of this. For a full description of the continuous case see [28], where in contrast unit quaternions are used for the parameterisation of the rotation.

A rod is a slender body considered as a one dimensional continuum which is much larger in one direction than in the other two directions. The motion of the rod is described by means of the Lagrange description. The Lagrange parameter $s \in [0, L]$ refers to the undeformed length of the neutral fibre of the rod L. Two fields in inertial description depending on the time t and the coordinate s are introduced for the kinematics of the flexible body. Both are unit speed curves concerning the Lagrange parameter s. The position field

$$(s,t) \mapsto {}_I\boldsymbol{r}(s,t) = \begin{pmatrix} x(s,t) \\ y(s,t) \\ z(s,t) \end{pmatrix} \in \mathbb{R}^3 \tag{6.14}$$

describes the spatial motion of the centre line. The rotation field parametrised with Cardan angles

$$(s,t) \mapsto \boldsymbol{\varphi}(s,t) = \begin{pmatrix} \alpha(s,t) \\ \beta(s,t) \\ \gamma(s,t) \end{pmatrix} \in \mathbb{R}^3 \tag{6.15}$$

defines the spatial orientation of a body-fixed frame K with respect to the inertial frame I. The rotation matrix between the two coordinate systems is associated with the tangent, normal and binormal of the centre line given in the inertial system. It is the result of three successive rotations [38]

$$\begin{aligned} \boldsymbol{\varphi} \mapsto {}_{IK}\boldsymbol{A}(\boldsymbol{\varphi}) &:= \left({}_I\boldsymbol{t}(\boldsymbol{\varphi}), {}_I\boldsymbol{n}(\boldsymbol{\varphi}), {}_I\boldsymbol{b}(\boldsymbol{\varphi})\right) \\ &= \begin{pmatrix} \cos\beta\cos\gamma & -\cos\beta\sin\gamma & \sin\beta \\ \cos\alpha\sin\gamma + \sin\alpha\sin\beta\cos\gamma & \cos\alpha\cos\gamma - \sin\alpha\sin\beta\sin\gamma & -\sin\alpha\cos\beta \\ \sin\alpha\sin\gamma - \cos\alpha\sin\beta\cos\gamma & \sin\alpha\cos\gamma + \cos\alpha\sin\beta\sin\gamma & \cos\alpha\cos\beta \end{pmatrix}. \end{aligned} \tag{6.16}$$

The vectors $\boldsymbol{n}$ and $\boldsymbol{b}$ span the cross-section area of the rod. The relationship between the time derivative of position and angles as well as velocity $\boldsymbol{v} \in \mathbb{R}^3$ and angular velocity $\boldsymbol{\omega} \in \mathbb{R}^3$ is given by

$$\begin{pmatrix} {}_I\dot{\boldsymbol{r}} \\ \dot{\boldsymbol{\varphi}} \end{pmatrix} = \begin{pmatrix} \boldsymbol{E} & \boldsymbol{0} \\ \boldsymbol{0} & {}_I\boldsymbol{Y} \end{pmatrix} \begin{pmatrix} {}_I\boldsymbol{v} \\ {}_I\boldsymbol{\omega} \end{pmatrix}, \tag{6.17}$$

with the unity matrix $\boldsymbol{E} \in \mathbb{R}^{3\times 3}$ and the matrix $\boldsymbol{Y} \in \mathbb{R}^{3\times 3}$ whose inverse is shown below.

The angular velocity vector in the inertial coordinate system is gained from the skew symmetric matrix

$$ {}_I\tilde{\boldsymbol{\omega}} = {}_{IK}\dot{\boldsymbol{A}}\,{}_{IK}\boldsymbol{A}^T \tag{6.18}$$

in the following form

$$ {}_I\boldsymbol{\omega} = {}_I\boldsymbol{Y}^{-1}\dot{\boldsymbol{\varphi}} = \begin{pmatrix} {}_It_2\dfrac{\partial\, {}_It_3}{\partial \boldsymbol{\varphi}} + {}_In_2\dfrac{\partial\, {}_In_3}{\partial \boldsymbol{\varphi}} + {}_Ib_2\dfrac{\partial\, {}_Ib_3}{\partial \boldsymbol{\varphi}} \\ {}_It_3\dfrac{\partial\, {}_It_1}{\partial \boldsymbol{\varphi}} + {}_In_3\dfrac{\partial\, {}_In_1}{\partial \boldsymbol{\varphi}} + {}_Ib_3\dfrac{\partial\, {}_Ib_1}{\partial \boldsymbol{\varphi}} \\ {}_It_1\dfrac{\partial\, {}_It_2}{\partial \boldsymbol{\varphi}} + {}_In_1\dfrac{\partial\, {}_In_2}{\partial \boldsymbol{\varphi}} + {}_Ib_1\dfrac{\partial\, {}_Ib_2}{\partial \boldsymbol{\varphi}} \end{pmatrix} \dot{\boldsymbol{\varphi}}, \tag{6.19}$$

for an arbitrary angle parameterisation.

Potential energies

The strain, curvature and gravitational energy form the potential energies.

Strain energy The Cosserat beam includes shear compared to the Kirchhoff beam theory. The spatial strain vector is modelled by the difference of the first derivative with respect to the arc length of the curve and the tangent. In the inertial frame I, it is given by

$$ {}_I\boldsymbol{\varepsilon} = \frac{\partial\, {}_I\boldsymbol{r}}{\partial s} - {}_I\boldsymbol{t}\,. \tag{6.20}$$

Transformed to the material or body-fixed frame K, it has the form

$$ {}_K\boldsymbol{\varepsilon} = {}_{IK}\boldsymbol{A}^T\,\frac{\partial\, {}_I\boldsymbol{r}}{\partial s} - \begin{pmatrix} 1 \\ 0 \\ 0 \end{pmatrix}. \tag{6.21}$$

Due to the choice of the columns of the rotation matrix in (6.16), the first unit vector has to be subtracted in (6.21). For interpretation, e.g. the elongation in the material system is calculated to

$$ \varepsilon_1 = {}_I\boldsymbol{t}^T\,{}_I\boldsymbol{r}' - 1. \tag{6.22}$$

Thus, for the arrangement of the constitutive values, the stiffness EA is in the first diagonal element of the material matrix

$$ \boldsymbol{C}^{\boldsymbol{\varepsilon}} = \begin{pmatrix} EA & & \\ & G\sigma_1 A & \\ & & G\sigma_2 A \end{pmatrix}. \tag{6.23}$$

The appearing parameters are Young's modulus E, the shear modulus G, the cross-section area A and the shear corrections $0 < \sigma_1, \sigma_2 < 1$. The strain energy with strain vector in the body-fixed system is given by

$$V_{SE} = \frac{1}{2} \int_0^L {}_K\boldsymbol{\varepsilon}^T \boldsymbol{C}^{\boldsymbol{\varepsilon}} {}_K\boldsymbol{\varepsilon} \, \mathrm{d}s. \tag{6.24}$$

Curvature energy To derive the curvature vector, a skew symmetric matrix resulting from the rotation matrix is required. For every rotation matrix it holds

$${}_{IK}\boldsymbol{A}^T {}_{IK}\boldsymbol{A} = \boldsymbol{0}. \tag{6.25}$$

Therefore, the derivative of (6.25) with respect to s

$${}_{IK}\boldsymbol{A}^T {}_{IK}\boldsymbol{A}' + ({}_{IK}\boldsymbol{A}^T {}_{IK}\boldsymbol{A}')^T = \boldsymbol{0}, \tag{6.26}$$

yields a skew symmetric matrix by the product rule. This matrix is interpreted as the tilde matrix $\widetilde{\boldsymbol{\kappa}}$ of the curvature vector $\boldsymbol{\kappa}$

$${}_K\widetilde{\boldsymbol{\kappa}} = {}_{IK}\boldsymbol{A}^T {}_{IK}\boldsymbol{A}' = -({}_{IK}\boldsymbol{A}^T {}_{IK}\boldsymbol{A}')^T. \tag{6.27}$$

The curvature vector can be extracted of ${}_K\widetilde{\boldsymbol{\kappa}}$:

$${}_K\boldsymbol{\kappa}_n = \begin{pmatrix} {}_I\boldsymbol{b}^T {}_I\boldsymbol{n}' \\ {}_I\boldsymbol{t}^T {}_I\boldsymbol{b}' \\ {}_I\boldsymbol{n}^T {}_I\boldsymbol{t}' \end{pmatrix}. \tag{6.28}$$

The corresponding constitutive matrix $\boldsymbol{C}^{\boldsymbol{\kappa}}$ has the form

$$\boldsymbol{C}^{\boldsymbol{\kappa}} = \begin{pmatrix} GI_0 & & \\ & EI_1 & \\ & & EI_2 \end{pmatrix} \tag{6.29}$$

with the polar moment of inertia $I_0 = I_1 + I_2$ around the torsional axis and the area moments of inertia I_1 in $\boldsymbol{t}-\boldsymbol{b}-$plane and I_2 in $\boldsymbol{t}-\boldsymbol{n}-$plane. Finally, the curvature energy has the form

$$V_{BT} = \frac{1}{2} \int_0^L {}_K\boldsymbol{\kappa}^T \boldsymbol{C}^{\boldsymbol{\kappa}} {}_K\boldsymbol{\kappa} \, \mathrm{d}s. \tag{6.30}$$

Gravitational energy The last potential energy, the gravitational energy, is calculated straightforward to

$$V_G = -\rho A \, {}_I\boldsymbol{g}^T \int_0^L {}_I\boldsymbol{r} \, \mathrm{d}s. \tag{6.31}$$

The parameters are the density ρ and the gravitational vector $\boldsymbol{g}$.

Kinetic energies

The kinetic energy is divided into the translatory and rotatory part.

Translatory kinetic energy The translatory kinetic energy satisfies

$$T_T = \frac{\rho A}{2} \int_0^L \| {}_I\dot{\boldsymbol{r}} \|^2 \, \mathrm{d}s. \tag{6.32}$$

Rotatory kinetic energy The derivative of (6.25) with respect to the time t yields a skew symmetric matrix. This is interpreted as the tilde matrix of the material angular velocity

$${}_K\widetilde{\boldsymbol{\omega}} = {}_{IK}\boldsymbol{A}^T \, {}_{IK}\dot{\boldsymbol{A}} = -({}_{IK}\boldsymbol{A}^T \, {}_{IK}\dot{\boldsymbol{A}})^T. \tag{6.33}$$

The material angular velocity has the form

$${}_K\boldsymbol{\omega} = \begin{pmatrix} {}_I\boldsymbol{b}^T \, {}_I\dot{\boldsymbol{n}} \\ {}_I\boldsymbol{t}^T \, {}_I\dot{\boldsymbol{b}} \\ {}_I\boldsymbol{n}^T \, {}_I\dot{\boldsymbol{t}} \end{pmatrix}. \tag{6.34}$$

The corresponding inertia tensor is constant for the material angular velocity and is given by

$$\boldsymbol{I} = \begin{pmatrix} I_0 & & \\ & I_1 & \\ & & I_2 \end{pmatrix}. \tag{6.35}$$

Finally, the rotatory kinetic energy is calculated as

$$T_R = \frac{\rho}{2} \int_0^L {}_K\boldsymbol{\omega}^T \boldsymbol{I} \, {}_K\boldsymbol{\omega} \, \mathrm{d}s. \tag{6.36}$$

Strain dissipation

The strain dissipation is introduced to damp the strains as the stiff DOFs according to [28]

$$D_{SE} = \int_0^L {}_K\dot{\boldsymbol{\varepsilon}}^T \boldsymbol{C}^{\dot{\varepsilon}} {}_K\dot{\boldsymbol{\varepsilon}} \, \mathrm{d}s. \tag{6.37}$$

The corresponding material damping matrix is given by

$$_K\boldsymbol{C}_D^{\boldsymbol{\varepsilon}} = \begin{pmatrix} c_{0D}^{\boldsymbol{\varepsilon}} & & \\ & c_{1D}^{\boldsymbol{\varepsilon}} & \\ & & c_{2D}^{\boldsymbol{\varepsilon}} \end{pmatrix}, \tag{6.38}$$

with the shear damping parameters $c_{0D}^{\boldsymbol{\varepsilon}}, c_{1D}^{\boldsymbol{\varepsilon}}, c_{2D}^{\boldsymbol{\varepsilon}}$.

6.2.2 Discrete equations of motion

For the discretisation of the equations of motion a staggered grid

$$0 = s_0 < s_{\frac{1}{2}} < s_1 < \ldots < s_{N-1} < s_{N-\frac{1}{2}} < s_N = L \tag{6.39}$$

as in [28] is applied with vertices s_n and midpoints $s_{n-\frac{1}{2}} = \frac{s_{n-1}+s_n}{2}$. The two main reasons to choose a staggered grid are the required finite difference approximations of the derivatives with respect to s and the interpretation of the variables (like strain and curvature vector) for the energy expressions, see later in this subsection. For the evaluation of the internal dynamics, only the discrete degrees of freedom (DOFs) at these points are required. The discrete DOFs of the elements reduce to the three degrees for the plane motion. The inertial positions are given by

$$_I\boldsymbol{r}_n(t) = \begin{pmatrix} x(s_n, t) \\ y(s_n, t) \end{pmatrix} \in \mathrm{I\!R}^2, \tag{6.40}$$

and are positioned at the vertices, cf. Figure 6.5. The rotation about the binormal vector $\boldsymbol{b}$ is described by the inertial Cardan angle at the midpoints

$$\gamma_{n-\frac{1}{2}}(t) = \gamma(s_{n-\frac{1}{2}}, t) \in \mathrm{I\!R}. \tag{6.41}$$

The discrete rotation matrix (around the vector $\boldsymbol{b}$) for the planar case yields

$$_{IK}\boldsymbol{A}_{n-\frac{1}{2}} = \begin{pmatrix} _I\boldsymbol{t}_{n-\frac{1}{2}}, & _I\boldsymbol{n}_{n-\frac{1}{2}} \end{pmatrix} = \begin{pmatrix} \cos(\gamma_{n-\frac{1}{2}}) & -\sin(\gamma_{n-\frac{1}{2}}) \\ \sin(\gamma_{n-\frac{1}{2}}) & \cos(\gamma_{n-\frac{1}{2}}) \end{pmatrix}. \tag{6.42}$$

It depends on the angles located at the midpoints. Two different staggered element types are introduced for the evaluation of the energies. One translation element consists of five DOFs

$$\boldsymbol{q}_{el,tr,n} = \begin{pmatrix} {}_I\boldsymbol{r}_{n-1} \\ \gamma_{n-\frac{1}{2}} \\ {}_I\boldsymbol{r}_n \end{pmatrix}, \tag{6.43}$$

and describes potential strain and gravitational energy, translatory and rotatory kinetic energy as well as strain dissipation. One rotation element has four DOFs

$$\boldsymbol{q}_{el,ro,n} = \begin{pmatrix} \gamma_{n-\frac{1}{2}} \\ {}_I\boldsymbol{r}_n \\ \gamma_{n+\frac{1}{2}} \end{pmatrix}, \tag{6.44}$$

cf. Figure 6.5. It is used once only for the potential curvature energy.

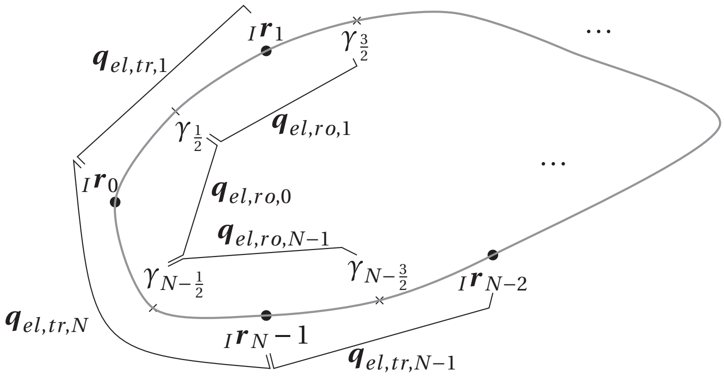

Figure 6.5: Translation and rotation elements in a closed structure [10]

The overall vector of the discrete DOFs for the closed structure ($\boldsymbol{r}_N = \boldsymbol{r}_0$) is given by

$$\boldsymbol{q}^T = \left({}_I\boldsymbol{r}_0^T, \quad \gamma_{\frac{1}{2}}, \quad \ldots, \quad {}_I\boldsymbol{r}_{N-1}^T, \quad \gamma_{N-\frac{1}{2}} \right). \tag{6.45}$$

The position at the Lagrange parameter L, ${}_I\boldsymbol{r}_N$, is not part of the vector as it is equal to the starting position ${}_I\boldsymbol{r}_0$ because of the closing condition. Due to the staggered grid, two different weight factors occur for the approximation of the energy expressions corresponding to two quadrature rules. For the midpoint rule it is the arc length of the n-th translation element

$$\Delta s_{n-\frac{1}{2}} := s_n - s_{n-1}. \tag{6.46}$$

For the trapezoidal rule it is the arc length of the n-th rotation element

$$\delta s_n := s_{n+\frac{1}{2}} - s_{n-\frac{1}{2}}, \tag{6.47}$$

with the exception of the first and last weight factor which are constructed different

$$\delta s_0 := s_{\frac{1}{2}},\ \delta s_N := L - s_{N-\frac{1}{2}}. \tag{6.48}$$

The discrete equations of motion are gained by Hamilton's principle according to Section 2.5. The corresponding discrete energy expressions are derived in the following.

Discrete potential energies

The potential energies are the strain, curvature and gravitational energies.

Discrete strain energy In the planar case, only extension and shearing in normal direction remain. The discrete strains are situated on the midpoints between two positions, as they are a measure of the deformations. Thus, the discrete strain energy is approximated by the midpoint rule to

$$V_{SE} = \frac{1}{2}\sum_{n=1}^{N} \Delta s_{n-\frac{1}{2}}\, {}_K\boldsymbol{\varepsilon}^T_{n-\frac{1}{2}} \begin{pmatrix} EA & 0 \\ 0 & G\sigma A \end{pmatrix} {}_K\boldsymbol{\varepsilon}_{n-\frac{1}{2}} = \sum_{n=1}^{N} V_{SE,el,n}, \tag{6.49}$$

with the material strain vector

$${}_K\boldsymbol{\varepsilon}_{n-\frac{1}{2}} = {}_{IK}\boldsymbol{A}^T_{n-\frac{1}{2}} \frac{{}_I\Delta\boldsymbol{r}_{n-\frac{1}{2}}}{\Delta s_{n-\frac{1}{2}}} - \begin{pmatrix} 1 \\ 0 \end{pmatrix}. \tag{6.50}$$

It is approximated by a finite difference of first order with the abbreviation

$${}_I\Delta\boldsymbol{r}_{n-\frac{1}{2}} := {}_I\boldsymbol{r}_n - {}_I\boldsymbol{r}_{n-1}. \tag{6.51}$$

Like in the finite elements theory, the energies are expressed in element energy terms. The n-th energy element depends on the translation element and reduces to

$$V_{SE,el,n}(\boldsymbol{q}_{el,tr,n}) = \frac{1}{2\Delta s_{n-\frac{1}{2}}} \left[EA\left({}_I\boldsymbol{t}^T_{n-\frac{1}{2}}\, {}_I\Delta\boldsymbol{r}_{n-\frac{1}{2}} - \Delta s_{n-\frac{1}{2}} \right)^2 + G\sigma A \left({}_I\boldsymbol{n}^T_{n-\frac{1}{2}}\, {}_I\Delta\boldsymbol{r}_{n-\frac{1}{2}} \right)^2 \right]. \tag{6.52}$$

The contribution to the equations of motion of the strain energy satisfies

$$
\begin{aligned}
\frac{\partial V_{SE}}{\partial \boldsymbol{q}_{el,tr,n}} = \frac{1}{\Delta s_{n-1}} \Bigg\{ & EA\left[{}_I\boldsymbol{t}^T_{n-\frac{1}{2}}\,{}_I\Delta\boldsymbol{r}_{n-\frac{1}{2}} - \Delta s_{n-\frac{1}{2}}\right]\left(-{}_I\boldsymbol{t}^T_{n-\frac{1}{2}}, {}_I\Delta\boldsymbol{r}^T_{n-\frac{1}{2}}\frac{\mathrm{d}\,{}_I\boldsymbol{t}_{n-\frac{1}{2}}}{\mathrm{d}\gamma_{n-\frac{1}{2}}}, {}_I\boldsymbol{t}^T_{n-\frac{1}{2}}\right) \\
& + G\sigma A\left[{}_I\boldsymbol{n}^T_{n-\frac{1}{2}}\,{}_I\Delta\boldsymbol{r}_{n-\frac{1}{2}}\right]\left(-{}_I\boldsymbol{n}^T_{n-\frac{1}{2}}, {}_I\Delta\boldsymbol{r}^T_{n-\frac{1}{2}}\frac{\mathrm{d}\,{}_I\boldsymbol{n}_{n-\frac{1}{2}}}{\mathrm{d}\gamma_{n-\frac{1}{2}}}, {}_I\boldsymbol{n}^T_{n-\frac{1}{2}}\right)\Bigg\},
\end{aligned}
\tag{6.53}
$$

with the derivatives

$$
\frac{\mathrm{d}\,{}_I\boldsymbol{t}_{n-\frac{1}{2}}}{\mathrm{d}\gamma_{n-\frac{1}{2}}} = \begin{pmatrix} -\sin(\gamma_{n-\frac{1}{2}}) \\ \cos(\gamma_{n-\frac{1}{2}}) \end{pmatrix},
\tag{6.54}
$$

and

$$
\frac{\mathrm{d}\,{}_I\boldsymbol{n}_{n-\frac{1}{2}}}{\mathrm{d}\gamma_{n-\frac{1}{2}}} = \begin{pmatrix} -\cos(\gamma_{n-\frac{1}{2}}) \\ -\sin(\gamma_{n-\frac{1}{2}}) \end{pmatrix}.
\tag{6.55}
$$

Discrete curvature energy The planar curvature energy reduces significantly as only bending in the $\boldsymbol{t}$-$\boldsymbol{n}$-plane remains. As bending considers the rotation between two different frames, the discrete curvature is situated in the middle of two rotation matrices on the vertices of the staggered grid. The discrete curvature energy is given by

$$
V_{BT} = \frac{1}{2}\sum_{n=0}^{N} \delta s_n\, {}_K\widehat{\kappa}^T_n\, EI\, {}_K\widehat{\kappa}_n = \sum_{n=0}^{N} V_{BT,el,n},
\tag{6.56}
$$

The integral is approximated by means of the trapezoidal rule because the curvatures are given at the vertices. The Cardan angles required at the vertices are gained by interpolation

$$
\widehat{\gamma}_n = \frac{1}{2}\left[\gamma_{n-\frac{1}{2}} + \gamma_{n+\frac{1}{2}}\right],
\tag{6.57}
$$

and the finite difference satisfies

$$
\widehat{\gamma}'_n = \frac{1}{\delta s_n}\left[\gamma_{n+\frac{1}{2}} - \gamma_{n-\frac{1}{2}}\right].
\tag{6.58}
$$

The interpolated curvature simplifies to

$$
\widehat{\kappa}_n = {}_I\boldsymbol{n}^T_n\,{}_I\boldsymbol{t}'_n = {}_I\boldsymbol{n}^T_n(\widehat{\gamma}_n)\frac{\mathrm{d}\,{}_I\boldsymbol{t}}{\mathrm{d}\gamma}(\widehat{\gamma}_n)\widehat{\gamma}'_n = \begin{pmatrix} -\sin(\widehat{\gamma}_n) \\ \cos(\widehat{\gamma}_n) \end{pmatrix}^T \begin{pmatrix} -\sin(\widehat{\gamma}_n) \\ \cos(\widehat{\gamma}_n) \end{pmatrix}\widehat{\gamma}'_n = \widehat{\gamma}'_n.
\tag{6.59}
$$

The n-th curvature energy element, depending only on the rotational element has the form

$$V_{BT,el,n}(\boldsymbol{q}_{el,ro,n}) = \frac{1}{2}\delta s_n EI\left(\widehat{\kappa}_n - \kappa^0\right)^2, \tag{6.60}$$

with the precurvature κ^0. The contribution to the equations of motion is given by

$$\frac{\partial V_{BT,el,n}}{\partial \boldsymbol{q}_{el,ro,n}} = \delta s_n \left[EI(\widehat{\kappa}_n - \kappa^0)\frac{\partial \widehat{\kappa}_n}{\partial \boldsymbol{q}_{el,ro,n}} \right] = EI(\widehat{\gamma}'_n - \kappa^0)\begin{pmatrix}-1, & 0, & 0, & 1\end{pmatrix}. \tag{6.61}$$

Hereby, the following equation has been used

$$\frac{\partial \widehat{\kappa}_n}{\partial \boldsymbol{q}_{el,ro,n}} = \begin{pmatrix} \dfrac{\partial \widehat{\gamma}'_n}{\partial \gamma_{n-\frac{1}{2}}}, & \dfrac{\partial \widehat{\gamma}'_n}{\partial \boldsymbol{r}_n}, & \dfrac{\partial \widehat{\gamma}'_n}{\partial \gamma_{n+\frac{1}{2}}} \end{pmatrix} = \frac{1}{\delta s_n}\begin{pmatrix}-1, & 0, & 0, & 1\end{pmatrix}. \tag{6.62}$$

Discrete gravitational energy The discrete gravitational energy is approximated by means of the trapezoidal rule to

$$V_G = -\rho A\, {}_I\boldsymbol{g}^T \sum_{n=0}^{N} \delta s_n\, {}_I\boldsymbol{r}_n, \tag{6.63}$$

with the planar gravity vector $\boldsymbol{g} \in \mathbb{R}^2$. The n-th energy element depending on the translational element yields

$$V_{G,el,n}(\boldsymbol{q}_{el,tr,n}) = -\rho A\, {}_I\boldsymbol{g}^T \left[\overline{\delta s}_{n-1}\, {}_I\boldsymbol{r}_{n-1} + \overline{\delta s}_n\, {}_I\boldsymbol{r}_n\right], \tag{6.64}$$

with $\overline{\delta s}_n$ the new weight

$$\overline{\delta s}_0 := \delta s_0,\ \overline{\delta s}_n := \frac{\delta s_n}{2},\ \overline{\delta s}_N := \delta s_N. \tag{6.65}$$

The contribution to the equations of motion satisfies

$$\frac{\partial V_{G,el,n}}{\partial \boldsymbol{q}_{el,tr,n}} = -\rho A\begin{pmatrix}\overline{\delta s}_{n-1}\, {}_I\boldsymbol{g}^T, & 0, & \overline{\delta s}_n\, {}_I\boldsymbol{g}^T\end{pmatrix}. \tag{6.66}$$

Discrete kinetic energies

The translatory and rotatory energies form the kinetic energies.

Discrete translatory energy The discrete energy expression (with the trapezoidal rule) satisfies

$$T_T = \frac{\rho A}{2} \sum_{n=0}^{N} \delta s_n \|{}_I\dot{\boldsymbol{r}}_n\|^2. \tag{6.67}$$

The n-th energy element depending on the time derivative of the translational element is given by

$$T_{T,el,n}(\dot{\boldsymbol{q}}_{el,tr,n}) = \frac{\rho A}{2}\left[\overline{\delta s}_{n-1}\|{}_I\dot{\boldsymbol{r}}_{n-1}\|^2 + \overline{\delta s}_n\|{}_I\dot{\boldsymbol{r}}_n\|^2\right]. \tag{6.68}$$

The contribution to the right hand side of the equations of motion vanish

$$\frac{\partial T_{T,el,n}}{\partial \boldsymbol{q}_{el,tr,n}} = \boldsymbol{0}^T, \tag{6.69}$$

$$\frac{\partial^2 T_{T,el,n}}{\partial \dot{\boldsymbol{q}}_{el,tr,n}\partial \boldsymbol{q}_{el,tr,n}} = \boldsymbol{0}, \tag{6.70}$$

and the contribution to the mass matrix yields

$$\frac{\partial^2 T_{T,el,n}}{\partial \dot{\boldsymbol{q}}^2_{el,tr,n}} = \begin{pmatrix} \operatorname{diag}[\rho A\overline{\delta s}_{n-1}] & \\ & 0 & \\ & & \operatorname{diag}[\rho A\overline{\delta s}_n] \end{pmatrix}. \tag{6.71}$$

Discrete rotatory energy The discrete rotatory energy simplifies significantly compared to the spatial case as the angular velocity becomes scalar. By means of the midpoint rule it is given by

$$T_R = \frac{\rho}{2}\sum_{n=1}^{N} \Delta s_{n-\frac{1}{2}}\omega^2_{n-\frac{1}{2}} I = \sum_{n=1}^{N} T_{R,el,n}. \tag{6.72}$$

The angular velocity is gained by

$$\omega_{n-\frac{1}{2}} = {}_I\boldsymbol{n}^T_{n-\frac{1}{2}}\,{}_I\dot{\boldsymbol{t}}_{n-\frac{1}{2}} = {}_I\boldsymbol{n}^T_{n-\frac{1}{2}}\frac{\mathrm{d}\,{}_I\boldsymbol{t}}{\mathrm{d}\gamma}(\gamma_{n-\frac{1}{2}})\dot{\gamma}_{n-\frac{1}{2}} = \dot{\gamma}_{n-\frac{1}{2}}. \tag{6.73}$$

The n-th energy element depends only on the translational element

$$T_{R,el,n}(\dot{\boldsymbol{q}}_{el,tr,n}) = \frac{\rho}{2}\Delta s_{n-\frac{1}{2}} I\dot{\gamma}^2_{n-\frac{1}{2}}. \tag{6.74}$$

The contributions to the right hand side vector vanish

$$\frac{\partial T_{R,el,n}}{\partial \boldsymbol{q}_{el,tr,n}} = \boldsymbol{0}^T, \tag{6.75}$$

$$\frac{\partial^2 T_{R,el,n}}{\partial \dot{\boldsymbol{q}}_{el,tr,n} \partial \boldsymbol{q}_{el,tr,n}} = \boldsymbol{0}. \tag{6.76}$$

The contribution to the mass matrix is constant in the planar case

$$\frac{\partial^2 T_{R,el,n}}{\partial \dot{\boldsymbol{q}}^2_{el,tr,n}} = \begin{pmatrix} \boldsymbol{0} & & \\ & \rho \Delta s_{n-\frac{1}{2}} I & \\ & & \boldsymbol{0} \end{pmatrix}. \tag{6.77}$$

Discrete strain dissipation

The discrete strain dissipation reduces to the components in extension and normal shearing direction

$$D_{SE} = \sum_{n=1}^{N} \Delta s_{n-\frac{1}{2}} \, {}_I\dot{\boldsymbol{\varepsilon}}^T_{n-\frac{1}{2}} \, {}_I\boldsymbol{C}^{\boldsymbol{\varepsilon}}_D \, {}_I\dot{\boldsymbol{\varepsilon}}_{n-\frac{1}{2}} = \sum_{n=1}^{N} D_{SE,el,n}. \tag{6.78}$$

Hereby, the integral is approximated by means of the midpoint rule and the inertial strain rate is given by

$${}_I\dot{\boldsymbol{\varepsilon}}_{n-\frac{1}{2}} = \frac{{}_I\Delta\dot{\boldsymbol{r}}_{n-\frac{1}{2}}}{\Delta s_{n-\frac{1}{2}}} - {}_I\dot{\boldsymbol{t}}_{n-\frac{1}{2}}. \tag{6.79}$$

The damping matrix in the body fixed frame has the form

$${}_K\boldsymbol{C}^{\boldsymbol{\varepsilon}}_D = \begin{pmatrix} c^{\boldsymbol{\varepsilon}}_{0D} & \\ & c^{\boldsymbol{\varepsilon}}_{1D} \end{pmatrix}. \tag{6.80}$$

It is transformed to the inertial coordinate system according to

$${}_I\boldsymbol{C}^{\boldsymbol{\varepsilon}}_D = {}_{IK}\boldsymbol{A}_{n-\frac{1}{2}} \boldsymbol{C}^{\boldsymbol{\varepsilon}}_D \, {}_{IK}\boldsymbol{A}^T_{n-\frac{1}{2}}. \tag{6.81}$$

The n-th element dissipation term is given by

$$\begin{aligned} D_{SE,el,n}(\boldsymbol{q}_{el,tr,n}, \dot{\boldsymbol{q}}_{el,tr,n}) = \frac{1}{\Delta s_{n-\frac{1}{2}}} \Big\{ & c^{\boldsymbol{\varepsilon}}_{0D} \left(\left[{}_I\Delta\dot{\boldsymbol{r}}^T_{n-\frac{1}{2}} - {}_I\dot{\boldsymbol{t}}^T_{n-\frac{1}{2}} \Delta s_{n-\frac{1}{2}} \right] {}_I\boldsymbol{t}_{n-\frac{1}{2}} \right)^2 \\ & + c^{\boldsymbol{\varepsilon}}_{1D} \left(\left[{}_I\Delta\dot{\boldsymbol{r}}^T_{n-\frac{1}{2}} - {}_I\dot{\boldsymbol{t}}^T_{n-\frac{1}{2}} \Delta s_{n-\frac{1}{2}} \right] {}_I\boldsymbol{n}_{n-\frac{1}{2}} \right)^2 \Big\}. \end{aligned} \tag{6.82}$$

The contribution to the equations of motion satisfies

$$
\begin{aligned}
&\frac{\partial D_{SE}}{\partial \dot{\boldsymbol{q}}_{el,tr,n}} \\
&= \frac{2}{\Delta s_{n-1}} \Bigg\{ c^{\boldsymbol{\varepsilon}}_{0D}\, {}_I\boldsymbol{t}^T_{n-\frac{1}{2}} \left[{}_I\Delta\dot{\boldsymbol{r}}_{n-\frac{1}{2}} - {}_I\dot{\boldsymbol{t}}_{n-\frac{1}{2}}\, \Delta s_{n-\frac{1}{2}} \right] \left(-{}_I\boldsymbol{t}^T_{n-\frac{1}{2}}, -{}_I\boldsymbol{t}^T_{n-\frac{1}{2}} \frac{\mathrm{d}\,{}_I\boldsymbol{t}_{n-\frac{1}{2}}}{\mathrm{d}\,\gamma_{n-\frac{1}{2}}} \Delta s_{n-\frac{1}{2}}, {}_I\boldsymbol{t}^T_{n-\frac{1}{2}} \right) \\
&+ c^{\boldsymbol{\varepsilon}}_{1D}\, {}_I\boldsymbol{n}^T_{n-\frac{1}{2}} \left[{}_I\Delta\dot{\boldsymbol{r}}_{n-\frac{1}{2}} - {}_I\dot{\boldsymbol{t}}_{n-\frac{1}{2}}\, \Delta s_{n-\frac{1}{2}} \right] \left(-{}_I\boldsymbol{n}^T_{n-\frac{1}{2}}, -{}_I\boldsymbol{n}^T_{n-\frac{1}{2}} \frac{\mathrm{d}\,{}_I\boldsymbol{t}_{n-\frac{1}{2}}}{\mathrm{d}\,\gamma_{n-\frac{1}{2}}}, {}_I\boldsymbol{n}^T_{n-\frac{1}{2}} \right) \Bigg\}.
\end{aligned}
\tag{6.83}
$$

In the planar case, the following derivatives can be simplified to

$$
{}_I\dot{\boldsymbol{t}}_{n-\frac{1}{2}} = \begin{pmatrix} -\sin(\gamma_{n-\frac{1}{2}}) \\ \cos(\gamma_{n-\frac{1}{2}}) \end{pmatrix} \dot{\gamma}_{n-\frac{1}{2}}, \tag{6.84}
$$

and

$$
\frac{\mathrm{d}\,{}_I\boldsymbol{t}_{n-\frac{1}{2}}}{\mathrm{d}\gamma_{n-\frac{1}{2}}} = \begin{pmatrix} -\sin(\gamma_{n-\frac{1}{2}}) \\ \cos(\gamma_{n-\frac{1}{2}}) \end{pmatrix}. \tag{6.85}
$$

The equations of motion have the following form

$$
\boldsymbol{M}\ddot{\boldsymbol{q}} = \boldsymbol{h}. \tag{6.86}
$$

The block diagonal mass matrix satisfies

$$
\boldsymbol{M}(\boldsymbol{q}) = \begin{pmatrix} \boldsymbol{M}_0 & \boldsymbol{0} & \boldsymbol{0} \\ \boldsymbol{0} & \ddots & \boldsymbol{0} \\ \boldsymbol{0} & \boldsymbol{0} & \boldsymbol{M}_{N-1} \end{pmatrix}, \tag{6.87}
$$

with the n-th matrix element

$$
\boldsymbol{M}_n = \begin{pmatrix} \mathrm{diag}[\rho A \overline{\delta s}_n] & \boldsymbol{0} \\ \boldsymbol{0}^T & \rho \Delta s_{n+\frac{1}{2}} I \end{pmatrix}. \tag{6.88}
$$

The right hand side vector $\boldsymbol{h}$ simplifies to

$$
\boldsymbol{h}(\boldsymbol{q}, \dot{\boldsymbol{q}}) = -\frac{\partial\,(V_{SE} + V_{BT} + V_G)}{\partial\,\boldsymbol{q}} - \frac{\partial\,D_{SE}}{\partial\,\dot{\boldsymbol{q}}}. \tag{6.89}
$$

6.2.3 Contour description for set-valued force laws

The text of this subsection equates an only slightly modified part of the joint paper [10]. Whereas for the internal dynamics the DOFs are required only at discrete points, they have to be interpolated for the contour description. As internal dynamics and contour specification are conceptually independent, only the interpolated position and rotation curves of the neutral fibre are used for the contour characterisation. It is assumed that sufficient elements are used so that the differences between the Frenet-frame and the trihedral gained from the rotation grid are negligible and therefore the trihedral is almost perpendicular to the curve. The angle information can therefore be calculated out of the rotation grid. In addition, the Jacobian matrices are parametrised. The NURBS interpolation [39] is chosen as global interpolation method. The position curve satisfies

$$ {}_I\boldsymbol{r}(s) = \sum_n N_{r,n}(s)\,{}_I\boldsymbol{r}_n \tag{6.90} $$

with the basis functions $\left\{N_{r,n}\right\}_n$.

The Frenet frame is derived by means of differential geometry out of ${}_I\boldsymbol{r}(s)$. The tangent and normal are the first respectively second normalised derivatives with respect to the arc length s of the position curve. The binormal is obtained by means of the cross product:

$$ {}_I\boldsymbol{t}(s) = \frac{{}_I\boldsymbol{r}'(s)}{\|{}_I\boldsymbol{r}'(s)\|}, \quad {}_I\boldsymbol{n}(s) = \frac{{}_I\boldsymbol{r}''(s)}{\|{}_I\boldsymbol{r}''(s)\|}, \quad {}_I\boldsymbol{b} = {}_I\boldsymbol{t} \times {}_I\boldsymbol{n}. \tag{6.91} $$

Another approach to obtain the angles searches for the two closest angle DOFs (left and right) and applies a local linear interpolation

$$ \boldsymbol{\varphi}(s) = \boldsymbol{\varphi}_L + \frac{s - s_L}{l_0}(\boldsymbol{\varphi}_R - \boldsymbol{\varphi}_L). \tag{6.92} $$

A linear interpolation has been chosen for the angles like in the internal dynamics, cf. (6.57). This approach can be chosen if the Frenet frame method fails. For the velocity and the angular velocity

$$ {}_I\boldsymbol{v}(s) = \sum_n N_{v,n}(s)\,{}_I\boldsymbol{v}_n, \tag{6.93} $$

$$ {}_I\boldsymbol{\omega}(s) = \sum_n N_{\omega,n+\frac{1}{2}}(s)\,{}_I\boldsymbol{\omega}_{n+\frac{1}{2}}. \tag{6.94} $$

different basis functions $\left\{N_{v,n}\right\}_n$, $\left\{N_{\omega,n+\frac{1}{2}}\right\}_n$ may be used. The angular velocity vector is gained from the time derivatives of the angles by (6.19).

The Jacobian matrices on the staggered grid are calculated from internal dynamics.

The following definition for the element DOFs is introduced:

$$\boldsymbol{q}_n := \begin{pmatrix} {}_I\boldsymbol{r}_n \\ \boldsymbol{\varphi}_{n+\frac{1}{2}} \end{pmatrix}, \tag{6.95}$$

for $n = 0, \ldots, N-1$. The Jacobians of translation are located on the vertices

$${}_I\boldsymbol{J}_{T,n} = \frac{\partial\, {}_I\boldsymbol{r}_n}{\partial \boldsymbol{q}} = \left(\frac{\partial\, {}_I\boldsymbol{r}_n}{\partial \boldsymbol{q}_1}, \ \ldots\ , \ \frac{\partial\, {}_I\boldsymbol{r}_n}{\partial \boldsymbol{q}_{N-1}}\right) = \Big((\boldsymbol{0},\boldsymbol{0}), \ \ldots\ , \ \underbrace{(\boldsymbol{I},\boldsymbol{0})}_{n} \ \ldots\ , \ (\boldsymbol{0},\boldsymbol{0})\Big) \tag{6.96}$$

and the Jacobians of rotation are situated at the midpoints

$${}_I\boldsymbol{J}_{R,n+\frac{1}{2}} = \frac{\partial\, {}_I\boldsymbol{\omega}_{n+\frac{1}{2}}}{\partial \dot{\boldsymbol{q}}} = \left(\frac{\partial\, {}_I\boldsymbol{\omega}_{n+\frac{1}{2}}}{\partial \dot{\boldsymbol{q}}_1}, \ \ldots\ , \ \frac{\partial\, {}_I\boldsymbol{\omega}_{n+\frac{1}{2}}}{\partial \dot{\boldsymbol{q}}_{N-1}}\right) = \Big((\boldsymbol{0},\boldsymbol{0}), \ \ldots\ , \ \underbrace{(\boldsymbol{0},\boldsymbol{Y}_{n+\frac{1}{2}})}_{n} \ \ldots\ , \ (\boldsymbol{0},\boldsymbol{0})\Big). \tag{6.97}$$

By means of the NURBS interpolation, the parametrised Jacobians are obtained

$${}_I\boldsymbol{J}_T(s) = \sum_n N_{T,n}(s)\, {}_I\boldsymbol{J}_{T,n}, \tag{6.98}$$

$${}_I\boldsymbol{J}_R(s) = \sum_n N_{R,n+\frac{1}{2}}(s)\, {}_I\boldsymbol{J}_{R,n+\frac{1}{2}}, \tag{6.99}$$

with basis functions $\{N_{T,n}\}_n$, $\left\{N_{R,n+\frac{1}{2}}\right\}_n$. This information is used for either a description of the neutral fibre or a description of a flexible band. The flexible band is a flexible contour of a beam with cross-section that is placed perpendicular to the neutral fibre at a horizontal distance $\frac{b}{2}$ and a vertical distance d_N (cf. [45]):

$$\begin{aligned} {}_I\boldsymbol{B} : [0,L] \times \left[-\frac{b}{2}, \frac{b}{2}\right] &\to \mathbb{R}^3, \\ (s,\mu) &\mapsto {}_I\boldsymbol{r}(s) + d_N \frac{\theta_1\, {}_I\boldsymbol{n}(s) + \theta_2\, {}_I\boldsymbol{b}(s)}{\sqrt{\theta_1^2 + \theta_2^2}} + \mu \frac{\theta_1\, {}_I\boldsymbol{b}(s) - \theta_2\, {}_I\boldsymbol{n}(s)}{\sqrt{\theta_1^2 + \theta_2^2}}. \end{aligned} \tag{6.100}$$

The parameters $\theta_1, \theta_2 \in \{-1,0,1\}$ depend on the relative band location with respect to the neutral fibre: top, bottom, left or right. With the formulas of this section and the set-valued force laws a point - flexible band contact can be calculated which is used for the application in the CVT.

6.2.4 Initialisation of Cosserat rod ring sets

The initialisation is described for the non tapered case and for the general case of the spatial Cosserat rod model, whereof the planar DOFs are extracted. Four sections - push part, secondary pulley, loose part and primary pulley - exist as in [45]. The initialisation is performed similar to Subsection 4.2.2 for the spatial RCM beam with the difference that the Cosserat beam model has only six rigid DOFs per finite element and no flexible coordinates. In addition, the angles in the Cosserat case are staggered which results in different cases for the initialisation of the two Cardan angles β and γ. It has to be distinguished if the rotation grid of the current element is situated in the same section as the position grid or already in the next section.

Position and rotation initialisation

The initialisation of the beam model is implemented anti-clockwise and against the running direction with the angle φ from Figure 4.2. It starts at the transition between secondary pulley and push part and leads over the pushpart and the primary arc. Only the first two parts are shown below as the other two are implemented likewise
$0 \le i l_0 < t_l$ - **node on push part** (upper straight part):

$$\begin{pmatrix} x_i \\ y_i \end{pmatrix} = i l_0 \begin{pmatrix} \sin(\varphi) \\ \cos(\varphi) \end{pmatrix} + r_O \begin{pmatrix} -\cos(\varphi) \\ \sin(\varphi) \end{pmatrix}, \tag{6.101}$$

$$z_i = \left(1 - \frac{i l_0}{t_l}\right) q_{0_{O_M}} + \frac{i l_0}{t_l} q_{0_{I_M}} \pm \frac{w_S + w_P}{4}, \tag{6.102}$$

$$\alpha_{i+\frac{1}{2}} = 0, \tag{6.103}$$

$$\beta_{i+\frac{1}{2}} = \begin{cases} \arctan\left(\dfrac{q_{0_{O_M}} - q_{0_{I_M}}}{\sin(\varphi) d_A}\right), & \text{if } t_l - i l_0 > 0.5 l_0, \\ 0, & \text{else,} \end{cases} \tag{6.104}$$

$$\gamma_{i+\frac{1}{2}} = \begin{cases} 0.5\pi - \varphi, & \text{if } t_l - i l_0 > 0.5 l_0, \\ 0.5\pi - \varphi - \dfrac{(i+0.5) l_0 - t_l}{r_I}, & \text{else.} \end{cases} \tag{6.105}$$

$$\tag{6.106}$$

$t_l \le i l_0 < t_l + b_I$ - **node on primary arc** with $\alpha_I = \dfrac{i l_0 - t_l}{r_I}$ and $\alpha_{I,R} = \dfrac{(i+0.5) l_0 - t_l}{r_I}$:

$$\begin{pmatrix} x_i \\ y_i \end{pmatrix} = \begin{pmatrix} d_A \\ 0 \end{pmatrix} + r_I \begin{pmatrix} -\cos(\varphi + \alpha_I) \\ \sin(\varphi + \alpha_I) \end{pmatrix}, \tag{6.107}$$

$$z_i = q_{0_{I_M}} \pm \frac{w_S + w_P}{4}, \tag{6.108}$$

$$\alpha_{i+\frac{1}{2}} = 0, \tag{6.109}$$

$$\beta_{i+\frac{1}{2}} = \begin{cases} 0, & \text{if } t_l + b_I - i l_0 > 0.5 l_0, \\ \arctan\left(\dfrac{q_{0_{I_M}} - q_{0_{O_M}}}{\sin(\varphi) d_A}\right), & \text{else,} \end{cases} \tag{6.110}$$

$$\gamma_{i+\frac{1}{2}} = \begin{cases} 0.5\pi - \varphi - \alpha_{I,R}, & \text{if } t_l + b_I - i l_0 > 0.5 l_0, \\ -\dfrac{3}{2}\pi + \varphi, & \text{else.} \end{cases} \tag{6.111}$$

$$\tag{6.112}$$

Two different angles for the position α_I and rotation $\alpha_{I,R}$ in the arcs have to be used because of the staggered grid. Loose part and secondary arc are initialised likewise.

Velocity initialisation

The velocities are initialised as in [45] with the kinetic Sattler model explained in Section 4.1. The belt velocity v depends on the angle inside the pulley. The components $u_{z,i}$, $\omega_{x,i+\frac{1}{2}}$ and $\omega_{y,i+\frac{1}{2}}$ are initialised zero for simplification.

$0 \leq i l_0 < t_l$ - **node on push part** (upper straight part):

$$\begin{pmatrix} u_{x,i} \\ u_{y,i} \end{pmatrix} = \begin{pmatrix} -\cos(0.5\pi - \varphi) \\ -\sin(0.5\pi - \varphi) \end{pmatrix} v(-\varphi), \tag{6.113}$$

$$u_{z,i} = 0, \tag{6.114}$$

$$\omega_{x,i+\frac{1}{2}} = 0, \tag{6.115}$$

$$\omega_{y,i+\frac{1}{2}} = 0, \tag{6.116}$$

$$\omega_{z,i+\frac{1}{2}} = 0. \tag{6.117}$$

$$\tag{6.118}$$

$t_l \leq i l_0 < t_l + b_I$ - **node on primary arc** with $\alpha_I = \dfrac{i l_0 - t_l}{r_I}$:

$$\begin{pmatrix} u_{x,i} \\ u_{y,i} \end{pmatrix} = \begin{pmatrix} -\cos(0.5\pi - \varphi - \alpha_I) \\ \sin(0.5\pi - \varphi - \alpha_I) \end{pmatrix} v(2\pi - \alpha_I - \varphi), \tag{6.119}$$

$$u_{z,i} = 0, \tag{6.120}$$

$$\omega_{x,i+\frac{1}{2}} = 0, \tag{6.121}$$

$$\omega_{y,i+\frac{1}{2}} = 0, \tag{6.122}$$

$$\omega_{z,i+\frac{1}{2}} = \begin{cases} \omega_I, & \text{if } t_l + b_I - i l_0 > 0.5 l_0, \\ 0, & \text{else.} \end{cases} \tag{6.123}$$

$$\tag{6.124}$$

By this approach, the ring sets with the Cosserat rod model can be initialised successfully. Both (planar and spatial) Cosserat rod models have already been successfully validated by means of academic examples [56, 11]. However, as they turned out to be very stiff, the application of the Cosserat rod model into the pushbelt CVT model leads to impracticable small time step sizes in the numerical integration and thus a large computing time. A possible remedy is the nonlinear model order reduction shown in the next section.

6.3 Nonlinear model order reduction

In model order reduction, a large-scale (linear or nonlinear) dynamical system is approximated by a low order system with only a small number of DOFs with the same system characteristics. Thereby, the approximation algorithm should be fast, the error should be small and an a priori error estimator is desired to control the dimensionality of the reduced system. As the Cosserat rod model turned out to be very stiff, a method of nonlinear model order reduction is applied to truncate high numerical frequencies from the system. The number of DOFs used for the ring sets is with about $100-300$ not very large compared to typical systems in model order reduction. Thus, the model order reduction technique is used in this study primarily to filter out high frequencies and only as a side product to lower the DOFs.

The most commonly used method for nonlinear dynamical systems, the *proper orthogonal decomposition* (POD), has been chosen to reduce the nonlinear equations of motion and obtain a low order model. This method is explained in detail in [3]. The presented concept is general and works for the planar as well as the spatial Cosserat rod model. The POD method requires a full simulation of the original model, which can be done offline. It uses the calculated information of the state of the system at pre-specified time-instances. The matrix $\boldsymbol{X}$ stores the n time snapshots of a full simulation of the model

$$\boldsymbol{X} = \big(\boldsymbol{q}(t_1), \dots, \boldsymbol{q}(t_n)\big) \in \mathrm{I\!R}^{N\times n}, \tag{6.125}$$

with $N > n$. That means less snapshots than the DOFs of the system are used. Starting from this matrix $\boldsymbol{X}$, a basis for a subspace of the solution of a lower dimension has to be found. The snapshots are not used as a basis because of possible linear dependency of some columns of $\boldsymbol{X}$. Hence, the singular value decomposition (SVD) is applied to calculate this basis. The SVD is a matrix decomposition which provides the optimal rank k approximation of a rectangular matrix in the 2-norm [3]. The singular value decomposition of the snapshot matrix has the form

$$\boldsymbol{X} = \boldsymbol{U}\boldsymbol{\Sigma}\boldsymbol{V}^T, \qquad \boldsymbol{\Sigma} = \mathrm{diag}(\sigma_1, \dots, \sigma_n) \in \mathrm{I\!R}^{N\times n}, \tag{6.126}$$

with the orthogonal matrices $\boldsymbol{U} = (\boldsymbol{u}_1, \dots, \boldsymbol{u}_N) \in \mathrm{I\!R}^{N\times N}$ and $\boldsymbol{V} = (\boldsymbol{v}_1, \dots, \boldsymbol{v}_n) \in \mathrm{I\!R}^{n\times n}$. The singular values σ_i are sorted according to their size

$$\sigma_1 \geq \sigma_2 \geq \dots \geq \sigma_n \geq 0. \tag{6.127}$$

The remaining entries of the matrix $\boldsymbol{\Sigma}$ are zeros. Orthogonal matrices in general have the advantage that their numerical condition is equal to 1 and therefore round-off errors are not magnified and a robust algorithm is obtained. Their inverse is just the transposed of the matrix. The relationship between singular values σ_i and eigenvalues λ_i is given by

$$\sigma_i(\boldsymbol{X}) = \sqrt{\lambda_i(\boldsymbol{X}^T\boldsymbol{X})} \qquad i = 1,\dots,n. \tag{6.128}$$

Hence, the squares σ_i^2, $i = 1,\dots,n$ are the eigenvalues of $\boldsymbol{X}^T\boldsymbol{X}$ resp. $\boldsymbol{X}\boldsymbol{X}^T$ to the eigenvectors $\boldsymbol{v}_i$ resp. $\boldsymbol{u}_i$, $i = 1,\dots,n$. Assume, that the decay of the singular values of $\boldsymbol{X}$ in the application is rapid and only the first $k < n$ are significant to represent the model. Then, the first k columns of $\boldsymbol{U}$ are extracted into the projection matrix

$$\boldsymbol{P} = (\boldsymbol{u}_1,\dots,\boldsymbol{u}_k) \in \mathrm{I\!R}^{N\times k}. \tag{6.129}$$

The matrix $\boldsymbol{P}$ consists now of the POD basis with the most important generalised eigenfunctions of the system whose linear span approximates the linear span of the set of the snapshots best concerning the 2-norm, cf. [12] for details. By means of the projection matrix, the vector of DOFs is projected

$$\hat{\boldsymbol{q}} = \boldsymbol{P}^T\boldsymbol{q}. \tag{6.130}$$

This projection is applied to the equations of motion (6.86)

$$\boldsymbol{M}\,\boldsymbol{P}\ddot{\hat{\boldsymbol{q}}} = \boldsymbol{h}(\boldsymbol{P}\hat{\boldsymbol{q}},\boldsymbol{P}\dot{\hat{\boldsymbol{q}}}). \tag{6.131}$$

In a second step, the equations are projected by the same matrix called a POD-Galerkin approximation and the reduced system is gained

$$(\boldsymbol{P}^T\boldsymbol{M}\boldsymbol{P})\,\ddot{\hat{\boldsymbol{q}}} = \boldsymbol{P}^T\boldsymbol{h}(\boldsymbol{P}\hat{\boldsymbol{q}},\boldsymbol{P}\dot{\hat{\boldsymbol{q}}}). \tag{6.132}$$

In the evaluation of the nonlinear vector $\boldsymbol{h}$, still the full vector $\boldsymbol{q}$ and its time derivative $\dot{\boldsymbol{q}}$ have to be known. Different techniques exist for an intelligent evaluation only on special points, such as the discrete empirical interpolation method cf. [12]. These strategies are not of great importance in this application as the number N of the DOFs is relatively small and this evaluation does not take much CPU-time. The main goal is to use a larger time step size for the integration. In the test with academic examples, this was possible for systems with contacts [56]. However, this approach has not yet been tested for the pushbelt CVT model.

7 Results and Verification

In [45], a first validation of the spatial model explained in Section 3.2 has been done. The different element contact forces, the thrust ratio, the spiral running and the alignment setting have been investigated and compared with measurements. In these comparisons, there is still room for improvement, e.g. in terms of the element contact forces, which is further approached in this study. For this purpose, the local element contact forces, and the global phenomena spiral running and thrust ratio are analysed with regard to the different model enhancements. In a follow-up of this study, an intensified validation of the overall spatial model will be carried out where these phenomena and others like efficiency, slip curves, bearing forces and noise - vibration - harshness will be validated with measurements from Bosch. Therefore, this chapter intends to not supply a complete but rather a further validation. In addition, it means to demonstrate where the individual model enhancements have an effect on and what the explicit changes are. As this study contains a large number of multifaceted enhancements, not all effects of every possible combination of the enhancements can be provided. Nonetheless, the major impact is presented. The reduced hybrid model of Section 6.1 is applied for the comparisons of this chapter. It represents the analysed planar phenomena with a much lower computing time than the spatial model according to the following verification.

Different realistic boundary settings in the ratios OD ($i_r < 1$), MED ($i_r = 1$) and LOW ($i_r > 1$) have been chosen for the verification. The boundary conditions for the element contact forces are shown in Table 7.1, those for the thrust ratio in Table 7.2 and those for the spiral running in Table 7.3. Measurements of Bosch for the element - pulley normal contact force, the thrust ratio and the spiral running are available for these settings. In addition, measurements of Honda for the six element contact forces exist in the literature in comparable settings [23]. In the following, the torque ratio ξ is defined by

$$\xi = \frac{M_I}{M_{I,\max}}\,, \tag{7.1}$$

with the maximum transmittable torque $M_{I,\max}$ at the primary pulley specified by the measurements. Through the applied cases, large spectra of the geometric and torque ratios are covered and many details of the pushbelt CVT can be obtained. As measurements on the running belt are very complex and also describe a large intervention into the physical system (e.g. change of the elements for application of strain gauges or transmitters on the belt), most often only qualitative statements can be made. This applies in particular to the comparison with the Honda measurements, which have been performed with unrealistic low speeds and therefore also for different boundary settings than in Table 7.1. However, as the element contact forces depend mainly on the transmission and torque ratio, a qualitative comparison is possible, cf. [45]. Even if these measurements are from 1994, they are still one of the most reliable measurements available in literature for the element contact forces.

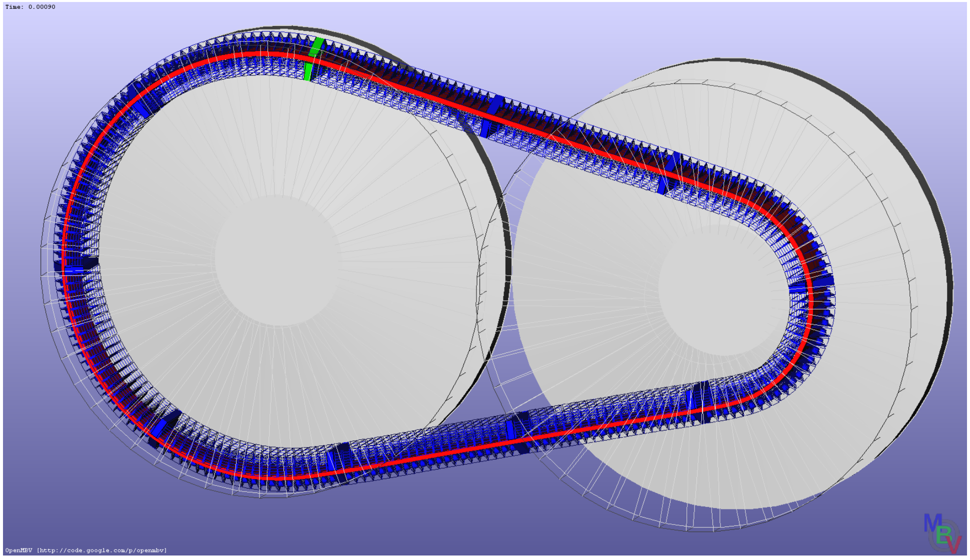

Figure 7.1: Simulation model of the pushbelt CVT variator for LOW

In the simulation 220 elements and 52 (RCM) finite elements for the ring sets are used. The number of elements in reality N_{E_0} is set to 432 in the OD and MED cases and 433 in the LOW cases. One drawback of the simulation model is its design to specify the geometric ratio, in contrast to the measurements where most often the speed ratio ($i_s = \omega_I / \omega_O$) is used. These ratios are not exactly the same, but depend in addition on the relative slip s_r [55]:

$$i_s = i_r + s_r \cdot i_r . \tag{7.2}$$

Therefore, depending on the case, the geometric ratio has to be adapted. For the OD and MED cases it is approximately equal to the speed ratio and thus also equally chosen. However for the case LOW, it is chosen different ($i_r = 2.25$). If nothing else is stated, the half explicit time-stepping scheme of Section 2.7 is applied with an integrator step size $\Delta t = 10^{-6}$s and a plot step size of 10^{-4}s. The end time of the integration is set between 0.07s and 0.12s depending on the setting. To reduce the computing time, the results of only 10 elements uniformly distributed over the pushbelt are plotted. These 10 elements are drawn as 'filled' in Figure 7.1 in contrast to the remaining 210 elements where only the contour lines are drawn. The green element is denoted with 'Element 1' and the numbering is done anti-clockwise (which is also the running direction of the pushbelt). 'Element 1' is situated in the transition from pushpart to secondary pulley. At least one complete cycle is simulated which corresponds to the time as only steady states are regarded. In this cycle each element traverses the four sections primary (pulley) - pushpart - secondary (pulley) - loosepart at different time instances. In the process of these four sections, the contact forces of the 10 elements with the other possible contact partners (pulleys, elements, ring sets) are plotted. This results in the six element contact forces: the element - pulley normal contact as well as longitudinal and radial friction force, the element - element normal contact force and the element - ring set normal contact as well as longitudinal friction force.

7.1 Hybrid pushbelt CVT model

At the beginning of this chapter, the hybrid pushbelt CVT model is validated, as it is used to demonstrate the effects of the different model enhancements later on. The analysed phenomena are the element contact forces, the thrust ratio and the spiral running.

7.1.1 Element contact forces

The six element force components of the hybrid model are qualitatively compared with the measurements of the Doshisha University Kyoto and Honda R&D [23]. The measurements are only available in a qualitative setup without any quantitative values, axes, zero level or other lines to show respective sections and are presented exactly as they are. The analysed boundary settings OD, MED and LOW are given in Table 7.1. In LOW two different speed ratios are applied, which are 2.0 in the Honda measurements and 2.36 in the Bosch measurements.

Table 7.1: Boundary settings for element contact forces

	OD	MED	LOW
$i_s\,[-]$	0.5	1.0	{2.0, 2.36}
$\omega_I\,[\mathrm{s}^{-1}]$	$1000 \cdot \frac{2\pi}{60}$	$2000 \cdot \frac{2\pi}{60}$	$2000 \cdot \frac{2\pi}{60}$
$M_O\,[\mathrm{N\,m}]$	0	74.58	198.24
$F_{C_O}\,[\mathrm{N}]$	6128	10520	33420
$\xi\,[-]$	0.0	0.65	0.81

The Honda setting with a speed ratio of 0.5 and a torque ratio of 0.0 correlates with the OD case. A primary angular velocity of 15.7$[\mathrm{s}^{-1}]$ and a secondary clamping force of 2670[N] are used in this setting. For the simulation model, the coupled element -

pulley and bilateral element - ring set normal contact laws are chosen. In Figure 7.2, the element contact force measurements and simulation results are shown.

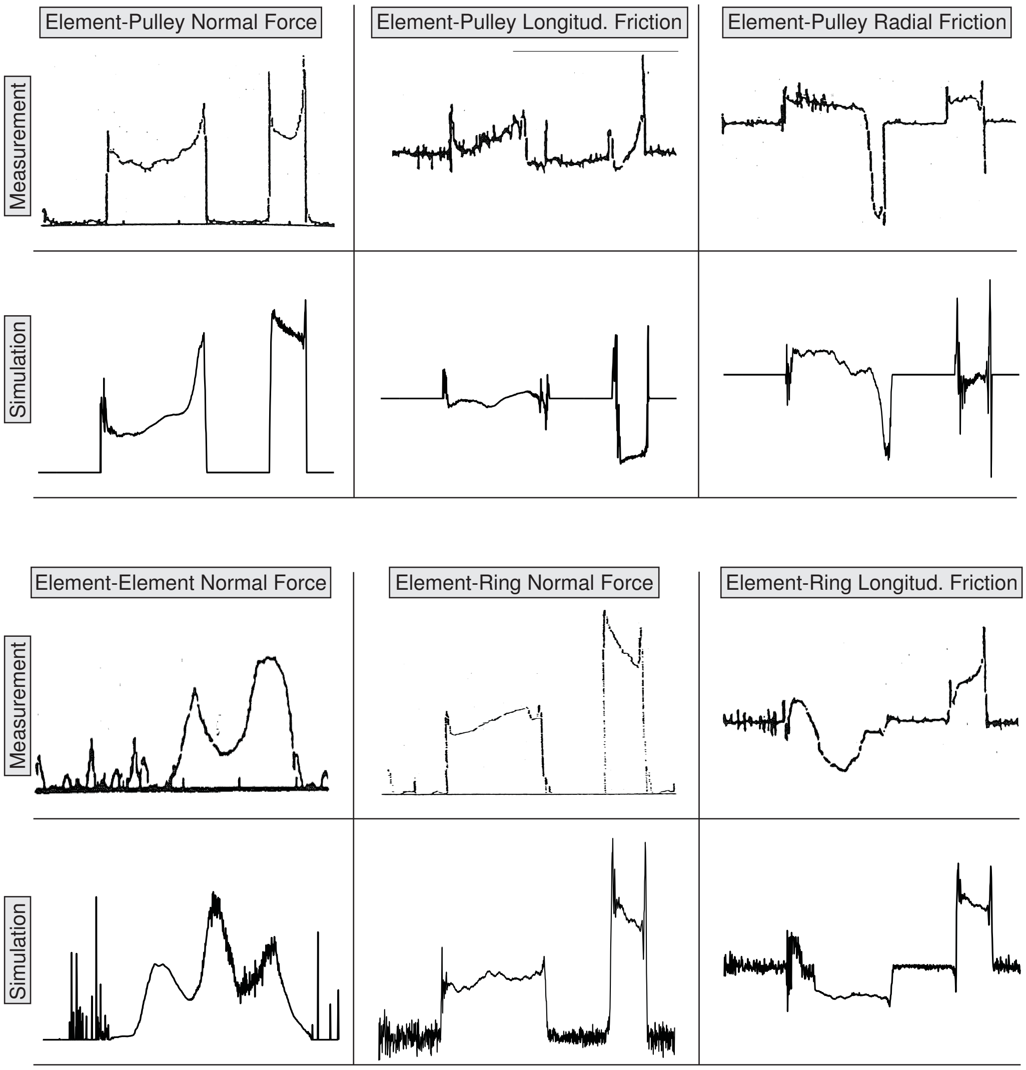

Figure 7.2: Measurement and simulation of element contact forces for OD

The results are very good. All contact forces and their different phenomena are depicted. The force peaks at the beginning and the end of the element - pulley normal contact are present in the model. The force increase and sagging in the larger arc is represented. In the smaller arc the sagging can already be seen in combination with a force decrease as in [17]. Also the course of the friction forces equates the measurements. Especially the larger arc in the radial friction is represented in detail. Unlike in the measurements, the element - pulley longitudinal friction is mainly negative in the smaller arc. Further, the level of the larger arc of the element - pulley longitudinal friction and of the smaller arc of the radial friction is too low compared to the measurements. This variance of results is similar to the ones gained in [17]. In the simulation of the element - element normal force, a middle rise in the pushpart occurs because the element top force is additionally considered in the model, which acts primarily in the pushpart. This is in contrast to the measurements where only the rocking edge force is measured, see [45]. Both element - ring set forces depict the measurements in detail. In the normal contact all phenomena are present. In the longitudinal friction in the smaller arc a decrease can be seen instead of an increase in the measurements. Again, the variance is similar to the model [17].

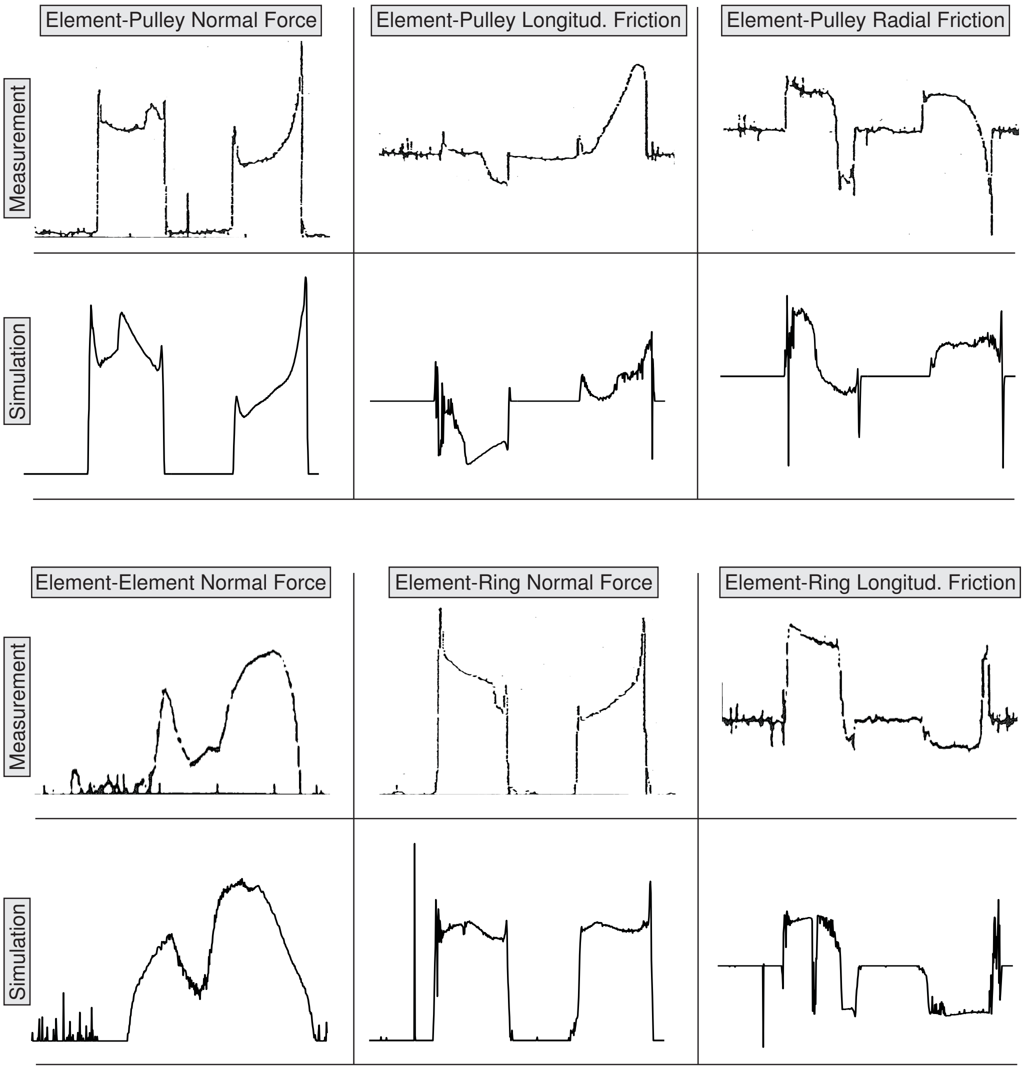

Figure 7.3: Measurement and simulation of element contact forces for MED

For the MED case, the Honda setting with a speed ratio of 1.0 and a torque ratio of

0.77 is taken for a qualitative comparison. The primary angular velocity is 20.5[s^{-1}] and the secondary clamping force is 3480[N] in this setting. Measurements and simulation are presented in Figure 7.3.

Again, a very detailed correlation can be seen. All six element contact forces reflect the measurements very well. Likewise, the level of all friction forces in both arcs is in accordance with the measurements. The peaks and sagging in the element - pulley normal contact are represented.

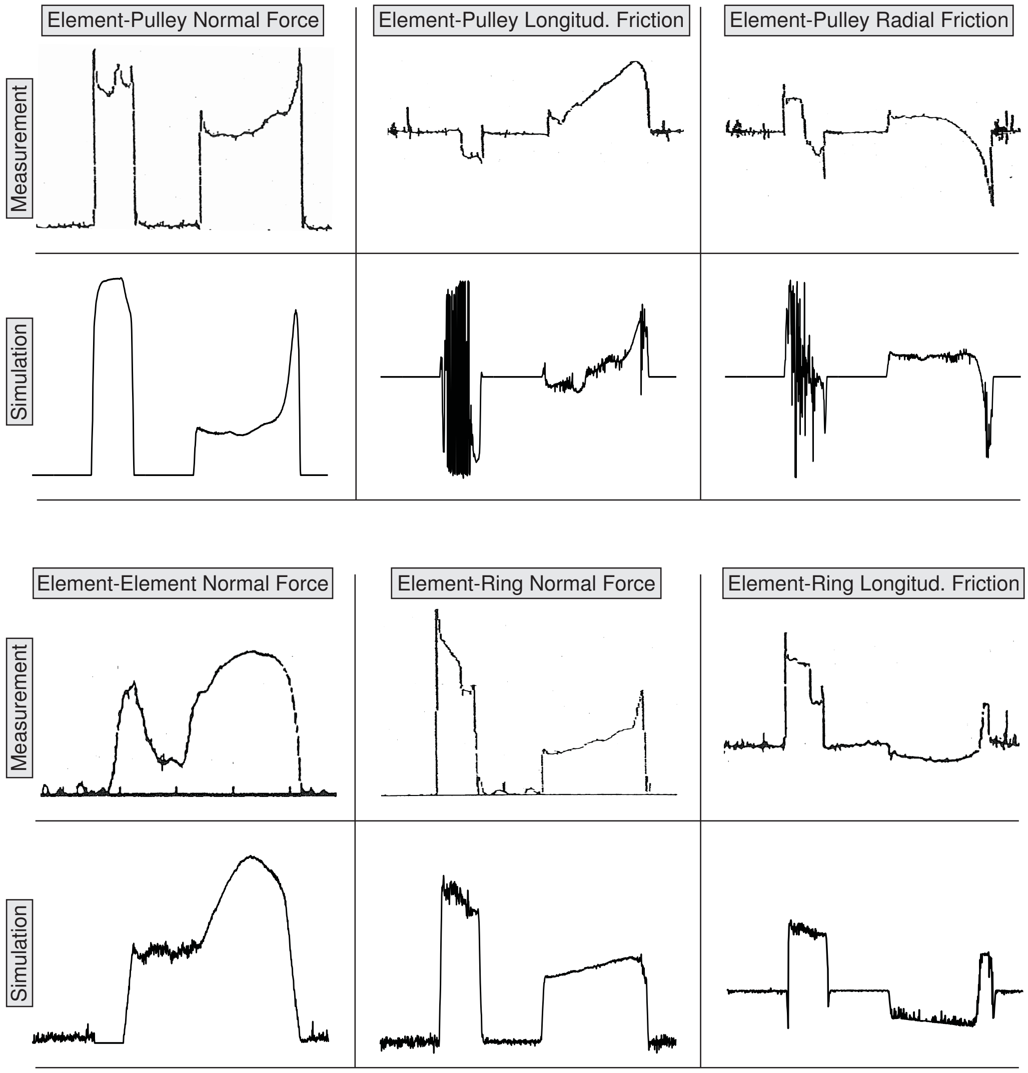

Figure 7.4: Measurement and simulation of element contact forces for LOW

For the LOW case, the measurement setting with a speed ratio of 2.0 and a torque ratio of 0.77 is taken for a qualitative comparison. There, a primary angular velocity of 31.4[s^{-1}] and a secondary clamping force of 5340[N] are used. In the simulation the geometric ratio has been set to $i_r = 1.9$ for this comparison. In Figure 7.4, the element contact forces of the measurements and simulation are shown.

For all six contacts, the larger arc is represented in detail. In the element - pulley normal contact, the force increase and sagging in the larger arc is represented. The larger arc of the radial contact correlates very well with the measurements. However, in the smaller arc there is still room for improvement. The three force peaks in the element - pulley normal contact are not present in the smaller arc. In the longitudinal and radial friction an oscillation is present in the smaller arc. In the larger arc of the element - pulley longitudinal friction a force increase from negative to positive can be seen in the simulation similar to the model [17]. The course of the element - element normal contact force in the model results again from the additional top contact closed in the pushpart and depicts the expected behaviour. The element - ring set contact and friction forces matches with the measurements in detail. Even the change of sign in the longitudinal friction in the larger arc is present.

Altogether, the element contact forces are depicted very well and the model quality has been significantly improved by the model enhancements. Yet, still some areas with potential for improvement can be seen for single forces in the smaller arc especially in the LOW case. The different effects of each enhancement will be developed step by step in the following.

7.1.2 Thrust ratio

The thrust ratio

$$k_{pks} = \frac{F_{C_I}}{F_{C_O}} \tag{7.3}$$

describes the ratio between primary and secondary clamping force and is essential for the pulley slip cf. [45].

Table 7.2: Boundary settings for thrust ratio

	OD-KpKs	MED
$i_s\,[-]$	0.5	1.0
$\omega_I\,[\mathrm{s}^{-1}]$	$2000 \cdot \frac{2\pi}{60}$	$2000 \cdot \frac{2\pi}{60}$
$M_O\,[\mathrm{N\,m}]$	{2, 15.44, 30.88, 46.32, 61.76, 72.5, 77}	{2, 24.86, 49.72, 74.58, 99.43, 116}
$F_{C_O}\,[\mathrm{N}]$	11140	10520
$\xi\,[-]$	{0.025, 0.19, 0.39, 0.58, 0.78, 0.91, 0.97}	{0.017, 0.22, 0.43, 0.65, 0.86, 1.0}

Quantitative measurements in different transmission ratios from Bosch Transmission Technology B.V. are available and are used to validate the model. In Table, 7.2, the cases

OD-KpKs and MED are summarised. For each case the entire spectrum of the torque ratio is applied. The comparison between simulation and measurements for the cases OD-KpKs and MED are shown in Figure 7.5. The thrust ratio is plotted over the torque ratio. For the simulation, the thrust ratio values of the fixed torque ratios of Table 7.2 are drawn with a circle and connected linearly. The unilateral element - ring set contact and the coupled element - pulley normal contact laws are used in the model. Also for quantitative values, a very good agreement can be seen in both cases.

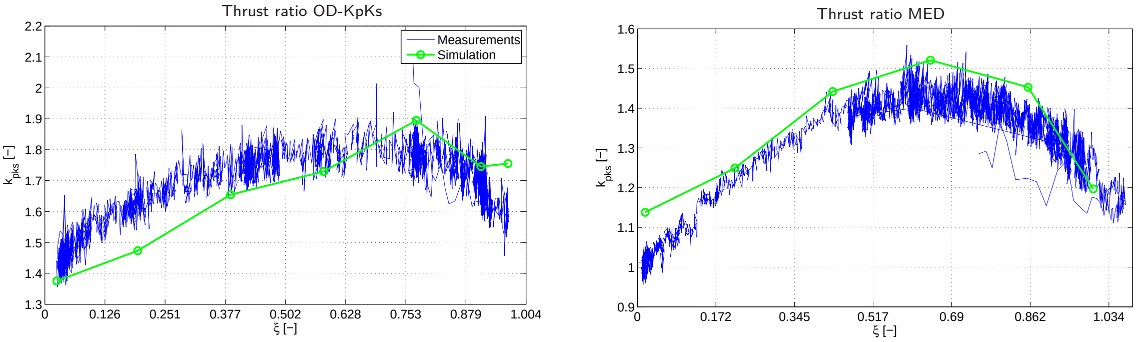
Thrust ratio OD-KpKs

Thrust ratio MED

Figure 7.5: Measurement and simulation of thrust ratio for OD-KpKs and MED

7.1.3 Spiral running

The spiral running is the deviation of the pushbelt's run in the pulleys from the circular arc. It is "mainly influenced by the sheave flexibility and the prestressing of the ring packages" [45, p. 78]. The setting OD-SpiRun for the spiral running is given in Table 7.3. The entire torque ratio from zero to one is applied with four discrete values.

Table 7.3: Boundary settings for spiral running

	OD-SpiRun	LOW-SpiRun
$i_s\,[-]$	0.5	2.4
$\omega_I\,[\mathrm{s}^{-1}]$	$2000 \cdot \frac{2\pi}{60}$	$2000 \cdot \frac{2\pi}{60}$
$M_O\,[\mathrm{N\,m}]$	{0, 32.4, 56.7, 81}	{0, 104, 208, 260}
$F_{C_O}\,[\mathrm{N}]$	18000	35000
$\xi\,[-]$	{0.0, 0.4, 0.7, 1.0}	{0.0, 0.4, 0.7, 1.0}

The comparisons between measurements from Bosch and simulation for the case OD-SpiRun are shown in Figure 7.6. The radial distance from the sheave centre to the top of the ring set is plotted over the angle in the pulley. For the primary pulley the four torque ratios of Table 7.3 are in top-down and for the secondary pulley in bottom-up assembly. The unilateral element - ring set and coupled element - pulley normal contacts laws are used in the simulation. With the coupled element - pulley normal contact law, this behaviour is improved significantly. For both, primary and secondary pulley, the characteristic behaviour can be seen. Only the level of the radii differs. It is too low in the primary and too high in the secondary pulley. That means the transmission ratio of simulation and measurement is different.

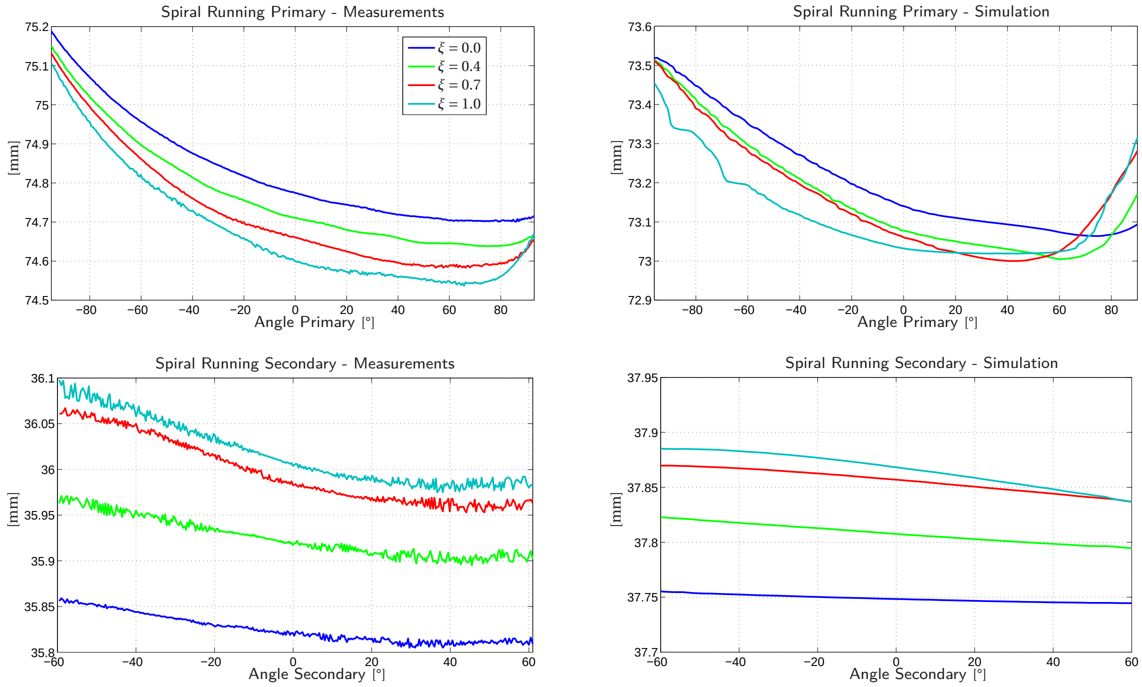

Figure 7.6: Measurements and simulation of spiral running for OD-SpiRun

The comparison between measurements and simulation for the case LOW-SpiRun is shown in Figure 7.7. The course in the secondary pulley is in very good agreement to the measurements. In the primary pulley a different behaviour can be seen. Again, the ratio of primary and secondary radii is different, leading to a different level of the spiral running.

7.1.4 Computing time reduction

Overall, the hybrid model reflects the phenomena element contact forces, thrust ratio and spiral running very well. This validates the hybrid model and shows its capability to represent these phenomena and therefore not the entire spatial model is required. In addition, this model reduction significantly decreases the computing time. The hybrid

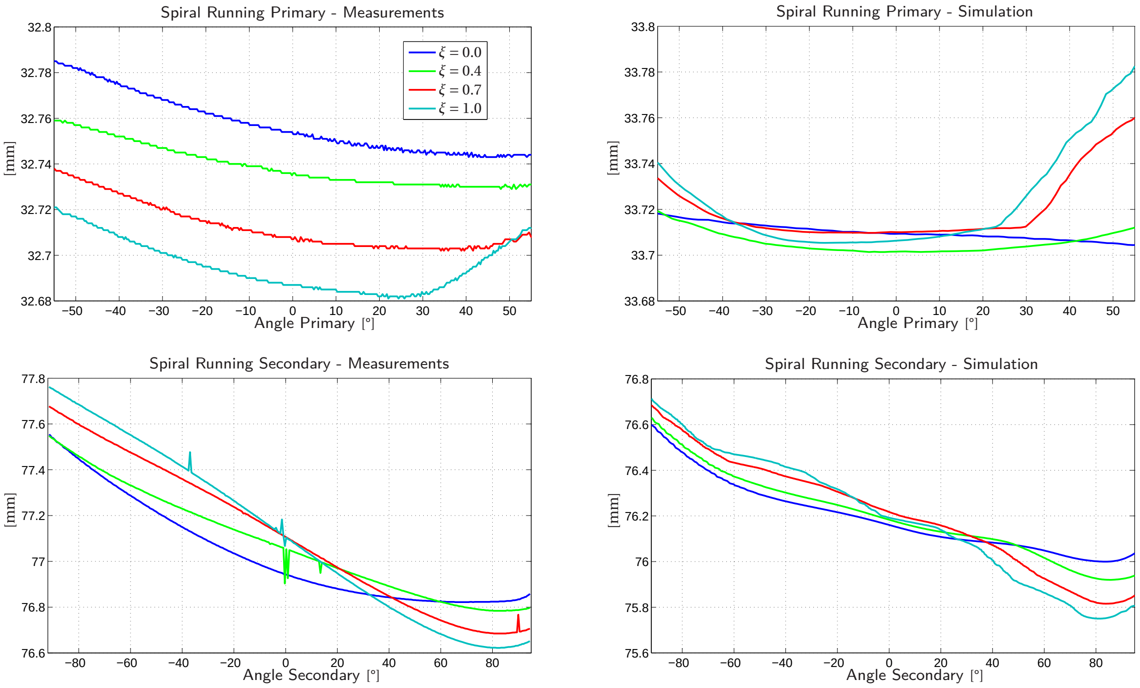

Figure 7.7: Measurements and simulation of spiral running for LOW-SpiRun

model is about nine times faster than the full spatial model. Of course, most spatial phenomena such as alignment cannot be represented by the hybrid model. Thus, it is an extreme computing time reduction in regards to the planar phenomena. With the simple element - pulley contact which uses only one fixed contact point per element flank, described in Subsection 6.1.2, an additional computing time reduction between about 4% and 8% (depending on the setting) in the hybrid model can be obtained.

7.2 Tapered elements

Regarding tapered elements, the expected changes are in the areas of operational endplay, element - element normal forces and curvature of the straight parts. The operational endplay is the sum of all positive contact distances of the element - element normal contact points. In general, one expects less operational endplay for the tapered case. This can also be seen in the element - element normal forces. Here, for torques beyond transition (which all analysed cases are part of), the region on the primary pulley where the force is zero should decrease with increasing taperedness. In addition, in the push part the cat's back should increase the more tapered the elements are.

7.2.1 Operational endplay

In the simulation, the 'non-tapered' case ($t_T = t_R$) with coupled element - pulley and unilateral element - ring set contact is compared to the cases 'tapered 05' ($t_T = t_R + 5\,\mu\text{m}$) and 'tapered 08' ($t_T = t_R + 8\,\mu\text{m}$). The operational endplay at the element top contact is plotted in Figure 7.8 for the cases OD and LOW. For both cases a similar behaviour can be seen. The operational endplay at the top decreases the more the elements are tapered, as expected.

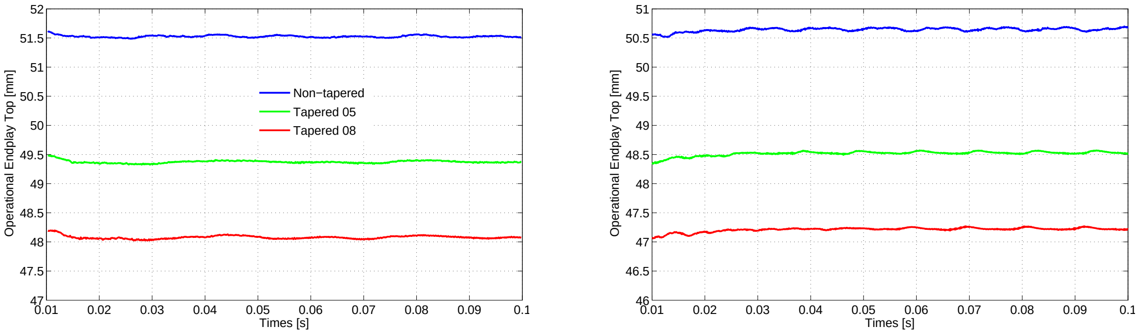

Figure 7.8: Operational endplay at element top for OD and LOW

7.2.2 Element contact forces

The element contact forces do not change significantly comparing these three cases. Only a slightly horizontal shifting of the graphs from right to left can be observed the more the elements are tapered. This means that the individual sections primary - pushpart - secondary - loosepart occur earlier the more taperedness is applied. However, in the element - element normal forces differences can be seen. In addition to the explained shifting, the force level increases the more the elements are tapered, see

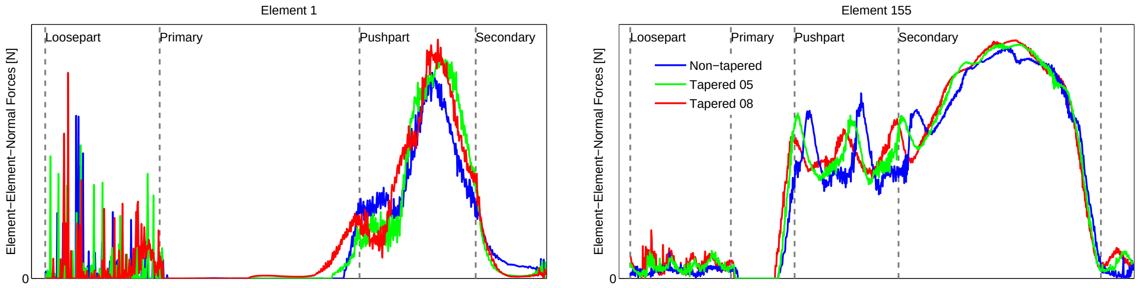

Figure 7.9: Element-element normal contact force for OD (left) and LOW (right)

Figure 7.9. Further, the push force starts earlier in the primary for the tapered case. This is caused also by the less endplay.

A comparison of the start and end positions of the ring set in the visualisation shows that the start position of the non-tapered case fits the best with the end position of the ring set. At the end, all three cases are located approximately at this position. The cat's back at the end is more distinct the more tapered the elements are. A consequence is that the transient effect at the beginning of the simulation lasts longer and the oscillations of the pushbelt have larger amplitudes for the tapered cases as the approximation of the steady state is better for the non-tapered case.

7.2.3 Thrust ratio

Looking at the thrust ratio, it can be seen that the taperedness influences this value depending on the transmission ratio. In Table 7.4 the thrust ratio is given for the cases OD and LOW for different levels of taperedness. For the OD case, if the taperedness increases (and thus the endplay reduces) the thrust ratio decreases. For the LOW case, in contrast, if the taperedness increases (and also the endplay reduces) the thrust ratio increases. Both results confirm the expectations.

Table 7.4: Thrust ratio for different taperedness

	non-tapered	tapered 05	tapered 08
OD	1.4854	1.4828	1.4722
LOW	1.1797	1.2014	1.2122

Altogether, the tapered model enhancement depicts the expected phenomena. A method to adapt the operational endplay in the simulation model has been developed

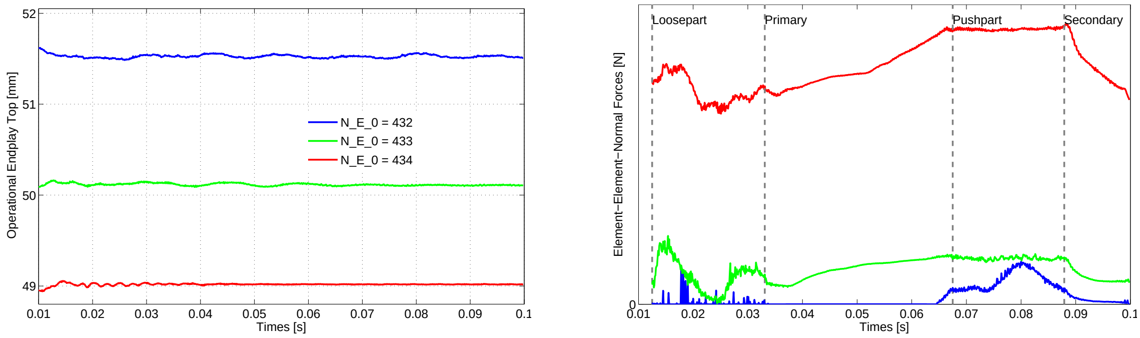

Figure 7.10: Operational endplay and element-element normal contact force for different N_{E_0} in case OD

thereby. This enhancement is different from the possibility to change the number of elements in reality N_{E_0} which virtually adds another element and adapts the scaling factor for the elements in the model. By increasing N_{E_0}, too, the operational endplay can be decreased, see Figure 7.10 (left) for the case OD and different numbers of N_{E_0}. However, this also lifts the overall force level of the element - element normal contact to an unrealistic setting, which is shown on the right side of Figure 7.10.

7.3 Unilateral element - ring set contact

This section shows the effects of the two different element - ring set normal contact models - the bilateral and unilateral contact at the element saddle.

7.3.1 Element contact forces

The element contact forces for the OD case with the bilateral and unilateral contact are shown in Figure 7.11 for 'Element 199'. In the element - pulley normal contact, when entering the small arc, the force peak is larger with the bilateral contact model and therefore the sagging is better represented. In the element - pulley longitudinal friction in the larger arc, the decline at the end is better reproduced with the unilateral contact. Whereas in the smaller arc the switch from positive to negative friction force takes place earlier with the bilateral contact which correlates with the measurements. For the radial friction in the smaller arc the force between the two peaks increases to the positive area in the unilateral case, which is closer to the measurements. A large difference can be seen in the element - element normal contact forces. There, the contact force rises earlier in the primary with the bilateral model and has an elevation (local maximum) in the primary, in the pushpart and the secondary. With the unilateral contact model, the force increase in the primary occurs later, then stays constant in the pushpart and increases in the end of the pushpart in the transition to the secondary. For the element - ring set forces in the two straight parts where the contact force level is around zero, the oscillations nearly vanish with the unilateral contact model. The contact forces in primary and secondary do not change significantly.

For the case LOW the changes are not as extensive as in the OD case. In Figure 7.12, the element contact forces are depicted for the LOW case for 'Element 177'. In the element - element normal contact force two elevations can be seen in the pushpart for the unilateral case. Again, the oscillations in the two straight parts of the element - ring set contact forces vanish with the unilateral contact.

7.3.2 Thrust ratio

In Table 7.5, the thrust ratio is shown for the bilateral and unilateral element - ring set normal contact law. The thrust ratio for the case OD is lifted with the unilateral contact

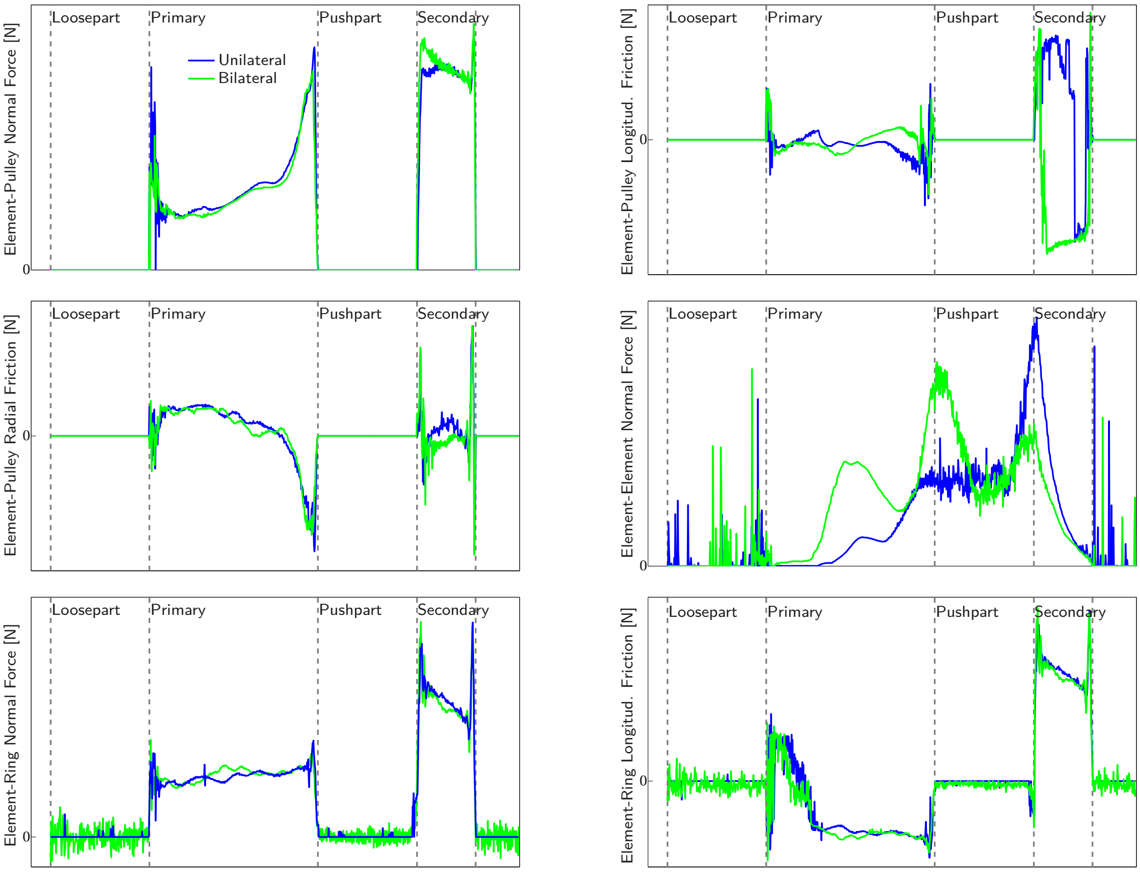

Figure 7.11: Element contact forces with unilateral and bilateral saddle for OD

law to the realistic setting. For the LOW case, the difference is not as significant.

Table 7.5: Thrust ratio for bilateral and unilateral law

	bilateral	unilateral
OD	1.2174	1.4854
LOW	1.3009	1.2929

7.3.3 Computing time reduction

In the unilateral saddle, the contact at the element saddle can lift and the ring set can get into contact with the element ear. This can be depicted with the simulation model. The contact element ear with the ring set occurs only in the two straight parts where the normal force on the element saddle is zero. The possible lifting leads also

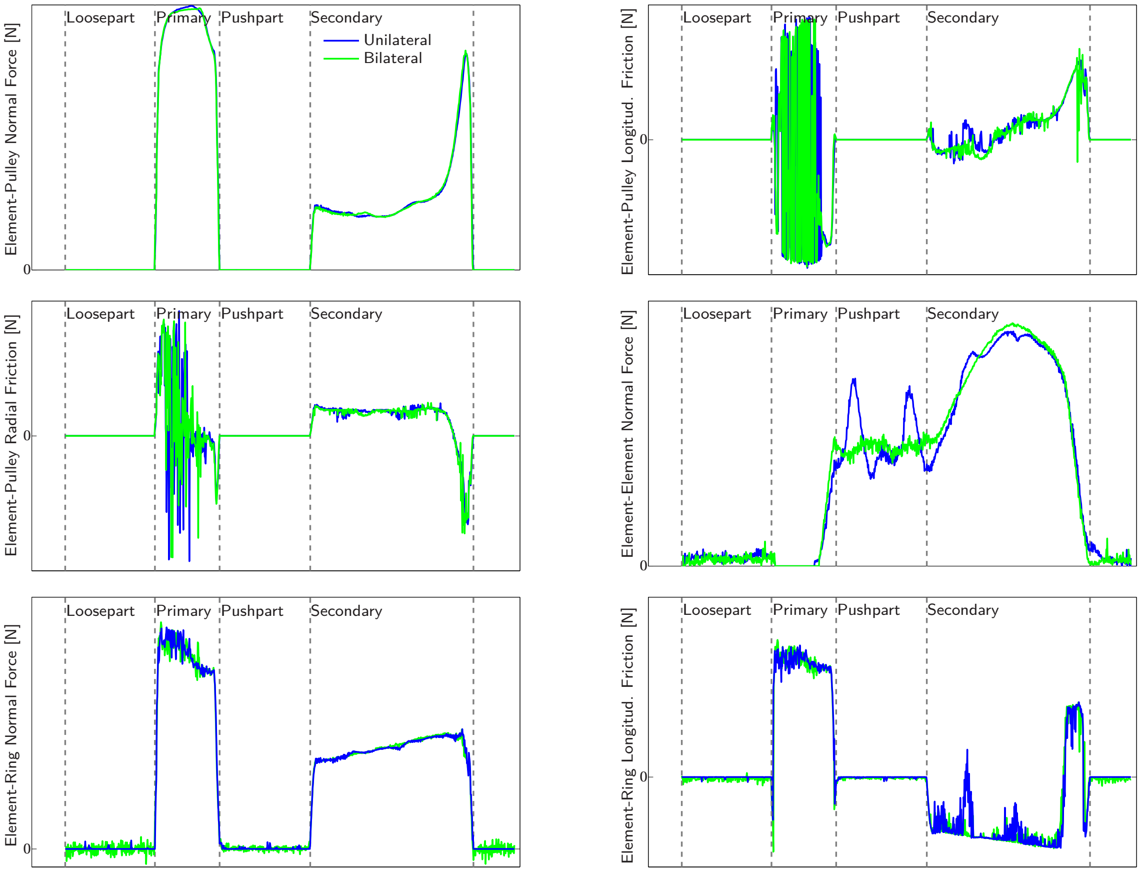

Figure 7.12: Element contact forces with unilateral and bilateral saddle for LOW

to a significant computing time reduction, as the element - ring set contact has to be calculated only when the contact is closed, in contrast to the bilateral case where it has to be calculated for every time step. Using the time-stepping scheme with step size control, the hybrid model with unilateral element - ring set contact is 1.55 times faster than with the bilateral contact (for OD). This is a huge computing time reduction. For the time-stepping scheme with fixed step size, which is applied in practice, it is even $1.7-2.2$ times faster depending on the setting (OD and LOW). Thus, both the unilateral and the bilateral model have their advantages. However, considering the faster computing time, the unilateral model is the model of choice.

7.4 Coupled contact law for element - sheave contact

For the element - pulley coupled and non-coupled normal contact law the element contact forces, the thrust ratio and the spiral running are investigated.

7.4.1 Element contact forces

For the element - pulley normal contact forces, quantitative measurements from Bosch exist. Therefore, a detailed and not only qualitative analysis can be made for this case. In Figure 7.13, the measurements, the coupled and the non-coupled element - pulley normal contact are shown for the boundary setting OD of two different elements. In the simulation the unilateral element ring set contact model is used. The force increase in the larger pulley arc with the peak at the end is expressed much better through the coupled contact model. In the smaller pulley arc both cases already include the force peak at the end, but the peak at the beginning is only rudimentary present. Here, it can also be seen that different elements may have different force curves. For 'Element 177' e.g. the sagging in the smaller arc is already visible for both force laws, in contrast to 'Element 199', where no sagging is present.

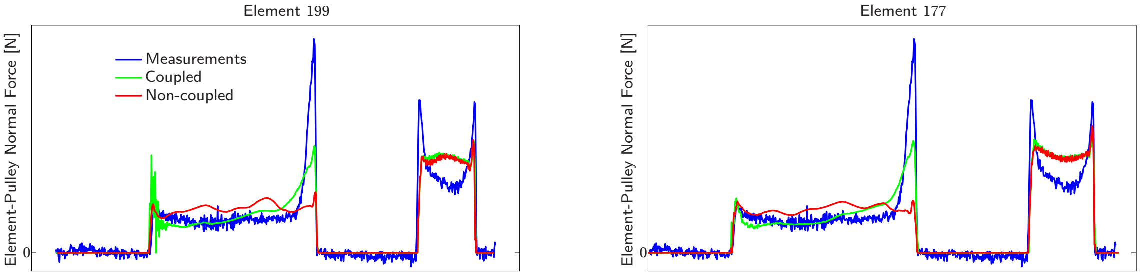

Figure 7.13: Measurement and simulation of element-pulley normal contact force for OD

The modelling of the element - pulley normal contact has not only effects on this force profile but great influence on the other contacts. For the case OD, the remaining element contact forces are shown in Figure 7.14 for 'Element 199'. Concerning the element - pulley friction, again, a considerable improvement is achieved with the coupled contact law in the larger pulley arc. Especially the course of the radial friction changes significantly to the correct behaviour by the coupled law. The course of the larger arc for the longitudinal frictions is slightly better reproduced by the non-coupled law. For the smaller arc in the radial friction both contact laws are in line with the measurements and in the longitudinal friction the unilateral behaviour is seen in both. For the element - ring set longitudinal force the elevation in the beginning of the primary pulley is better reproduced by the coupled law. A significant change can be seen in the element - element normal contact force where the force decreases at the end of the primary with the non-coupled law and increases again in the pushpart. Whereas in the coupled case the forces stay nearly constant from the end of the primary until the end of the pushpart.

Regarding the LOW case, again considerable improvements are achieved by means of the coupled law. In Figure 7.15, the element - pulley normal contact force measurements are compared to the simulation for two elements. Again, in the larger pulley arc the

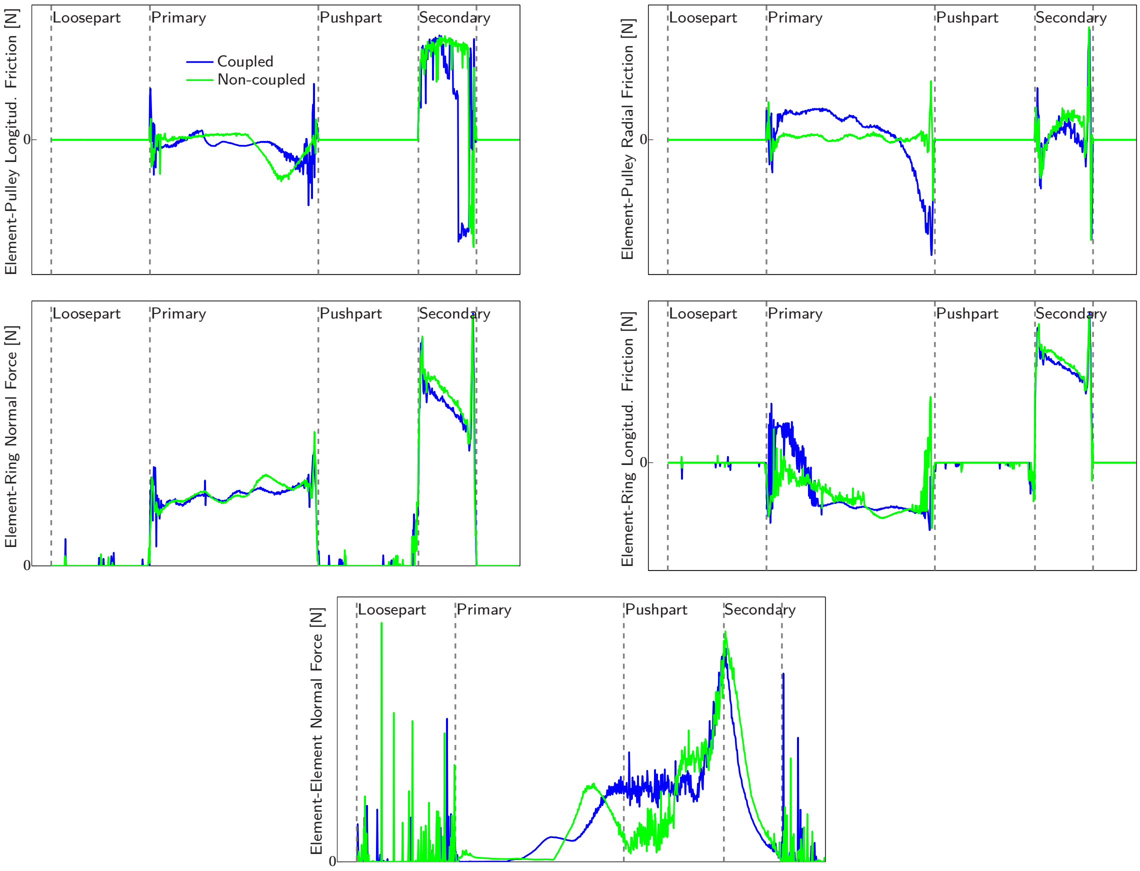

Figure 7.14: Remaining element contact forces coupled and non-coupled for OD

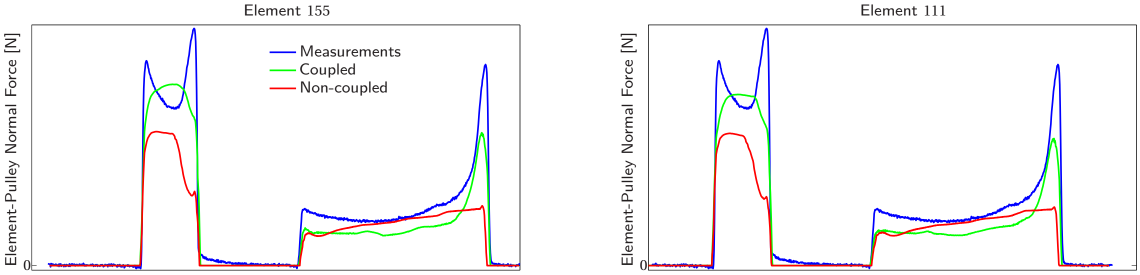

Figure 7.15: Measurement and simulation of element-pulley normal contact force for LOW

force peak at the end is present with the coupled law in contrast to the decoupled case. In addition, the force level in the smaller pulley arc comes much closer to the measurements in the coupled case. Nevertheless, the sagging in the smaller arc can not be depicted with both contact models.

The comparison of the remaining element contact forces for the LOW case can be seen in Figure 7.16 for 'Element 155'. In the larger pulley arc in the element - pulley frictions

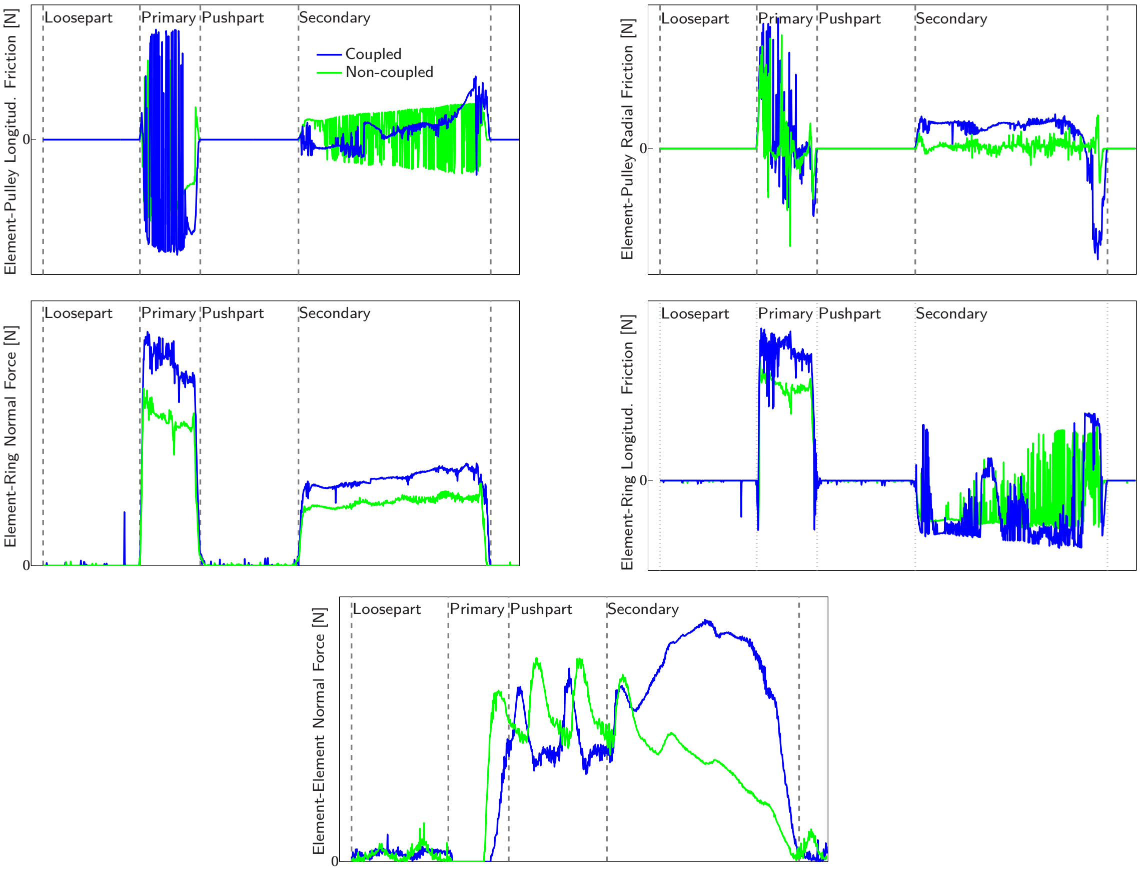

Figure 7.16: Remaining element contact forces coupled and non-coupled for LOW

the coupled law represents the measurements very well in contrast to the decoupled law where oscillations are present. The force increase in the element - element normal force in the secondary is depicted with the coupled law. With the decoupled law, the force decreases in the secondary pulley. Therefore, only by the coupled law this significant pushbelt behaviour of the force elevation in the secondary could be achieved. Also, the force level of the element - ring normal force is changed by the coupled law. For the longitudinal contact in the larger arc the right behaviour is reproduced with the coupled law, whereas oscillations are present for the non-coupled one. This shows clearly that the changes of this model enhancement have a range far beyond the element - pulley contact.

7.4.2 Thrust ratio

In Table 7.6, the thrust ratio for two boundary settings is given for the non-coupled and coupled element - pulley normal contact law. With the coupled law the thrust ratio is lifted in the LOW cases to the realistic level. Thus, a large improvement has been achieved. In the OD case also a small increase can be seen with the coupled law.

Table 7.6: Thrust ratio for non-coupled and coupled law

	non-coupled	coupled
OD	1.4172	1.4854
LOW	0.77436	1.1797

7.4.3 Spiral running

The comparison of the spiral running for the coupled and non-coupled law for the OD-SpiRun case can be seen in Figure 7.17. In the primary the characteristic decrease is obtained with the coupled law in contrast to the non-coupled case where the running radius stays nearly the same. For the secondary pulley a similar behaviour can be seen for both laws but the non-coupled law is a little closer to the measurements.

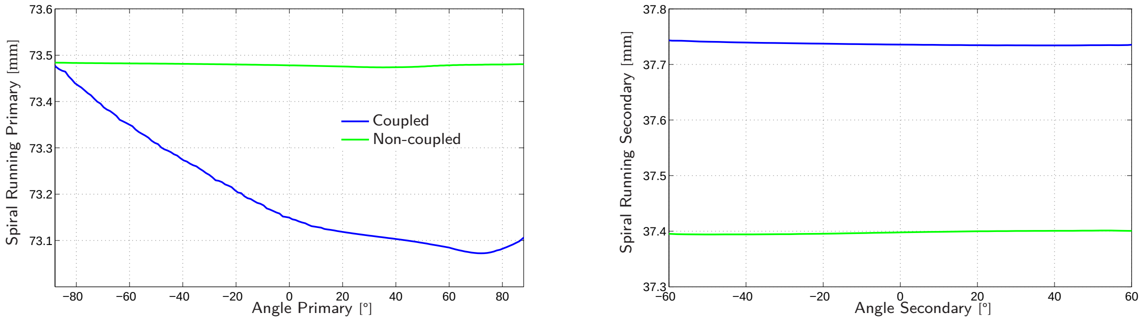

Figure 7.17: Spiral running at primary and secondary pulley for OD

Overall, the coupled contact law takes slightly more computing time of about 1.05, but compared to the great impovements this is of little importance.

7.5 Variable boundary conditions

The variable boundary conditions make the model more flexible. In particular, they solve the problem that in the simulation model only the geometric transmission ratio i_r could be specified, yet, in the measurements the speed ratio i_s is given. Thus, the geometric ratio had to be adjusted manually by running a full simulation for each setting to obtain the final speed ratio from the simulation results. In the boundary cases with two angular speeds, the speed ratio is implicitly specified. However, the torque can no longer be specified in these cases, as both rotational boundary conditions are given kinematically.

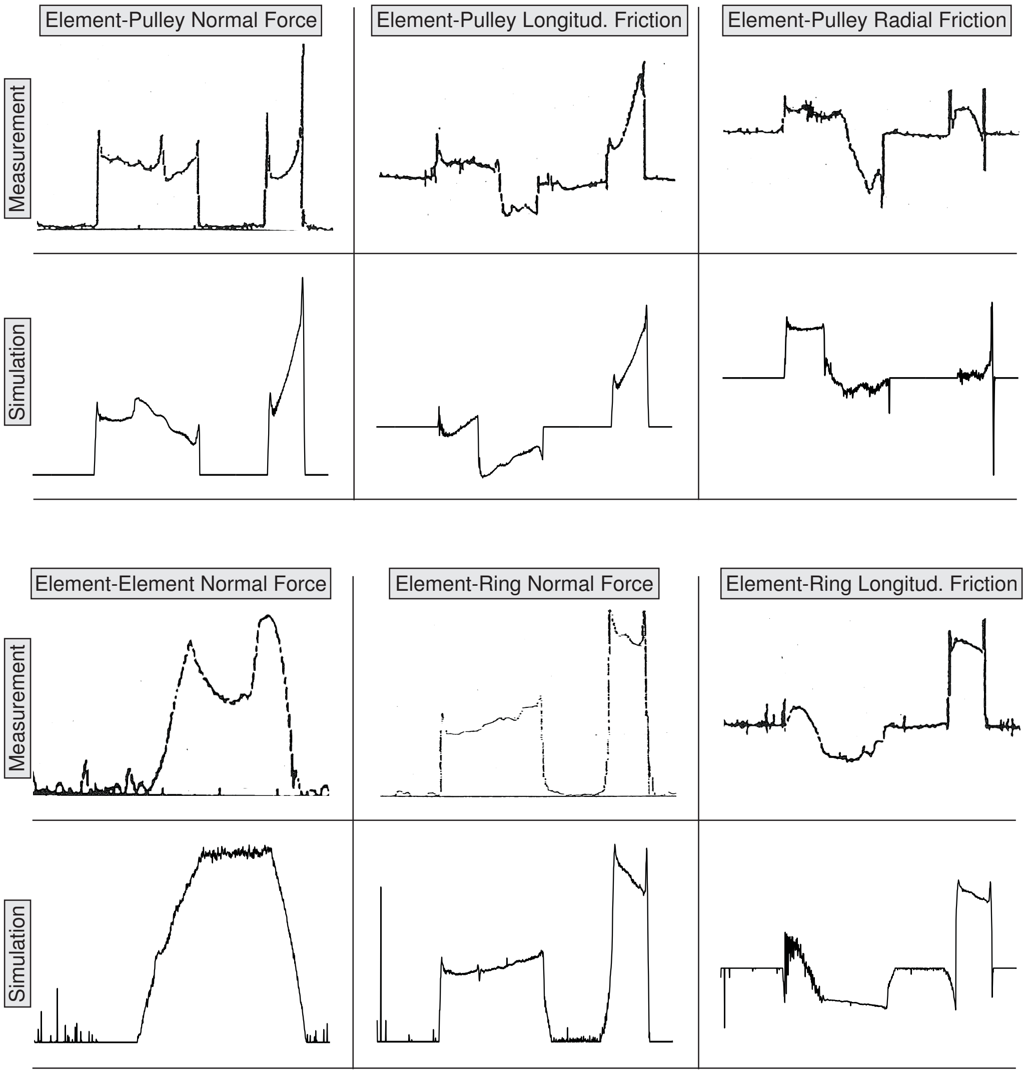

Figure 7.18: Measurement and simulation of element contact forces for OD

As a first validation, the six element contact forces are shown in Figure 7.18 with primary end stop and secondary speed. The speed ratio, primary angular velocity and secondary clamping forces are taken from the case OD. The appeared secondary torque of 31.85N m in the simulation (averaged between loose and fixed sheave) correlates with a torque ratio of 0.75. Thus, they are compared with the Honda measurement setting of speed ratio 0.5 and torque ratio 0.77. In the simulation the unilateral element - ring set contact and the coupled element - pulley law are used.

A very good correlation can now be seen in all contact forces. All force peaks in the element - pulley normal contact force are depicted. Moreover, the sagging in the smaller arc can be seen. The rising, starting from a positive value, in the smaller arc of the element - pulley longitudinal friction is for the first time present with this enhancement. Both larger arcs of the element - pulley friction are represented in detail. The element - element normal force depicts the expected behaviour with the additional top contact acting in the pushpart. The element - ring set normal contact and longitudinal friction are in very good alignment with the measurements. Overall, a large improvement, especially in the smaller arc, is achieved with the specification of the two angular velocities.

8 Conclusions and Future Work

Several model enhancements have been presented in this study to further improve the pushbelt CVT model. Altogether, most enhancements achieve their purpose and contribute to a functional refinement of the variator model. In particular, comparisons of the hybrid model with measurements show a very good representation of the local element contact forces as well as the global phenomena spiral running and thrust ratio. This validates the hybrid model. Additionally, a large computing time reduction could be achieved by means of the hybrid model when one is only interested in planar phenomena. The effects of the different model enhancements on the element - element contact forces have been shown in this study. The enhancement to depict tapered elements in the simulation adds a method to adapt the operational endplay and to influence the element - element normal contact force, e.g. that it starts earlier in the primary pulley with increased taperedness. By means of the unilateral element - ring set contact a representation of another technical feature of the CVT could be achieved. Thus, the ring sets can lose contact with the element saddle and get into contact with the element ear. This model enhancement reduces the oscillations in the element - ring set contact forces in the two straight parts and additionally the calculation time. The planar pre-integration works for academic examples. However, it is not feasible in the presented way in the CVT model, as small inaccuracies in the numerical calculation of the flexible RCM beam coordinates result in an incorrect solution of the internal nonlinear transformation to the internal coordinate set. The coupled element - pulley sheave normal contact law significantly improves the element contact forces; in particular the element - element normal forces and all three element - pulley contact forces. In addition, the spiral running and the thrust ratio are brought to the expected behaviour. The variable boundary concept presented in this study shows good improvements in first validations; especially the small arcs in the element contact forces could be significantly improved. The Cosserat rod model has been validated by means of academic examples. It turns out to be very stiff and thus difficult to be applied in the CVT setting because of a too small integration time step size resulting in too long computing times. Nonlinear model order reduction techniques have been applied to filter out higher frequencies and allow for a larger time step. These concepts worked for academic examples, however, they have yet to prove themselves in practice.

These enhancements represent a large step forward to a detailed spatial pushbelt CVT model. Yet, as the time period of this study is limited, it is not the final step. Some topics have to be done in the follow-up project. In particular, the ring tracking law has to be validated and can be refined with a physical based model. The pre-integration concept can be revised to make it function for the CVT model. Further approaches have to be tried to get rid of the stiffness of the Cosserat rod model. As for the POD, the limiting factor is that a full simulation is required for the snapshot matrix. This full simulation with a large computing time has to be done for each CVT setting. Thus, also different methods should be tried to solve the problem. A possible solution strategy could be to split the solution into a low and high spectrum component and extract the higher frequency modes to use a larger time step size for explicit time-stepping schemes as proposed in [41]. Further boundary cases are possible with two end stops or primary torque or a different concept with two speeds in combination with secondary clamping and secondary torque to adjust the torque ratio. Finally, an intensified validation for the overall spatial pushbelt CVT model, already in work for the follow-up project, should be carried out. There, additionally to the phenomena presented here, others like efficiency, slip curves, bearing forces and noise - vibration - harshness will be validated intensively with measurements obtained from Bosch.

Bibliography

[1] Vincent Acary and Bernard Brogliato. *Numerical methods for nonsmooth dynamical systems : applications in mechanics and electronics*, volume 35 of *Lecture notes in applied and computational mechanics*. Springer, Berlin, 1st edition, 2008.

[2] Pierre Alart and Alain Curnier. A mixed formulation for frictional contact problems prone to Newton like solution methods. *Comput Methods Appl Mech Engrg*, 92:353 – 375, 1991.

[3] Athanasios C. Antoulas. *Approximation of large-scale dynamical systems*, volume 6. SIAM, 2009.

[4] Martin Arnold. Numerical methods for simulation in applied dynamics. In Martin Arnold and Werner Schiehlen, editors, *Simulation Techniques for Applied Dynamics*, number 507 in CISM International Centre for Mechanical Sciences, pages 191–246. Springer, Wien, 2009.

[5] Bosch Transmission Technology B.V. Continuously variable transmission – drive into a stepless world. Leaflet: `http://www.bosch.nl/transmission_technology/nl/downloads/GS_CVT_Leaflet_En_final.pdf`.

[6] Bernard Brogliato. *Nonsmooth mechanics: models, dynamics and control*. Communications and control engineering. Springer, London, 2nd edition, 1999.

[7] Olivier Brüls, Alberto Cardona, and Michel Géradin. Modelling, simulation and control of flexible multibody systems. In *Simulation Techniques for Applied Dynamics*, pages 21–74. Springer, 2009.

[8] Markus Bullinger. *Dynamik von Umschlingungsgetrieben mit Schubgliederband*. Number 593 in Fortschrittberichte VDI: Reihe 12. VDI Verlag, Düsseldorf, 2005.

[9] Thomas Cebulla, Kilian Grundl, Thorsten Schindler, Heinz Ulbrich, Arie van der Velde, and Han Pijpers. Spatial Dynamics of Pushbelt CVTs: Model Enhancements. *SAE Transmissions & drivelines*, SP 2334(2012-01-0307):97–106, April 2012.

[10] Thomas Cebulla and Thorsten Schindler. Application of Cosserat rods in the non-smooth spatial simulation of pushbelt CVTs. In preparation.

[11] Thomas Cebulla, Thorsten Schindler, and Heinz Ulbrich. Spatial Dynamics of Cosserat Rods with Set-Valued Force Laws. In *84th Annual Scientific Conference of the International Association of Applied Mathematics and Mechanics, Novi Sad, Serbia*, 2013.

[12] Saifon Chaturantabut and Danny C. Sorensen. Nonlinear model reduction via discrete empirical interpolation. *SIAM Journal on Scientific Computing*, 32(5):2737 – 2764, 2010.

[13] Richard Cottle. *The linear complementarity problem.* Classics in applied mathematics ; 60. SIAM, Philadelphia, 2009.

[14] Hansjörg Dach, Wolf-Dieter Gruhle, and Peter Köpf. *Pkw-Automatgetriebe: Sicher, komfortabel und wirtschaftlich fahren*, volume 88 of *Die Bibliothek der Technik*. Verl. Moderne Industrie, Landsberg/Lech, 2nd edition, 2001.

[15] F. N. Fritsch and R. E. Carlson. Monotone piecewise cubic interpolation. *SIAM Journal on Numerical Analysis*, 17(2):238–246, 1980.

[16] Martin Förg. *Mehrkörpersysteme mit mengenwertigen Kraftgesetzen: Theorie und Numerik*. Number 411 in Fortschritt-Berichte VDI: Reihe 20. VDI Verlag, Düsseldorf, 2007.

[17] Thomas Geier. *Dynamics of push belt CVTs*. Number 654 in Fortschrittberichte VDI: Reihe 12. VDI Verlag, Düsseldorf, 2007.

[18] Christoph Glocker. *Set-valued force laws in rigid body dynamics : dynamics of non-smooth systems*, volume 1 of *Lecture notes in applied and computational mechanics*. Springer, Berlin, 1st edition, 2001.

[19] Kilian Grundl. The Maxwell Contact. Diploma thesis, Technische Universität München, 2011. Supervisors: Thomas Cebulla, Thorsten Schindler and Heinz Ulbrich.

[20] Kilian Grundl, Thomas Cebulla, Thorsten Schindler, and Heinz Ulbrich. The Maxwell-Contact. *PAMM*, 12(1):73–74, 2012. `http://dx.doi.org/10.1002/pamm.201210028`.

[21] Ernst Hairer and Gerhard Wanner. *Solving Ordinary Differential Equations II: Stiff and Differential-Algebraic-Problems*, volume 14 of *Springer series in computational mathematics*. Springer, Berlin, 2nd rev. edition, 2010.

[22] Robert Huber and Heinz Ulbrich. Higher order integration of non-smooth dynamical systems using parallel computed extrapolation methods based on time-stepping schemes. In *Proceedings of 1st Joint International Conference on Multibody System Dynamics, Lappeenranta*, May 2010.

[23] Shigeru Kanehara, Toru Fujii, and Takashi Kitagawa. A study of a metal pushing V-belt type CVT - part 3: what forces act on metal blocks. *SAE Technical Paper Series*, 940735:139–169, 1994.

[24] Tim Willem Gerard Leo Klaassen. *The empact CVT: dynamics and control of an electromechanically actuated CVT.* PhD thesis, Technische Universiteit Eindhoven, 2007.

[25] Werner Klement. *Fahrzeuggetriebe.* Fahrzeugtechnik. Hanser Verlag, München, 2nd edition, 2007.

[26] Martin Krüssmann. Driving CVT into a new area - Demonstrating a new benchmark for fuel consumption and cost for all markets. In *Transmissions in Vehicles; International VDI Congress Friedrichshafen*, number 2130 in VDI-Berichte, pages 427–442, Düsseldorf, 2011. VDI Verlag.

[27] Christian Käsbauer. Dynamics of Cosserat rods. Term paper, Technische Universität München, 2012. Supervisors: Thomas Cebulla, Thorsten Schindler.

[28] Holger Lang, Joachim Linn, and Martin Arnold. Multi-body dynamics simulation of geometrically exact cosserat rods. *Multibody System Dynamics*, 25(3):285–312, 2011.

[29] Remco Ingmar Leine and Nathan van de Wouw. *Stability and convergence of mechanical systems with unilateral constraints*, volume 36 of *Lecture notes in applied and computational mechanics.* Springer, Berlin, 1st edition, 2008.

[30] John E. Lloyd. Fast Implementation of Lemke's Algorithm for Rigid Body Contact Simulation. In *Proceedings of the 2005 IEEE International Conference on Robotics and Automation*, pages 4538–4543. IEEE, 2005.

[31] MBSim - multi-body simulation software. GNU Lesser General Public License `http://code.google.com/p/mbsim-env/`.

[32] Cleve B. Moler. *Numerical computing with MATLAB.* SIAM, 2004.

[33] Jean Jacques Moreau. Bounded Variation in Time. In *Topics in Nonsmooth Mechanics*, pages 1–74. Birkhäuser, Basel, 1988.

[34] Jean Jacques Moreau. Unilateral contact and dry friction in finite freedom dynamics. In *Nonsmooth Mechanics and Applications*, volume 302 of *CISM Courses and Lectures*, pages 1–82. Springer, Wien, 1988.

[35] Harald Naunheimer, Bernd Bertsche, Joachim Ryborz, and Wolfgang Novak. *Automotive Transmissions: Fundamentals, Selection, Design and Application.* Springer, Berlin, 2nd edition, 2011.

[36] OpenMBV - open multi body viewer. GNU General Public License `http://code.google.com/p/openmbv/`.

[37] G. S. Pandit and S. P. Gupta. *Structural Analysis: a Matrix Approach*. Tata McGraw-Hill, 1981.

[38] Friedrich Pfeiffer. *Mechanical system dynamics*, volume 40 of *Lecture notes in applied and computational mechanics*. Springer, Berlin, 1st edition, 2008.

[39] Les Piegl and Wayne Tiller. *The NURBS book*. Monographs in visual communications. Springer, Berlin, 2nd edition, 1997.

[40] Dilip Prasad and Brice N. Cassenti. Development and validation of a model for flat belt tracking in pulley drive systems. *J. Dyn. Sys., Meas., Control*, 134(1):011006–011006–8, 2012.

[41] Daniel J. Rixen. Explicit-implicit time-stepping for non-uniformly meshed models. In H. Boden and A. Nilsson, editors, *Proceedings of the 10th International Congress on Sound and Vibration*, pages 3949–3956, Stockholm, July 2003.

[42] Jesus Rodriguez, Frederic Brix, and Tomohisa Kumagai. A Fast-Running Model of a Van Doorne (Push-Belt) CVT Including Belt Tension and Compression Compliance. *SAE Transmissions & drivelines*, SP 2334(2012-01-0628):199–214, April 2012.

[43] Toshihiro Saito. Finite Element Analysis Coupled with Feedback Control for Dynamics of Metal Pushing V-Belt CVT. In Farzad Ebrahimi, editor, *Finite Element Analysis - Applications in Mechanical Engineering*. InTech, 2012.

[44] Heiko Sattler. *Stationäres Betriebsverhalten stufenlos verstellbarer Metallumschlingungsgetriebe*. PhD thesis, Universität Hannover, 1999.

[45] Thorsten Schindler. *Spatial dynamics of pushbelt CVTs*. Number 730 in Fortschritt-Berichte VDI: Reihe 12. VDI Verlag, Düsseldorf, 2010. `http://mediatum.ub.tum.de/node?id=981870`.

[46] Thorsten Schindler, Martin Förg, Markus Friedrich, Markus Schneider, Bastian Esefeld, Robert Huber, Roland Zander, and Heinz Ulbrich. Analysing dynamical phenomenons: introduction to MBSim. In *Proceedings of 1st Joint International Conference on Multibody System Dynamics, Lappeenranta*, May 2010.

[47] Thorsten Schindler, Binh Nguyen, and Jeff Trinkle. Understanding the difference between prox and complementarity formulations for simulation of systems with contact. In *IROS*, pages 1433–1438, 2011.

[48] Ahmed Shabana. *Dynamics of multibody systems*. Cambridge University Press, New York, 3rd edition, 2005.

[49] Nilabh Srivastava and Imtiaz Haque. A review on belt and chain continuously variable transmissions (CVT): Dynamics and control. *Mech Mach Theor*, 44:19–41, 2009.

[50] Karsten Stahl, Hermann Pflaum, and Sebastian Idler. Investigation on the scuffing resistance of belt and chain continuously variable transmissions. In *Transmissions in Vehicles; International VDI Congress Friedrichshafen*, number 2071 in VDI-Berichte, Düsseldorf, 2009. VDI Verlag.

[51] Armin Sue. *Betriebsverhalten stufenloser Umschlingungsgetriebe unter Einfluss von Kippspiel und Verformungen*. PhD thesis, Universität Hannover, 2003.

[52] Schaeffler Technologies. LuK's CVT chain provides continuously variable driving comfort. Press release: `http://www.schaeffler.de/content.schaeffler.de/de_2/_global/download/pdf/pressrelease_31630848.pdf`.

[53] André Teubert, Andreas Englisch, Andreas Götz, André Linnenbrügger, and Thomas Endler. Luk cvt technology–efficiency, comfort, dynamics. In *Transmissions in Vehicles; International VDI Congress Friedrichshafen*, number 2071 in VDI-Berichte, Düsseldorf, 2009. VDI Verlag.

[54] Heinz Ulbrich. Some selected research activities in mechatronic applications - case studies. In *International Conference on Engineering Mechanics, Structures, Engineering Geology, Rhodos*, July 2009.

[55] Erik van der Noll, Francis van der Sluis, Tom van Dongen, and Arie van der Velde. Innovative self-optimizing clamping force strategy boosts effiency of the pushbelt CVT. In *7th International CTI Symposium: Innovative Automotive Transmissions, Berlin*, December 2008.

[56] Robert von Zitzewitz. Fast planar dynamics of cosserat rods with set-valued force laws. Diploma thesis, Technische Universität München, 2013. Supervisors: Thomas Cebulla, Thorsten Schindler.

[57] Tamer Wasfy and Ahmed Noor. Computational strategies for flexible multibody systems. *Appl Mech Rev*, 56:553–613, 2003.

[58] Katsu Yamane and Yoshihiko Nakamura. A numerically robust LCP solver for simulating articulated rigid bodies in contact. In *Proceedings of Robotics: Science and Systems IV*, Zurich, Switzerland, June 2008.

[59] Roland Zander. *Flexible multi-body systems with set-valued force laws*. Number 420 in Fortschritt-Berichte VDI: Reihe 20. VDI Verlag, Düsseldorf, 2009. `http://mediatum2.ub.tum.de/node?id=654788`.

[60] Roland Zander, Thorsten Schindler, Markus Friedrich, Robert Huber, Martin Förg, and Heinz Ulbrich. Non-smooth dynamics in academia and industry: recent work at TU München. *Acta Mech*, 195:167–183, 2008.